POLITECNICO
MILANO 1863

Department of Energy
Doctoral Programme in Energy and Nuclear Science and Technology

Multiphysics Modelling of Solid Fission Products Transport in the Molten Salt Fast Reactor

Doctoral Dissertation of:
Andrea Di Ronco

Supervisors:
Prof. Antonio Cammi
Prof. Francesca Celsa Giacobbo
Prof. Stefano Lorenzi

Tutor:
Prof. Francesca Celsa Giacobbo

The Chair of the Doctoral Program:
Prof. Vincenzo Dossena

Cycle XXXIV
Year 2023

Abstract

Due to its innovative design and the strong coupling among thermal hydraulics, neutronics and fuel chemistry, the multiphysics approach has become a standard tool to address the design and analysis of the Molten Salt Fast Reactor (MSFR). Despite recent advancements, the integration of fission products (FPs) transport modelling has not been addressed yet. Some FP species are not expected to form stable compounds with the constituents of the liquid fuel salt and are likely to deposit on reactor surfaces in the form of solid precipitates, giving rise to potential issues such as formation of localised decay heat sources as well as deterioration of heat exchanger performance. The correct evaluation of solid FPs distribution is also crucial for the estimation of the radiological and decay heat inventory of the reactor, and to design effective FPs management and reprocessing strategies.

The main goal of this work is therefore the extension of state-of-the-art MSFR multiphysics tools towards the modelling and simulation of solid FPs within the reactor. Several aspects are covered, including (i) the treatment of deposition of precipitated solid particles on reactor walls, both from the modelling and numerical viewpoint; (ii) the modelling of precipitation/dissolution of FP particles to account for local temperature variations; (iii) effects of turbulence closure modelling on the prediction of transported species, especially for complex geometries. An advection-diffusion-decay model is first integrated in an incompressible single-phase multiphysics MSFR solver based on the open-source CFD library OpenFOAM. Then the developed models are tested on two-dimensional MSFR cases, showing the role of RANS turbulence modelling on the prediction of particle transport and deposition. The development of a three-dimensional LES model for the MSFR is also addressed, suggesting the feasibility of more advanced turbulence modelling approaches in the context of multiphysics analysis of the MSFR. Preliminary results show interesting dynamic behaviour, with promising applications in a wide range of MSFR studies.

Estratto

Grazie a caratteristiche progettuali innovative e al forte accoppiamento tra termoidraulica, neutronica e chimica del combustibile, l'approccio multifisico è divenuto uno strumento standard nell'analisi e la progettazione del reattore veloce a sali fusi (MSFR). Nonostante i recenti progressi, il trasporto dei prodotti di fissione (FP) è un aspetto non ancora studiato nel dettaglio. Alcune specie di FP, che non formano composti stabili con i costituenti della miscela del combustibile liquido, possono depositare sulle superfici del reattore sotto forma di precipitati solidi, dando luogo a problematiche quali la formazione di sorgenti di calore di decadimento localizzate e il deterioramento delle prestazioni degli scambiatori di calore. La corretta previsione della distribuzione dei FP solidi è anche di rilievo per la stima dell'inventario radiologico e del calore di decadimento del reattore, e per lo studio di strategie efficaci per la gestione e il riprocessamento degli stessi FP.

L'obiettivo principale di questo lavoro è dunque l'estensione degli strumenti di analisi multifisica per il MSFR allo stato dell'arte verso la modellazione del trasporto di FP solidi all'interno del reattore. Tra i diversi aspetti presi in esame figurano (i) la deposizione di particelle solide precipitate sulle pareti del reattore, da un punto di vista sia modellistico che numerico; (ii) la modellazione della loro precipitazione/dissoluzione in funzione delle variazioni locali di temperatura; (iii) gli effetti dovuti alla scelta dei modelli di turbolenza sulla stima delle specie trasportate, in particolare per geometrie più complesse. Delle equazioni di trasporto per i FP sono state dapprima integrate in un solutore multifisico monofase incomprimibile basato sulla libreria CFD open-source OpenFOAM. I modelli sviluppati sono stati poi testati su casi semplificati inerenti al MSFR, mostrando il ruolo dei modelli di turbolenza RANS nella previsione del trasporto e della deposizione delle particelle solide. Infine, è stato sviluppato un modello LES preliminare del reattore allo scopo di mostrare la fattibilità dell'impiego di approcci più avanzati di modellazione della turbolenza nel contesto dell'analisi multifisica del MSFR, con interessanti risvolti nello studio della dinamica e del controllo del reattore.

Contents

Acknowledgements **9**

List of Figures **11**

List of Tables **15**

List of Symbols **17**

1 Introduction **23**
- 1.1 Objectives, motivation and outline 24
- 1.2 The Molten Salt Fast Reactor 25

2 The Multiphysics Model **27**
- 2.1 The OpenFOAM library 27
- 2.2 Thermal hydraulics model 29
- 2.3 Neutronics model 30
  - 2.3.1 Calculation of group constants 31
- 2.4 Fission products transport model 32
  - 2.4.1 Deposition modelling 33
  - 2.4.2 Distributed sources 35
  - 2.4.3 Precipitation chemistry 38
- 2.5 Analytical verification 39
  - 2.5.1 Momentum equation 40
  - 2.5.2 Particle concentration equation 40
  - 2.5.3 Derivation of the analytical solution 42
  - 2.5.4 Results 45

3 Fission Products Transport in the MSFR **53**
- 3.1 The CNRS benchmark cavity 54
  - 3.1.1 Results and discussion 54
- 3.2 The two-dimensional EVOL MSFR 56
  - 3.2.1 Results and discussion 60
- 3.3 Simplified precipitation 66

4 Large Eddy Simulation of the MSFR 67
4.1 Case setup . . . 68
4.1.1 Geometry and mesh . . . 68
4.1.2 Initialisation . . . 69
4.1.3 LES turbulence modelling . . . 69
4.2 Results and discussion . . . 72

5 Conclusion 83
5.1 Further work . . . 84

A Supplement to the Analytical Model 87
A.1 Computation of M(a,b;z) . . . 87
A.2 Evaluation of normalization integrals . . . 88

B Neutronics and precursors data 91
B.1 CNRS benchmark cavity . . . 91
B.2 Two-dimensional EVOL MSFR . . . 93
B.3 Three-dimensional 1/16 cyclic MSFR . . . 93

Bibliography 99

Ringraziamenti 105

Acknowledgements

The research upon which this thesis work is based has been carried out in the framework of a collaboration among Politecnico di Milano and the other institutions involved in the H2020-Euratom project SAMOSAFER (`https://samosafer.eu`). As such, it has received funding from the Euratom research and training programme 2014-2018 under grant agreement no. 847527.

This work was also enabled in part by support provided by Compute Ontario (`https://www.computeontario.ca`) and the Digital Research Alliance of Canada (`https://alliancecan.ca`).

List of Figures

2.1 Decoupling of the transport and deposition problems: solutions for the wall region (C_w) and the bulk region (C_b) are obtained separately and joined by imposing interface continuity on particle concentration and particle flux at $y = \delta_\phi$. The wall region thickness $\delta_\phi \ll H$ is defined as the distance at which $\phi(\delta_\phi)$ becomes arbitrarily small. 34

2.2 Parallel plates channel geometry: with respect to the flow, the y coordinate denotes the transversal direction. Wall boundaries are located at $y = \pm H$. 36

2.3 Analytical solutions for the 1D parallel plates geometry. Different S_{min} to S_{max} ratios produce similar behaviours: the concentration profiles follow a cosine-shaped profile in the bulk flow, then drop to 0 in a thin region close to the wall boundary. The thickness Δy^* shows little dependence on S_{min}/S_{max}. For these cases, $Da = 80000$. 37

2.4 Parallel plates geometry: with respect to the flow, the x and y coordinates denote the longitudinal and transversal directions. Inlet and outlet boundaries are located at $x = 0$ and $x = L$ respectively, while wall boundaries are located at $y = \pm H$. 39

2.5 Dependence of the 1st eigenvalue β_1 on model parameters Sh and Da. . . 46

2.6 Dependence of the 2nd eigenvalue β_5 on model parameters Sh and Da. . 46

2.7 Dependence of the 5th eigenvalue β_5 on model parameters Sh and Da. . . 47

2.8 Dependence of the 10th eigenvalue β_{10} on model parameters Sh and Da. . 47

2.9 Comparison of concentration profiles obtained with the proposed transport model implemented in OpenFOAM ($\circ$) and the corresponding analytical solutions ($-$) for cases 1, 2 and 3 (from top to bottom). 49

2.10 Comparison of concentration profiles obtained with the proposed transport model implemented in OpenFOAM ($\circ$) and the corresponding analytical solutions ($-$) for cases 4, 5 and 6 (from top to bottom). 50

2.11 Comparison of concentration profiles obtained with the proposed transport model implemented in OpenFOAM ($\circ$) and the corresponding analytical solutions ($-$) for cases 7, 8 and 9 (from top to bottom). 51

3.1 Lid-driven cavity: geometry (from [49], left) and computational mesh (coarsest case, right). The grid is refined by means of a constant growth-rate in the first 40 layers of cells, starting from a prescribed smallest layer size 55

3.2 Velocity U (left) and temperature T (right) distributions in the lid-driven cavity (most refined mesh, 400 divisions). Velocity streamlines are also added for more clarity. The combined action of lid motion and buoyancy affects the flow pattern, producing two separate recirculation zones. . . . 57

3.3 Particle concentration C distributions for three different mesh refinements: from top to bottom, 100, 200, and 400 divisions in both directions. 58

3.4 Particle concentration C wall profiles for three different mesh refinements. Line plots correspond to a horizontal line at half the cavity height on the left (top plot) and right (bottom plot) walls, corresponding to points A and A' of Figure 3.1. 59

3.5 EVOL case: an axisymmetric geometry (left) is chosen to reduce the computational requirements and the resulting mesh (right) is predominantly structured thanks to the simple geometry employed. Wall mesh refinement is obtained by subsequent divisions of the wall layer. 60

3.6 Magnitude of velocity $\mathbf{u}$ (left) and total kinetic viscosity ν_{eff} (right) distributions in the EVOL reactor for the $k-\varepsilon$, $k-\omega$ and $k-\omega-SST$ turbulence models (from top to bottom). 62

3.7 Particle concentration C distributions for the $k-\varepsilon$, $k-\omega$ and $k-\omega-SST$ turbulence models (from top to bottom). Plots on the left and right columns refer to Sc_t equal to 0.50 and 1.20, respectively. 63

3.8 Particle concentration C wall profiles for different values of the turbulent Schmidt number Sc_t and turbulence models. Line plots refer to vertical lines of length 0.01 m placed at 0.8 m from the reactor symmetry axis on the bottom (top plot) and top (bottom plot) walls (A-A' in Figure 3.5). . 64

3.9 FP precipitate concentration C^p for the cavity benchmark case. On the left, base case with direct formation of the solid precipitate phase; on the right, simplified equilibrium precipitation model. 66

4.1 MSFR 3D case: a 1/16 cyclic domain is chosen to reduce the computational requirements and the resulting hexahedral mesh is predominantly structured. 70

4.2 Normalised total reactor power during LES transients for different mesh refinements and SGS models. 73

4.3 Average reactor temperature during LES transients for different mesh refinements and SGS models. 74

4.4 Normalised total reactor mass flow rate during LES transients for different mesh refinements and SGS models. 75

4.5 Normalised total reactor fission rate during LES transients for different mesh refinements and SGS models. 76

4.6 Normalised integrated concentration of 1st family of delayed neutron precursors during LES transients for different mesh refinements and SGS models. 77
4.7 Normalised integrated concentration of 8th family of delayed neutron precursors during LES transients for different mesh refinements and SGS models. 78
4.8 Initial fields from standard k-ε RANS for LES simulation of "700k" mesh on a vertical midplane section. 79
4.9 Solution fields after 20 s of Smagorinsky LES simulation of "700k" mesh on a vertical midplane section. 80

List of Tables

2.1 Values of Da e Sh selected for verification cases. 45

2.2 Model parameters used in all verification cases. 46

2.3 Computational times for the verification cases. 5×10^4 iterations are performed on 5×10^4 volumes with 8 CPUs. 48

3.1 Main physical parameter values adopted for the lid-driven cavity case [49]. 55

3.2 Main physical parameter values adopted for the EVOL case. 61

3.3 EVOL case: main simulation results for the selected turbulence models and values of Sc_t. The balance error is computed as the relative difference between the integral source and the sum of the integral deposition and decay rates. 65

4.1 Main 3D MSFR mesh information. 69

4.2 Main physical parameter values adopted for the 3D MSFR case. 71

B.1 CNRS benchmark cavity neutron group constants: diffusion coefficient, absorption cross-section, fission cross-section. 91

B.2 CNRS benchmark cavity neutron group constants: scattering cross-section. 92

B.3 CNRS benchmark cavity neutron group constants: average neutron yield per fission, average energy yield per fission, inverse neutron velocity, prompt fission yield spectrum, decay energy yield spectrum. 92

B.4 CNRS benchmark cavity precursor family constants: delayed neutron precursors fraction, delayed neutron precursors decay constant. 93

B.5 Two-dimensional EVOL MSFR neutron group constants: diffusion coefficient, absorption cross-section, fission cross-section. 93

B.6 Two-dimensional EVOL MSFR neutron group constants: scattering cross-section. 94

B.7 Two-dimensional EVOL MSFR neutron group constants: average neutron yield per fission, average energy yield per fission, inverse neutron velocity, prompt fission yield spectrum, decay energy yield spectrum. 94

B.8 Two-dimensional EVOL MSFR precursor family constants: delayed neutron precursors fraction, delayed neutron precursors decay constant. . . . 95

B.9 Three-dimensional 1/16 cyclic MSFR neutron group constants: diffusion coefficient, absorption cross-section, fission cross-section. 95
B.10 Three-dimensional 1/16 cyclic MSFR neutron group constants: scattering cross-section. 96
B.11 Three-dimensional 1/16 cyclic MSFR neutron group constants: average neutron yield per fission, average energy yield per fission, inverse neutron velocity, prompt fission yield spectrum, decay energy yield spectrum. . . . 96
B.12 Three-dimensional 1/16 cyclic MSFR precursor family constants: delayed neutron precursors fraction, delayed neutron precursors decay constant. . 97

List of Symbols

Acronyms

CFD	Computational Fluid Dynamics
CNRS	Centre National de la Recherche Scientifique
CSG	constructive solid geometry
FP	fission product
FVM	Finite Volume Method
LES	Large Eddy Simulation
MSBR	Molten Salt Breeder Reactor
MSFR	Molten Salt Fast Reactor
MSR	Molten Salt Reactor
MSRE	Molten Salt Reactor Experiment
ORNL	Oak Ridge National Laboratory
RANS	Reynolds Averaged Navier-Stokes
SGS	sub-grid scale

Greek symbols

α	laminar thermal diffusivity
α_t	turbulent thermal diffusivity
α_{eff}	effective thermal diffusivity
β_d	total delayed neutrons fraction ($\sum_k \beta_{d,k}$)
$\beta_{d,k}$	k-th family delayed neutrons fraction

β_h	total decay heat prec. fraction ($\sum_l \beta_{h,l}$)
$\beta_{h,l}$	l-th family decay heat prec. fraction
β_n	(square root of) n-th eigenvalue
β_T	vol. thermal expansion coeff.
Δy^*	characteristic wall length
Δ	desorption number
δ	desorption rate constant
δ_ϕ	wall region thickness
γ	deposition velocity
γ_r	heat removal coefficient
λ_C	particle decay constant
$\lambda_{d,k}$	k-th family del. neutron prec. decay constant
$\lambda_{h,l}$	l-th family decay heat prec. decay constant
ρ	fluid density
$\Sigma_{a,g}$	g-th group absorption cross-section
$\Sigma_{f,g}$	g-th group fission cross-section
$\Sigma_{r,g}$	g-th group, r-th neutron reaction cross-section
$\Sigma_{r,g}^0$	reference g-th group, r-th neutron reaction cross-section
$\Sigma_{r,g}^T$	reference g-th group, r-th neutron reaction cross-section log. coeff.
$\Sigma_{s,g\to h}$	g-to-h-th group scattering cross-section
$\Sigma_{s,g\to h}^0$	reference g-to-h-th group scattering cross-section
$\Sigma_{s,g\to h}^T$	reference g-to-h-th group scattering cross-section log. coeff.
$\chi_{d,g}$	g-th energy group delayed neutron spectrum
$\chi_{p,g}$	g-th energy group prompt neutron spectrum
$\bar{\nu}_g$	avg. g-th group neutrons emitted per fission
ν	laminar kinematic viscosity

ν_{eff}	effective kinematic viscosity
ν_t	turbulent kinematic viscosity
ϕ	particle-wall interaction potential
φ_g	g-th group integrated neutron flux

Latin symbols

$\hat{C}$	non-dim. particle (vol.) concentration
$\hat{C}_d$	non-dim. deposited particle (surf.) conc.
$\hat{C}_{in}$	non-dim. inlet particle (vol.) concentration
C	particle (vol.) concentration
C_0	ref. particle (vol.) concentration
C_d	deposited particle (surf.) concentration
C_{in}	inlet particle (vol.) concentration
c_k	k-th family del. neutron prec. (vol.) concentration
c_p	specific heat capacity
D	laminar particle diffusivity
D_t	turbulent particle diffusivity
D_{eff}	effective particle diffusivity
D_{eff}^{∞}	bulk effective particle diffusivity
$D_{n,g}$	g-th group neutron diffusion coefficient
$D_{n,g}^0$	reference g-th group neutron diffusion coefficient
$D_{n,g}^T$	reference g-th group neutron diffusion coefficient log. coeff.
d_l	l-th family decay heat prec. (vol.) concentration
d_p	particle diameter
Da	Damköhler number
$\bar{E}_{f,g}$	avg. g-th group fission energy
f	channel aspect ratio

F_D	particle diffusivity correction factor
$\mathbf{g}$	gravitational acceleration
H	channel half-width
J_d	particle (surf.) deposition flux
k_B	Boltzmann constant
k_{eff}	effective multiplication factor
L	channel length
M	confluent hypergeometric function
p	fluid pressure
Pe	Péclet number
Pr	Prandtl number
Pr_t	turbulent Prandtl number
q'''	vol. energy source
Re	Reynolds number
$\bar{S}$	average particle (vol.) source
$\hat{S}$	non-dim. particle (vol.) source
$\tilde{S}$	unit-average particle (vol.) source
S	particle (vol.) source
S_{max}	max. particle (vol.) source
S_{min}	min. particle (vol.) source
Sc	Schmidt number
Sc_t	turbulent Schmidt number
Sh	Sherwood number
T	fluid temperature
T_0	reference temperature (buoyancy)
T_0^Σ	reference temperature (cross-sections)
T_{sink}	heat sink temperature

$\hat{u}$	non-dim. longitudinal velocity comp.
$\mathbf{u}$	fluid velocity
u	longitudinal velocity comp.
u_m	maximum profile velocity
v_g	avg. g-th group neutron velocity
V_r	heat removal region volume
$\hat{x}$	non-dim. longitudinal coord.
x	longitudinal coordinate
$\hat{y}$	non-dim. transversal coord.
y	transversal coord.
y_C	fission yield of transported fission product

Chapter 1

Introduction

Research on liquid-fuel reactor concepts has gained renewed interest over the last decade. Among them, the Molten Salt Reactor (MSR) and, in particular, the fast spectrum MSFR (Molten Salt Fast Reactor) has obtained a leading role as one of the selected Generation IV reference technologies [46]. The adoption of a circulating liquid fuel, in conjunction with the fast neutron spectrum, makes the MSFR system unique from the design and modelling viewpoints. Internal heat generation, fuel thermal feedback and transport of delayed neutron precursors and fission products lead altogether to a strong intrinsic coupling between thermal hydraulics, neutronics and fuel chemistry. Reactor modelling efforts have therefore shifted towards full-core and multiphysics analysis to meet the requirements and complexity of physical and computational models for the MSFR. A comprehensive account of state-of-the-art multiphysics modelling tools for the MSFR can be found in [49]. Multiphysics simulation codes have been successfully employed to investigate several MSFR features, such as for instance the adoption of a bubbling system [13, 14], fuel compressibility effects [12], the analysis of freeze-valve behaviour [48]. Multiphysics-based MSFR models have also been adopted to test the application of advanced data analysis and model order reduction techniques [21, 17].

Fission products (FPs) represent a major challenge in the modelling and design of the MSFR. They originate within the fuel and are not retained by solid structures, being thus free to be carried by the liquid fuel along the primary circuit. Some FP species are not expected to form stable compounds with the constituents of the fuel salt mixture [22, 3] and therefore may give rise to separate phases, either in the form of solid precipitates or gas bubbles. Solid FPs are likely to deposit on reactor surfaces in the form of solid precipitates [28, 15], giving rise to potential issues such as formation of localised decay heat sources as well as deterioration of heat exchanger performance. Surface deposits might also pose a serious radiological threat in inspection/maintenance operations. In a similar way, the oxidation of fissile species in particular operating conditions might lead to the formation of solid precipitates [6], with potential issues related to the transport and local accumulation of fissile particles.

1.1 Objectives, motivation and outline

The analysis of FPs transport has found limited space in recent MSFR studies. In this regard, there has been some effort on modelling the behaviour and effects of Xenon transport in MSRs [43, 11], while the analysis of metallic FPs in the context of a multiphysics system code for the study of the Molten Salt Reactor Experiment has been recently addressed by [51]. The analysis of the MSFR by means of a traditional system-code approach is made difficult by its peculiar geometry and fuel circulation, making the use of high-fidelity models a more appropriate choice. Local temperature effects on precipitation of metallic species can also be directly taken into account, in view of coupling with thermochemistry calculations [35].

The subject of this work is therefore the integration of transport models for solid FPs in state-of-the-art MSFR multiphysics tools, and to perform a preliminary analysis of FPs transport and deposition in relevant simplified MSFR cases. The development platform is the C++ open-source finite-volume CFD library OpenFOAM [39]. Due to their direct effect on species transport, different turbulence modelling approaches are tested in a more realistic MSFR case. Such approach is intended to allow for the analysis of inherently two- and three-dimensional effects, such as transport in complex turbulent flows, the estimation of particle deposition fluxes directly from concentration fields and the interaction with the gas bubbling system. Local temperature effects on precipitation of metallic species can also be directly taken into account, in view of coupling with thermochemistry calculations [35]. Turbulence modelling plays a significant role in the prediction of transported quantities such as fission products, especially for complex three-dimensional geometries. The employment of different turbulence modelling approaches should be considered to assess their influence on FPs distribution and deposition within the reactor. Therefore, different models based on the standard Reynolds-averaging (RANS) approach are used to assess turbulent transport of FPs, and more sophisticated techniques such as Large Eddy Simulation (LES) are also considered for the future extension of predictive capabilities of MSFR multiphysics tools.

The remainder of this thesis is organised as follows. In Chapter 2 the developed multiphysics approach is described. Then, its implementation in OpenFOAM is verified against analytical solutions for simplified test cases. The analytical solutions are derived from the well-known Graetz problem, which is here formulated for a general case with distributed source terms, linear decay and mixed-type boundary conditions. To the authors knowledge, such form of the Graetz problem has not been addressed in detail in the literature, and therefore the complete derivation is reported. The influence of some key model parameters is discussed, and corresponding solutions from the OpenFOAM and analytical models are presented and compared.

Chapter 3 is devoted to the preliminary analysis of FPs transport and deposition in relevant two-dimensional MSFR cases. Potential numerical issues arising from the commonly adopted "perfect adsorption" wall boundary conditions are addressed. Analytical results from Chapter 2 are also used to illustrate such issues, and are compared to numerical simulation in a lid-driven cavity. Then, due to their direct effect on species transport, different turbulence modelling approaches are tested in a more realistic two-dimensional MSFR case.

In Chapter 4, a preliminary LES 3D model of the MSFR is presented. Different LES turbulence closure models are tested in transient simulation to study the free dynamics of the MSFR evolving from initial RANS steady-state conditions, and highlighting the coupled effect of large-scale turbulence fluctuations on the different physics and relevant integral properties of the reactor.

Finally, Chapter 5 reports some conclusive remarks and suggestions for possible future extensions of the work.

1.2 The Molten Salt Fast Reactor

The Molten Salt Fast Reactor is conceived as a nuclear reactor for commercial power production, with a thermal output of the order of 3000 $\mathrm{MW_{th}}$. Its major design feature is the adoption of a liquid fuel, resulting in several potential advantages with respect to more traditional reactor designs:

- compact design, with low fuel inventory
- homogeneous fuel, with no need of fuel loading plan
- direct production of heat within the coolant, with no heat transfer from solid fuel elements
- possibility of online fuel reprocessing, with no need of reactor shutdown and more optimised usage of fissile/fertile resources and higher burnup
- intrinsic safety thanks to large negative temperature feedback
- good breeding ratio and reduced initial fissile inventory

Among liquid fuel carriers, fluoride salts have been chosen as they fulfil all main constraints and desiderata: they have relatively low melting temperatures and vapour pressures, high boiling points, good thermal properties and stability under irradiation. Furthermore, they are fairly transparent to neutrons and show good solubility of fissile/fertile elements.

Nuclear reactors with circulating fuels also show rather unique neutronics features. For instance, delayed neutrons are produced in a non negligible fraction outside the core region as the fuel is continuously extracted for cooling. Therefore the core mass flow rate has a strong impact on reactivity and reactor dynamics and control [1].

Conversely, liquid fuels present one of the most formidable challenges in terms of reactor design, analysis and operation. The Oak Ridge National Laboratory (ORNL) extensively focused on researching MSR technology for energy production during the ‘50s and ‘60s. The most remarkable outcome of these efforts was the successful operation of the Molten Salt Reactor Experiment (MSRE) and the design of the Molten Salt Breeder Reactor (MSBR) [34]. Despite these positive experiences, the Molten Salt

Reactor Project was discontinued in the ‘70s and, unfortunately, the MSBR was never constructed.

The MSFR design is continuously evolving and research activities are ongoing in the framework of the H2020-Euratom project SAMOSAFER (`https://samosafer.eu`). Details about the MSFR concept can be found e.g. in [46] and the related bibliography.

Chapter 2

The Multiphysics Model

The results presented in this Chapter have been published in:

Di Ronco, A., et al. "An Eulerian Single-Phase Transport Model for Solid Fission Products in the Molten Salt Fast Reactor: Development of an Analytical Solution for Verification Purposes". *Frontiers in Energy Research*, vol. 9, 2021, https://doi.org/10.3389/fenrg.2021.692627.

In this Chapter, the multiphysics solver adopted for the analysis of solid FPs transport is described. All the relevant equations are reported, with particular detail on the implementation of the transport equations for solid FPs. Then, the model implementation is verified against a simplified analytical model derived ad-hoc.

2.1 The OpenFOAM library

The OpenFOAM framework [39, 53] is used as the development platform for the implementation of the numerical solver. It consists of a set of C++ libraries that offer automated matrix construction and solving capabilities for scalar and vector equations, employing state-of-the-art Finite Volume Methods (FVM) with user-defined discretisation and interpolation schemes. Thanks to its flexibility and high-level programming interface that make it suitable for modelling complex coupled problems, OpenFOAM has seen widespread application in CFD analysis, both in academia and industry. A remarkable aspect of the OpenFOAM framework is the close resemblance between its high-level C++ representations of continuum mechanics equations and their corresponding mathematical counterparts. All model equations are solved sequentially, following an iterative segregated coupling approach. For instance, the OpenFOAM implementation of the following vector equation,

$$\frac{\partial(\rho\mathbf{U})}{\partial t} + \nabla\cdot(\rho\mathbf{U}\mathbf{U}) - \nabla\cdot(\mu\nabla\mathbf{U}) = -\nabla p, \tag{2.1}$$

would be similar to the following code:

```
solve
(
    fvm::ddt(rho, U)
  + fvm::div(phi, U)
  - fvm::laplacian(mu, U)
    ==
  - fvc::grad(p)
);
```

where `fvm` and `fvc` respectively indicate separate C++ namespaces for implicit and explicit finite-volume method calculations, while `phi` is an OpenFOAM device used to describe the face flux field computed starting from the $\rho\mathbf{U}$ product. Equations constituting numerical solvers can be easily modified or extended to include additional physical terms, requiring only a relatively basic understanding of C++.

In addition to the simplicity with which the constitutive equations of various physical phenomena can be constructed, OpenFOAM is shipped with a variety of pre-built models and solvers for the modelling of fluid flows. Pre-built validated solvers range from single-phase incompressible/compressible thermal flows to reactive multiphase eulerian/lagrangian transport problems. For instance, the backbone of a C++ application for solving a basic incompressible transient flow would resemble the following code:

```
int main()
{
    while (run())
    {
        time++;

        // --- Pressure-velocity corrector loop
        while (loop())
        {
            #include "UEqn.H"

            // --- Pressure corrector loop
            while (correct())
            {
                #include "pEqn.H"
            }
        }
    }

    return 0;
}
```

where it is evident that, at each time step, the code blocks which solve for the velocity (`UEqn.H`) and pressure (`pEqn.H`) equations are invoked multiple times within nested iteration loops, based on the standard practice for coupled pressure-velocity solution in CFD codes. The `run()`, `loop()` and `correct()` functions are indeed responsible for checking exit conditions of iteration loops at different solution phases, based on user-defined convergence/stopping criteria. Additional equations can be assembled, included and solved according to different coupling strategies, offering a flexible environment for the construction of multiphysics solvers.

Originally developed for the transient analysis of the MSFR [2], the adopted multiphysics solver was recently extended to allow for the study of compressibility effects during super-prompt-critical transients [13] and of the bubbling system [12, 11]. The version employed in this work features single-phase incompressible thermal hydraulics, multi-group neutron diffusion and transport equations for delayed neutron and decay heat precursors. Transport equations for fission products are solved alongside the other physical modules, to provide a fully-coupled multiphysics simulation.

2.2 Thermal hydraulics model

Continuity, momentum and energy (in temperature form) conservation equations are expressed in a single-phase incompressible formulation:

$$\nabla \cdot \mathbf{u} = 0 \tag{2.2}$$

$$\begin{aligned} \frac{\partial \mathbf{u}}{\partial t} + \nabla \cdot (\mathbf{u}\mathbf{u}^T) = -\frac{1}{\rho}\nabla p + [1 - \beta_T (T - T_0)]\,\mathbf{g} \\ + \nabla \cdot \left[\nu_{eff} \left(\nabla \mathbf{u} + (\nabla \mathbf{u})^T\right)\right] \end{aligned} \tag{2.3}$$

$$\frac{\partial T}{\partial t} + \nabla \cdot (\mathbf{u}T) = \nabla \cdot (\alpha_{eff} \nabla T) + \frac{q'''}{\rho c_p} \tag{2.4}$$

where the quantities $\mathbf{u}$, p and T, which correspond to velocity, pressure and temperature, respectively, are intended as averaged in the sense of Reynolds-Averaged Navier-Stokes modelling. It follows that turbulence modelling is performed by means of standard eddy-viscosity based closure models, such as the well-known k-ε model [31], for which effective momentum and thermal diffusivities can be expressed as the sum of a laminar and a turbulent contribution:

$$\nu_{eff} = \nu + \nu_t \tag{2.5}$$

$$\alpha_{eff} = \alpha + \alpha_t = \frac{\nu}{Pr} + \frac{\nu_t}{Pr_t} \tag{2.6}$$

where Pr and Pr_t are the Prandtl and turbulent Prandtl numbers, respectively. Momentum and energy equations are coupled thanks to the Boussinesq approximation, for which the density value driving the buoyancy term in (2.3) is linearised around a reference temperature T_0 and β_T represents the volumetric thermal expansion coefficient of the fluid. Except for what concerns density in the linearised buoyancy term, constant average values are used for thermophysical properties to keep the numerics and the coupling between different physics as simple as possible. Finally, q''' represents a volumetric energy source which includes internal heat generation (both prompt and delayed) and optionally other energy sinks to model heat removal systems.

Pressure-velocity coupling is performed through the standard SIMPLE/PISO algorithms [40, 25].

2.3 Neutronics model

The multi-group diffusion model is adopted for neutron flux calculations [24]. Despite some limitations, it is widely employed in standard nuclear reactor analysis. Thanks to its relative simplicity and limited computational effort, it has found several successful applications especially for multiphysics analysis [2, 20]. More recent works have also proposed the extension of OpenFOAM-based multiphysics codes to more advanced neutron transport approaches, e.g. the SP3 model [19, 13]. The diffusion equation for the g-th group-integrated neutron flux φ_g reads:

$$\frac{1}{v_g}\frac{\partial \varphi_g}{\partial t} = \nabla \cdot (D_{n,g} \nabla \varphi_g) + \left[(1-\beta_d)\chi_{p,g}\frac{\bar{\nu}_g}{k_{eff}}\Sigma_{f,g} - \Sigma_{a,g} - \sum_{h \neq g} \Sigma_{s,g\to h} \right] \varphi_g + S_{n,g} \tag{2.7}$$

where $S_{n,g}$ is the explicit neutron source of the g-th group, constituted by prompt fission and scattering neutrons from other groups and delayed neutron precursors decay:

$$S_{n,g} = (1-\beta_d) \sum_{h \neq g} \chi_{p,h} \frac{\bar{\nu}_h}{k_{eff}} \Sigma_{f,h}\, \varphi_h + \sum_{h \neq g} \Sigma_{s,h\to g}\, \varphi_h + \chi_{d,h} \sum_k \lambda_{d,k} c_k \tag{2.8}$$

The presence of φ_h in the explicit source term $S_{n,g}$ couples the transport equations for different energy groups, which are therefore dealt with following a segregated iterative approach. Most symbols have straightforward meaning and are listed in the Nomenclature section. It is worth mentioning that k_{eff} acts as a tunable multiplication factor to model a prescribed reactivity insertion. A power-iteration routine based on the k-eigenvalue method is also included for steady-state simulation, which allows for the iterative adjustment of k_{eff} to attain criticality at a specified power level.

Albedo boundary conditions [24] have been applied to both the radial wall (blanket salt) and the upper and lower limits of the core (axial reflectors) in order to further decrease the computational cost of the simulations. This reduces the computational effort needed by limiting the solution of the neutron diffusion equation to the fuel salt circuit.

Due to the circulating nature of the fuel, transport equations are formulated also for delayed neutron and decay heat precursors. The transport equation for the concentration of delayed neutron precursors of the k-th family c_k reads:

$$\frac{\partial c_k}{\partial t} + \nabla \cdot (\mathbf{u}\, c_k) = \nabla \cdot (D_{eff}\, \nabla c_k) - \lambda_{d,k}\, c_k + \beta_{d,k} \sum_g \bar{\nu}_g\, \Sigma_{f,g}\, \varphi_g \tag{2.9}$$

A discussion on the diffusion coefficient D_{eff} is given in Section 2.4. An analogous equation holds for the concentration of decay heat precursors of the l-th family d_l:

$$\frac{\partial d_l}{\partial t} + \nabla \cdot (\mathbf{u}\, d_l) = \nabla \cdot (D_{eff}\, \nabla d_l) - \lambda_{h,l}\, d_l + \beta_{h,l} \sum_g \bar{E}_{f,g}\, \Sigma_{f,g}\, \varphi_g \tag{2.10}$$

In the above equation, the actual concentration of decay heat precursors is multiplied by the average fission energy, such that d_l represents a volumetric amount of “latent” fission energy. Consistently, the volumetric heat source is given by:

$$q''' = (1 - \beta_h) \sum_g \bar{E}_{f,g}\, \Sigma_{f,g}\, \varphi_g + \sum_l \lambda_{h,l}\, d_l \tag{2.11}$$

.

2.3.1 Calculation of group constants

In order to account for thermal feedback on neutronics, the model includes a dependency of the cross sections on fuel temperature and density. The Doppler effect, in particular, is given by a logarithmic dependence of the fuel capture and fission cross sections, which was estimated by interpolating Monte Carlo runs at different fuel temperatures. Even though the fluid fuel is considered incompressible as far as thermal hydraulics is concerned (except for the linearised buoyancy term), a linear dependence on local temperature is considered to capture the effects of thermal expansion on nuclear properties.

Group constants are therefore adjusted as functions of local temperature around reference values to account for Doppler and fuel density effects. For a generic neutron reaction r occurring in the g-th energy group:

$$\Sigma_{r,g} = \left(\Sigma^0_{r,g} + \Sigma^T_{r,g} \log \frac{T}{T^\Sigma_0} \right) \frac{1 - \beta_T\,(T - T_0)}{1 - \beta_T(T^\Sigma_0 - T_0)} \tag{2.12}$$

where Doppler effects are modelled by means of a logarithmic term where $\Sigma^0_{r,g}$ and $\Sigma^T_{r,g}$ respectively represent the cross-section and a corresponding logarithmic coefficient at a reference temperature T^Σ_0, whereas density effects are taken into account through a linear correction consistently with the buoyancy term. The reference temperature for cross-sections can be chosen independently from T_0. An analogous approach is employed for the correction of the intra-group neutron diffusion coefficient $D_{n,g}$.

The group constants $\Sigma^0_{r,g}$ and $\Sigma^T_{r,g}$, as well as equivalent terms for diffusion coefficients, have been derived using the Monte Carlo reactor physics and burnup code SERPENT 2 [32] with the JEFF-3.1 evaluated nuclear data library [30]. Serpent is able to perform steady-state neutronics calculations on arbitrarily complex models based on constructive solid geometry (CSG). Group constant generation for reactor analysis codes was one of the original purposes for SERPENT. It is able to generate all the input parameters required for reactor calculations, such as homogenised macroscopic reaction cross sections, isotopic microscopic cross sections, diffusion coefficients and delayed neutron parameters. Most parameters are calculated using conventional Monte Carlo tallies.

Since the typical use case for SERPENT dictates the specification of a single temperature for each zone/material, the calculation must be repeated for different temperature conditions. Then, the sets of group constants generated at different temperatures can be post-processed to produce ad-hoc interpolation parameters. This simplified approach has shown the capabilities to describe the spatial and time dependence of neutron fluxes in the MSFR with a good degree of accuracy [2], making it a preferable tool for CFD-based multiphysics calculations.

2.4 Fission products transport model

Similarly to other transported scalar quantities, each fission product specie is modelled as a continuous scalar concentration field subject to advection, diffusion and decay mechanisms:

$$\frac{\partial C}{\partial t} + \nabla \cdot (\mathbf{u}\, C) = \nabla \cdot (D_{eff} \nabla C) - \lambda\, C + y_C \sum_g \Sigma_{f,g}\, \varphi_g \tag{2.13}$$

where C is the concentration of the species under consideration, expressed in number of particles per unit volume. D_{eff} is the total particle diffusivity, $\mathbf{u}$ is the carrier velocity field and λ represent the decay constant of a fission product specie. Since chemical interactions between species and formation of separate phases are neglected, the source term can be simply related to the fission rate through a suitable yield coefficient y_C.

As previously mentioned, this modelling choice is motivated by the need to limit the overall complexity and computational requirements of the MSFR, and to easily integrate such models in state-of-the-art MSFR codes. The single-phase Eulerian approach can still represent a valid approximation, provided that some conditions are met. Theoretical and experimental analysis has suggested that Fick's diffusion law only applies when inertial effects are negligible, and that particles inertia plays an increasingly dominant role in transport mechanisms as particles size increases [33, 23]. Little information is known about the expected size of fission product particles in the MSFR, but previous experience with MSRs suggests formation of colloidal suspensions (i.e. with particle diameters approx. between 10^{-9} m and 10^{-6} m) should be expected [15] and that simple diffusion laws may apply, at least as a first approximation. The other main condition requires the particle concentration in the carrier fluid to be sufficiently low to make all interactions between each particle and the fluid, or among particles themselves, negligible. Provided that such conditions are met, the adoption of more sophisticated approaches, e.g. Eulerian-Eulerian multiphase or Eulerian-Lagrangian, may prove little benefit at the expense of a much more complex modelling framework.

As regards the particle diffusivity, it is commonly assumed that the diffusivity coefficient D_{eff} may be separated in a laminar and a turbulent contribution, analogously to (2.6):

$$D_{eff} = D + D_t = \frac{\nu}{Sc} + \frac{\nu_t}{Sc_t} \tag{2.14}$$

where Sc and Sc_t are Schmidt and turbulent Schmidt numbers, respectively. The particle size can be used to derive a common expression for the laminar diffusivity D, which is given by the so-called Stokes-Einstein equation:

$$D = \frac{k_B T}{3\pi\rho\nu d_p} \tag{2.15}$$

where k_B is the Boltzmann constant and d_p is the particle diameter. The above equation is derived under the assumption of large Schmidt number Sc [4] and can be used to estimate Sc in such limit:

$$Sc = \frac{3\pi\rho\nu^2 d_p}{k_B T} \tag{2.16}$$

It is worth mentioning that particle size plays a relevant role in determining particle diffusivity, according to the Stokes-Einstein relation. Particles sizes are determined by complex nucleation and growth mechanisms. Furthermore, size influences the relative role of inertial effects on momentum transport, invalidating the assumption of gradient-driven turbulent transport above certain diameter values. For the sake of simplicity, these modelling aspects are here neglected.

2.4.1 Deposition modelling

Besides particle transport in the bulk flow, transport mechanisms which lead to deposition need to be addressed separately. First of all, when particle-wall interaction in the boundary layer is considered, a variable diffusion coefficient can be introduced to model hydrodynamic interactions between particles and solid walls [8]. In such case, D_{eff} is assumed as a function of the particle-wall distance:

$$D_{eff} = D_{eff}(y) \tag{2.17}$$

where y denotes the wall-distance in the normal direction in a boundary layer flow. Moreover, it is commonly accepted that D_{eff} is mostly constant in the bulk of the flow and abruptly decreases in a very small layer close to walls. For this reason it can be assumed

$$D_{eff}(y) = F_D(y) D_{eff}^{\infty} \tag{2.18}$$

where D_{eff}^{∞} is a constant bulk diffusivity and $F_D(y)$ a correction factor which is always comprised within 0 and 1 [8].

Moreover, to model deposition mechanisms and formulate appropriate boundary conditions for the particle concentration field, one possible approach is the inclusion in the transport equation of a particle-wall interaction forcing term based on an interaction potential energy ϕ [45, 7]. Since boundary layer flows are inherently two-dimensional, close to a generic wall the steady-state transport equation reads

$$D_{eff}(y)\frac{\partial^2 C}{\partial x^2} + \frac{\partial}{\partial y}\left(D_{eff}(y)\frac{\partial C}{\partial y} + \frac{D_{eff}(y)}{kT}\frac{\mathrm{d}\phi}{\mathrm{d}y}C\right) - u(y)\frac{\partial C}{\partial x} - \lambda C + S = 0 \tag{2.19}$$

where x and y here denote the longitudinal and transversal directions. This approach is general but introduces significant complication in the general problem. It is therefore beneficial, when possible, to decouple the advection-diffusion and deposition problems.

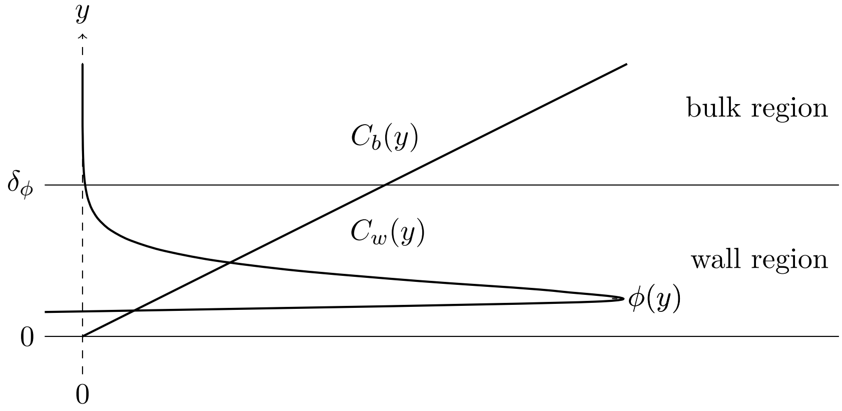

Figure 2.1: Decoupling of the transport and deposition problems: solutions for the wall region (C_w) and the bulk region (C_b) are obtained separately and joined by imposing interface continuity on particle concentration and particle flux at $y = \delta_\phi$. The wall region thickness $\delta_\phi \ll H$ is defined as the distance at which $\phi(\delta_\phi)$ becomes arbitrarily small.

When the energy potential ϕ and the hydrodynamic interaction effects are significant only over distances of the order of the particle size, this can be effectively achieved by dividing the boundary layer is divided in two regions (Figure 2.1): the bulk region, where advection occurs and interactions are negligible, and a very thin wall region, where advection is negligible and deposition processes take place. The two regions are subject to an interface condition, which equates the particle concentration $C(\delta_\phi)$ and its flux at a certain distance δ_ϕ from the wall (with δ_ϕ chosen such that $\phi(\delta_\phi)$ is arbitrarily small). It has been shown that, under fairly general hypotheses on ϕ, the coupled solution of the two regions may be approximated such that the wall region influence is collapsed in a first-order reaction boundary condition for the bulk region [45, 44]:

$$D_{eff}^{\infty} \frac{\partial C}{\partial y} = \gamma C, \quad y = 0 \tag{2.20}$$

where

$$\gamma = D_{eff}^{\infty} \left[\int_0^{\delta_\phi} \left(F_D(y)^{-1} e^{\phi(y)/kT} - 1 \right) \mathrm{d}y \right]^{-1} \tag{2.21}$$

The coefficient γ is therefore a constant depending on F and ϕ. In principle its value might also depend on the integration limit δ_ϕ, but it has been shown that in many circumstances its influence on the value of the integral is relatively small over a relatively broad range [44]. It should be noted that these results are derived under the assumption of negligible axial diffusion (which is commonly the case) and in absence of source terms and decay. They are, however, representative of a broad class of particle-wall interaction problems and it is here assumed that internal sources or decay phenomena do not alter significantly such behaviour.

In the general three-dimensional case, the wall boundary condition can be written as

$$-D^{\infty}_{eff}\nabla C \cdot \mathbf{n} = \gamma\, C \tag{2.22}$$

for any point on the wall boundary, where **n** denotes the outward pointing wall-normal direction. In this model, wall adsorption of fission product particles is modelled through a single deposition parameter γ, which has the physical dimensions of a velocity. The assumption of "perfectly adsorbing" walls is adopted, i.e. γ is let to tend to infinite such that the wall boundary condition simplifies to

$$C = 0 \tag{2.23}$$

In this way, conservative estimates of deposition fluxes are obtained. This represents indeed a major approximation, but it is widely adopted in the literature of CFD-based particle transport problems. Moreover, system-code approaches which follow fluid dynamic analogy with momentum transport are in general not feasible due to non-standard geometries found in MSFR cases.

Since particle-wall interactions are modelled by means of a simple first-order boundary condition, the deposited quantities can easily tracked by solving

$$\frac{\partial C_d}{\partial t} = -\lambda C_d + \gamma C \tag{2.24}$$

where C_d represents the surface concentration of deposited particles on the wall boundary, expressed in number of particles per unit area. Desorption mechanisms can be included as well by adding a corresponding term (2.24),

$$\frac{\partial C_d}{\partial t} = -(\lambda + \delta) C_d + \gamma C \tag{2.25}$$

with δ being the desorption rate constant [55].

2.4.2 Distributed sources

Some peculiar aspects of problems involving the transport of quantities subject to deposition boundary conditions and distributed internal generation need to be discussed. Distributed internal generation represents a modelling condition which is hardly found in common particle transport problems, and its effects on the concentration boundary layer need to be carefully addressed in CFD-based calculations. In particular, it is found that when deposition boundary conditions prescribe a vanishing species concentration at wall boundaries, large concentration gradients are to be expected if non-negligible generation of particles occurs in the boundary layer. This is naturally the case in MSFR calculations, where the fission rate does not vanish at reactor boundaries.

To provide some insight, analytical solutions for the scalar transport problem defined by Equation (2.13) are found for simplified test cases. Albeit simplified, these results are useful to understand general features of expected solutions of more complex problems.

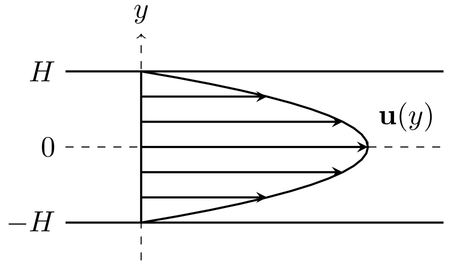

Figure 2.2: Parallel plates channel geometry: with respect to the flow, the y coordinate denotes the transversal direction. Wall boundaries are located at $y = \pm H$.

The fully-developed parallel-plates transport problem Equation (2.13) reduces to the 1D equation

$$D_{eff}\frac{\mathrm{d}^2C}{\mathrm{d}y^2} - \lambda_C C + S(y) = 0 \tag{2.26}$$

equipped with the boundary conditions

$$\mp D_{eff}\frac{\mathrm{d}C}{\mathrm{d}y} = \gamma C, \quad y = \pm H \tag{2.27}$$

Here, y denotes the coordinate in the direction transversal to the channel-flow, and H is the half-width of the channel (Figure 2.2).

The solution for a cosine-shaped source of the form

$$S(y) = S_{min} + (S_{max} - S_{min})\cos(\frac{\pi}{2H}y) \tag{2.28}$$

reads

$$\begin{aligned} C(y) = &\left(\frac{S_{max}}{\lambda_C}\right) K \left(e^{\frac{\sqrt{Da}}{H}y} + e^{-\frac{\sqrt{Da}}{H}y}\right) \\ &+ \left(\frac{S_{max}}{\lambda_C}\right)\left[\left(\frac{S_{min}}{S_{max}}\right) + \left(1 - \frac{S_{min}}{S_{max}}\right)\frac{4Da}{4Da+\pi^2}\cos(\frac{\pi}{2H}y)\right] \end{aligned} \tag{2.29}$$

where

$$K = \frac{-\left(\frac{S_{min}}{S_{max}}\right) Sh + \left(1 - \frac{S_{min}}{S_{max}}\right)\left(\frac{\pi}{2}\right)\frac{4Da}{4Da+\pi^2}}{Sh\left(e^{\sqrt{Da}} + e^{-\sqrt{Da}}\right) + \sqrt{Da}\left(e^{\sqrt{Da}} - e^{-\sqrt{Da}}\right)} \tag{2.30}$$

Non-dimensional quantities have been defined as $Sh = \gamma H/D_{eff}$ and $Da = \lambda_C H^2/D_{eff}$. Introducing some additional hypotheses, such as $Sh \gg \sqrt{Da} \gg 1$, it is possible to further simplify the solution:

$$\frac{\lambda_C C(y)}{S_{max}} = \left(\frac{S_{min}}{S_{max}}\right)\left[1 - \frac{e^{\frac{\sqrt{Da}}{H}y} + e^{-\frac{\sqrt{Da}}{H}y}}{e^{\sqrt{Da}} + e^{-\sqrt{Da}}}\right] + \left(1 - \frac{S_{min}}{S_{max}}\right)\cos(\frac{\pi}{2H}y) \tag{2.31}$$

The role of the ratio S_{min}/S_{max} appears evident when considering the two extreme cases:

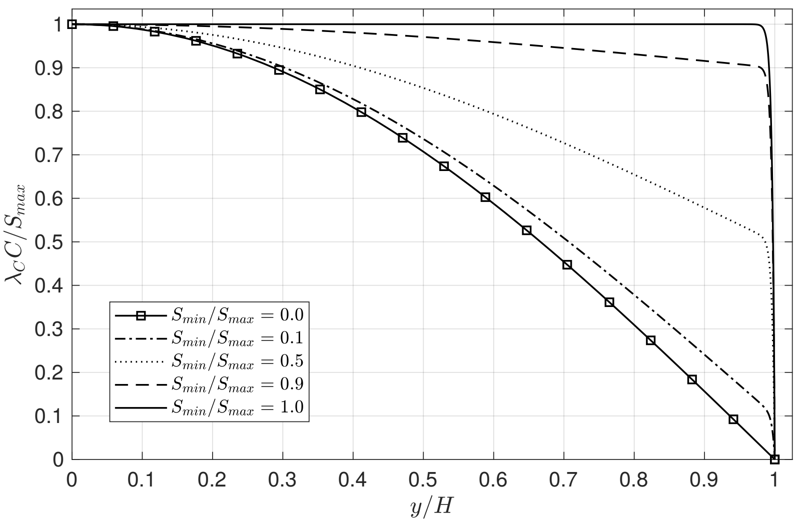

Figure 2.3: Analytical solutions for the 1D parallel plates geometry. Different S_{min} to S_{max} ratios produce similar behaviours: the concentration profiles follow a cosine-shaped profile in the bulk flow, then drop to 0 in a thin region close to the wall boundary. The thickness Δy^* shows little dependence on S_{min}/S_{max}. For these cases, $Da = 80000$.

(A) $S_{min}/S_{max} \to 0$: the concentration profile tends to a simple cosine shape:

$$\frac{\lambda_C C(y)}{S_{max}} \to \cos\left(\frac{\pi}{2H}y\right) \tag{2.32}$$

(B) $S_{min}/S_{max} \to 1$: the concentration profile tends to a uniform shape, except for a thin wall region where it quickly drops to 0:

$$\frac{\lambda_C C(y)}{S_{max}} \to 1 - \frac{e^{\frac{\sqrt{Da}}{H}y} + e^{-\frac{\sqrt{Da}}{H}y}}{e^{\sqrt{Da}} + e^{-\sqrt{Da}}} \tag{2.33}$$

Cases sufficiently far from (A) are significant for realistic reactor applications, where the "perfectly absorbing walls" condition ($Sh \gg 1$) is assumed to adequately approximate particle-wall interactions and the distributed source does not vanish close to walls. It is easily demonstrated that, in such cases, the thickness of the wall layer where the concentration drop occurs is of the order of few times the characteristic length Δy^*, defined as

$$\Delta y^* = \frac{H}{\sqrt{Da}} = \sqrt{\frac{D_{eff}}{\lambda_C}} \tag{2.34}$$

For intermediate cases, in the bulk flow the concentration profiles follow a cosine shape whose extrapolated intersection at $y = H$ depends on S_{min}/S_{max}, while they drop to 0 in the wall region much similarly to the limiting case (B) (Figure 2.3). The thickness

Δy^* shows little dependence on S_{min}/S_{max} (except for cases very close to (A)), while mainly depends on physical parameters as described by Equation (2.34).

For realistic physical parameters values, Equation (2.34) predicts Δy^* values of the order of 10^{-3} m or even less. Despite being strictly valid for simplified problems, these results offer a useful tool to understand the typical behaviour of local concentration profiles close to walls also in more realistic cases. As anticipated, steep concentration gradients are therefore expected whenever homogeneous-Dirichlet-like boundary conditions are used in combination with distributed sources which do not vanish in the wall region. Particle deposition calculations in liquid-fuel reactors such as the MSFR fall under such conditions, and are therefore affected by relevant numerical consequences, as described in Chapter 3, since a grid size of the order of Δy^* or less is needed to correctly resolve the wall layer. Wall gradients - and therefore the ability to resolve them - play a crucial role in determining the flux of deposited particles towards walls. From Equation (2.22), the local deposition flux is defined as

$$J_d = -D_{eff} \nabla C \cdot \mathbf{n} \tag{2.35}$$

and, from a simple steady-state balance, the corresponding surface concentration of deposited particles reads

$$C_d = -\frac{D_{eff}}{\lambda_C} \nabla C \cdot \mathbf{n} \tag{2.36}$$

2.4.3 Precipitation chemistry

Solid FPs are constituted by “noble metal” species (Mo, Rh, Ru, Pd, Tc and possibly others) which are expected to be normally found exclusively in solid precipitate phase within the chemical environment of the MSFR [6]. Presence of solute should be negligible in most cases, but temperature-dependent coexistence with precipitate might be relevant in particular circumstances such as accidental scenarios. In this work, the implementation of a simplified equilibrium thermochemistry model is considered. Albeit simple, this approach can mimic the effects due to local temperature. More advanced approaches can be considered as well, such as the coupling with external thermochemistry codes [35]. The local equilibrium hypothesis allows for the solution of algebraic constraint equations instead of altering the differential transport equations with stiff non-linear reaction terms. Following common practice in CFD-thermochemistry coupling for reactive transport problems [10], a segregated approach using temperature-dependent linear equilibrium constraints has been selected. A simple precipitation-dissolution reaction involving single metallic species is considered

$$M + nUF_4 \rightleftharpoons MF_n + nUF_3 \tag{2.37}$$

$$\left[M^{n+}\right] = K(T) \left(\frac{\left[U^{4+}\right]}{\left[U^{3+}\right]} \right)^n \tag{2.38}$$

where M denotes a generic metallic species and square brackets indicate concentrations (it is assumed for simplicity that chemical activity coincides with concentration). The

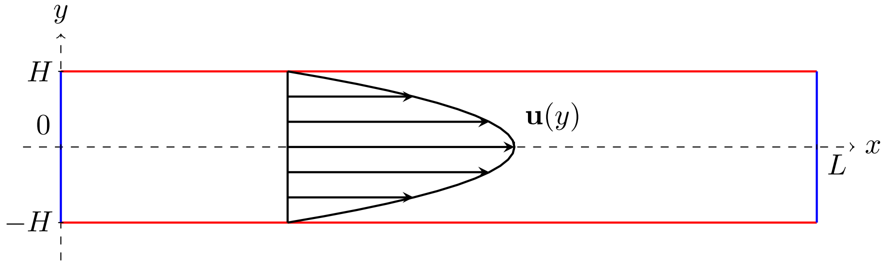

Figure 2.4: Parallel plates geometry: with respect to the flow, the x and y coordinates denote the longitudinal and transversal directions. Inlet and outlet boundaries are located at $x = 0$ and $x = L$ respectively, while wall boundaries are located at $y = \pm H$.

UF_4-to-UF_3 ratio can be considered as a design parameter, here assumed equal to 100 [6]. For simplicity, the stoichiometric coefficient n is set equal to 1. Following this approach, the particle concentration C can be split into precipitated and dissolved contributions:

$$C = C^p + C^s \tag{2.39}$$

where, in this context, C^s coincides with $[M^{n+}]$ up to a multiplicative constant. The temperature dependence of the equilibrium constant $K(T)$ is assumed exponential, following a standard Van ‘t Hoff equation:

$$\log \frac{K(T_2)}{K(T_1)} = \frac{\Delta H^0}{R} \left(\frac{1}{T_1} - \frac{1}{T_2} \right) \tag{2.40}$$

where ΔH^0 denotes a standard reaction enthalpy and R is the universal gas constant.

2.5 Analytical verification

In this Section the implemented FP transport model are verified against the analytical solution for a simplified case. A two-dimensional channel between parallel plates is considered (Figure 2.4). The particle transport model is decoupled from neutronics and heat transfer models. The source term S from (2.13) is therefore specified explicitly, and a steady-state isothermal laminar flow is considered.

The problem here considered resembles the well-known Graetz problem, for which different solutions are available in the literature. An exhaustive treatment of the Graetz theory applied to particle transport problems is given by [7], although it doesn't consider linear decay or distributed source terms. It is indeed difficult to find, in the literature, realistic applications which consider simultaneously, as in the case under consideration, distributed internal sources, decay reactions and mixed type boundary conditions. Corresponding analytical solutions for this specific problem are not found in the literature, and are therefore derived in the following.

2.5.1 Momentum equation

Analytical solutions of the momentum equation can be found only for simple steady-state fully-developed laminar flow problems. In such a case, the well known parabolic solution reads

$$\mathbf{u} = \begin{bmatrix} u(y) \\ 0 \end{bmatrix} \tag{2.41}$$

with

$$u(y) = u_m \left(1 - \frac{y^2}{H^2}\right) \tag{2.42}$$

where u_m is the maximum profile velocity and H is half the channel width as depicted in Figure 2.4.

2.5.2 Particle concentration equation

The boundary value problem then becomes, in explicit cartesian coordinates,

$$\begin{cases} D\left(\dfrac{\partial^2 C}{\partial x^2} + \dfrac{\partial^2 C}{\partial y^2}\right) - u(y)\dfrac{\partial C}{\partial x} - \lambda C + S = 0 \\ -(\lambda+\delta)C_d + \gamma C = 0, \quad y = \pm H \\ \mp D\dfrac{\partial C}{\partial y} = \gamma C - \delta C_d, \quad y = \pm H \end{cases} \tag{2.43}$$

where D is used, from now on, to denote the constant bulk diffusivity. Boundary conditions for the x-direction are discussed later. The problem is conveniently re-scaled by defining appropriate non-dimensional quantities:

$$\begin{aligned} \hat{x} &= \frac{x}{L} \\ \hat{y} &= \frac{y}{H} \\ \hat{u}(\hat{y}) &= \frac{u(H\hat{y})}{u_m} = 1 - \hat{y}^2 \\ \hat{C}(\hat{x},\hat{y}) &= \frac{C(L\hat{x}, H\hat{y})}{C_0} \\ \hat{C}_d(\hat{x}) &= \frac{C_d(L\hat{x})}{HC_0} \\ \hat{S}(\hat{x},\hat{y}) &= \frac{H^2}{D}\frac{S(L\hat{x}, H\hat{y})}{C_0} \end{aligned}$$

where C_0 is a concentration value typical of the problem. The equations are then rewritten as

$$\begin{cases} f^2\dfrac{\partial^2\hat{C}}{\partial\hat{x}^2}+\dfrac{\partial^2\hat{C}}{\partial\hat{y}^2}-f\,Pe\,\hat{u}(\hat{y})\dfrac{\partial\hat{C}}{\partial\hat{x}}-Da\hat{C}+\hat{S}=0 \\ \hat{C}_d=\dfrac{Sh}{Da+\Delta}\hat{C}, \quad \hat{y}=\pm 1 \\ \mp\dfrac{\partial\hat{C}}{\partial\hat{y}}=\dfrac{Da\,Sh}{Da+\Delta}\hat{C}, \quad \hat{y}=\pm 1 \end{cases} \tag{2.44}$$

where non-dimensional groups are defined as

$$Re=\frac{u_m H}{\nu} \qquad \text{(Reynolds number)}$$
$$Sc=\frac{\nu}{D} \qquad \text{(Schmidt number)}$$
$$Pe=Re\,Sc=\frac{u_m H}{D} \qquad \text{(Péclet number)}$$
$$Da=\frac{\lambda H^2}{D} \qquad \text{(Damköhler number)}$$
$$Sh=\frac{\gamma H}{D} \qquad \text{(Sherwood number)}$$
$$\Delta=\frac{\delta H^2}{D} \qquad \text{(desorption number)}$$
$$f=\frac{H}{L} \qquad \text{(aspect ratio)}$$

Longitudinal diffusion is neglected to allow for separation of variables. This assumption is reasonable in all cases where diffusion is negligible compared to advection, i.e. if $Pe \gg f$. Since the order of the equation with respect to x is now reduced, a single (inlet) boundary condition for x is required. As a further simplification, full symmetry of the problem with respect the x-axis is assumed. The full problem now reads

$$\begin{cases} \dfrac{\partial^2\hat{C}}{\partial\hat{y}^2}-f\,Pe\,\hat{u}(\hat{y})\dfrac{\partial\hat{C}}{\partial\hat{x}}-Da\,\hat{C}+\hat{S}=0 \\ \hat{C}_d=\dfrac{Sh}{Da+\Delta}\hat{C}, \quad \hat{y}=\pm 1 \\ -\dfrac{\partial\hat{C}}{\partial\hat{y}}=\dfrac{Da\,Sh}{Da+\Delta}\hat{C}, \quad \hat{y}=1 \\ \dfrac{\partial\hat{C}}{\partial\hat{y}}=0, \quad \hat{y}=0 \\ \hat{C}=\hat{C}_{in}=\dfrac{C_{in}}{C_0}, \quad \hat{x}=0 \end{cases} \tag{2.45}$$

where C_{in} specifies a uniform inlet condition for $C(0,y)$.

For the following discussion, it is convenient to assume that the distributed source can be expressed as

$$S(x,y) = \bar{S}\tilde{S}(x,y) \tag{2.46}$$

where $\bar{S}$ is a representative value of the source, e.g. its average value over the domain. The choice of c_0 is purely a matter of convenience. A meaningful definition, however, is not trivial to find in the general case, given the interplay of several physical phenomena. In the simplest case with no internal source, concentration profiles become self-similar far from the inlet but no fully-developed solutions can be attained (in presence of removal mechanisms such as deposition and decay). In such case, the definition is straightforward:

$$C_0 = C_{in} \tag{2.47}$$

On the other hand, when a distributed source is present, the inlet contribution is forgotten as the fully-developed concentration profile is attained and therefore a more meaningful choice should be based on the relative intensity of generation and removal mechanisms. When radioactive decay is dominant, a good definition reads

$$C_0 = \frac{\bar{S}}{\lambda} \tag{2.48}$$

When decay is negligible, the reference concentration C_0 can be chosen as

$$C_0 = \begin{cases} \dfrac{H^2\bar{S}}{D}, & Sh \gg 1 \\ \dfrac{H\bar{S}}{\gamma}, & Sh \ll 1 \end{cases} \tag{2.49}$$

These values are useful to identify correct scaling with respect to the dominant removal mechanisms. Similar expressions are easily found when solving for the centerline concentration in fully-developed profiles with uniform source.

Solutions of the boundary value problem (2.45) can be found by separation of variables:

$$\hat{C}(\hat{x},\hat{y}) = \sum_{n=1}^{\infty} X_n(\hat{x}) Y_n(\hat{y}) \tag{2.50}$$

2.5.3 Derivation of the analytical solution

According to the above definition, the functions $Y_n(\hat{y})$ coincide with the eigenfunctions of the associated Sturm-Liouville problem found by isolating the $\hat{y}$ part of the equation. This can be highlighted by inserting (2.50) in (2.45) and after some manipulation:

$$\sum_{n=1}^{\infty} \left[f\,Pe\,Y_n \frac{\mathrm{d}X_n}{\mathrm{d}\hat{x}} - \frac{1}{\hat{u}(\hat{y})} \left(\frac{\mathrm{d}^2 Y_n}{\mathrm{d}\hat{y}^2} - Da Y_n \right) X_n \right] = \frac{\hat{S}(\hat{x},\hat{y})}{\hat{u}(\hat{y})} \tag{2.51}$$

The eigenvalue problem is therefore stated as

$$\mathcal{L}\,Y_n = \beta_n^2\,Y_n \tag{2.52}$$

where

$$\mathcal{L} = -\frac{1}{\hat{u}(\hat{y})}\left(\frac{\mathrm{d}^2}{\mathrm{d}\hat{y}^2} - Da\right) \tag{2.53}$$

and β_n^2 being the eigenvalue associated to the eigenfunction Y_n. The problem must be equipped with the corresponding boundary conditions:

$$\begin{cases} \dfrac{\mathrm{d}^2 Y_n}{\mathrm{d}\hat{y}^2} + \left(\beta_n^2 - Da - \beta_n^2\,\hat{y}^2\right) Y_n = 0 \\ -\dfrac{\mathrm{d}Y_n}{\mathrm{d}\hat{y}} = \dfrac{Da\,Sh}{Da + \Delta} Y_n, \quad \hat{y} = 1 \\ \dfrac{\mathrm{d}Y_n}{\mathrm{d}\hat{y}} = 0, \quad \hat{y} = 0 \end{cases} \tag{2.54}$$

It is easily verified that $\beta_n = 0$ is not an eigenvalue. Then, through the simple change of variable $\eta = \sqrt{2\beta_n}\hat{y}$, (2.54) can be recast into one form of the *parabolic cylinder equation* [18, Ch. 12]:

$$\frac{\mathrm{d}^2 Y_n}{\mathrm{d}\eta^2} - \left[\frac{\eta^2}{4} - \frac{\beta_n}{2}\left(1 - \frac{Da}{\beta_n^2}\right)\right] Y_n = 0 \tag{2.55}$$

whose general solution (back in terms of $\hat{y}$) can be expressed as

$$Y_n(\hat{y}) = A_{1,n} Y_{1,n}(\hat{y}) + A_{2,n} Y_{2,n}(\hat{y}) \tag{2.56}$$

where

$$Y_{1,n}(\hat{y}) = e^{-\beta_n \hat{y}^2/2} M\left(\frac{1-\beta_n}{4} + \frac{Da}{4\beta_n}, \frac{1}{2}; \beta_n\,\hat{y}^2\right) \tag{2.57}$$

$$Y_{2,n}(\hat{y}) = \sqrt{2\beta_n}\,\hat{y}\,e^{-\beta_n \hat{y}^2/2} M\left(\frac{3-\beta_n}{4} + \frac{Da}{4\beta_n}, \frac{3}{2}; \beta_n\,\hat{y}^2\right) \tag{2.58}$$

are two linearly independent solutions. $M(\cdot,\cdot;\cdot)$ is the *confluent hypergeometric function* of the first kind [18, Ch. 13], which can be expressed as the following power series expansion:

$$M(a,b;z) = 1 + \frac{a}{b}z + \frac{a(a+1)}{b(b+1)}\frac{z^2}{2!} + \cdots = \sum_{k=0}^{\infty} \frac{(a)_k}{(b)_k}\frac{z^k}{k!} \tag{2.59}$$

where

$$(a)_k = a(a+1)\cdots(a+k-1) = \prod_{s=1}^{k}(a+s-1) \tag{2.60}$$

denotes the so-called *Pochhammer symbol*, or *rising factorial.* The eigenvalue problem must be solved by imposing the associated boundary conditions. By means of the following properties of $M(a,b;z)$,

$$M(a,b;0) = 1 \tag{2.61}$$

$$\frac{\mathrm{d}}{\mathrm{d}z} M(a,b;z) = \frac{a}{b} M(a+1,b+1;z), \tag{2.62}$$

it can be easily shown that the symmetry condition at $\hat{y} = 0$ implies $A_{2,n} = 0$. The wall boundary condition requires

$$\frac{Da\,Sh}{Da + \Delta} Y_{1,n}(1) + Y'_{1,n}(1) = 0 \tag{2.63}$$

which gives the β_n values that correspond to the non-trivial solutions of the eigenvalue problem. Solutions of (2.63) have to be found numerically; more detailed numerical considerations can be found in Appendix A.1. The eigenfunctions are therefore determined (up to an arbitrary multiplicative constant) as

$$Y_n(\hat{y}) = Y_{1,n}(\hat{y}) \tag{2.64}$$

The separated equation (2.51) now reads

$$\sum_{n=1}^{\infty} \left(\frac{\mathrm{d}X_n}{\mathrm{d}\hat{x}} + \frac{\beta_n^2}{f\,Pe} X_n \right) Y_n = \frac{1}{f\,Pe} \frac{\hat{S}(\hat{x},\hat{y})}{\hat{u}(\hat{y})} \tag{2.65}$$

The eigenfunctions Y_n are orthogonal with respect to the scalar product defined as

$$\langle f, g \rangle = \int_{-1}^{+1} \hat{u}(\hat{y}) f g \mathrm{d}\hat{y} \tag{2.66}$$

with

$$\langle Y_m, Y_n \rangle = \int_{-1}^{+1} \hat{u}(\hat{y}) Y_m Y_n \,\mathrm{d}\hat{y} = C_n \delta_{m,n} \tag{2.67}$$

$$C_n = \langle Y_n, Y_n \rangle = \int_{-1}^{+1} \hat{u}(\hat{y}) Y_n^2 \,\mathrm{d}\hat{y} \tag{2.68}$$

This is exploited to transform (2.65) into

$$\frac{\mathrm{d}X_n}{\mathrm{d}\hat{x}} + \frac{\beta_n^2}{f\,Pe} X_n = \frac{1}{f\,Pe} S_n(\hat{x}) \tag{2.69}$$

whose general solution is

$$X_n(\hat{x}) = \exp(-\frac{\beta_n^2}{f\,Pe}\hat{x}) \left[X_n(0) + \frac{1}{f\,Pe} \int_0^{\hat{x}} \exp(\frac{\beta_n^2}{f\,Pe}\xi) S_n(\xi) \mathrm{d}\xi \right] \tag{2.70}$$

To obtain this last form, $\hat{S}$ has been expanded as

$$\hat{S}(\hat{x},\hat{y}) = \hat{u}(\hat{y}) \sum_{n=1}^{\infty} S_n(\hat{x}) Y_n \tag{2.71}$$

$$S_n(\hat{x}) = \frac{1}{C_n} \int_{-1}^{+1} \hat{S}(\hat{x},\hat{y}) Y_n \,\mathrm{d}\hat{y} \tag{2.72}$$

Table 2.1: Values of Da e Sh selected for verification cases.

Case n°	1	2	3	4	5	6	7	8	9
Da	0.1	0.1	0.1	1.0	1.0	1.0	10	10	10
Sh	0.1	1.0	10	0.1	1.0	10	0.1	1.0	10

and the arbitrary constants $X_n(0)$ have been determined from the remaining inlet boundary condition (expanded as well):

$$X_n(0) = \frac{1}{C_n}\int_{-1}^{+1} \hat{u}(\hat{y})\hat{c}_{in}Y_n \,\mathrm{d}\hat{y} = \frac{D_n}{C_n}\hat{c}_{in} \tag{2.73}$$

where

$$D_n = \langle 1, Y_n\rangle = \int_{-1}^{+1} \hat{u}(\hat{y})Y_n \,\mathrm{d}\hat{y} \tag{2.74}$$

The normalisation constants C_n and D_n can be found by numerical integration of (2.68) and (2.74), respectively. More details on their computation are reported in Appendix A.1.

2.5.4 Results

Results of the verification of the implemented models against the analytical solutions are here presented. In Section 2.5.3 it is shown that, if the effect of desorption is negligible compared to decay, the β_n are the roots of

$$Sh\, Y_n(1) + Y_n'(1) \tag{2.75}$$

with

$$Y_n(\hat{y}) = e^{-\beta_n \hat{y}^2/2} M\left(\frac{1-\beta_n}{4} + \frac{Da}{4\beta_n}, \frac{1}{2}; \beta_n\, \hat{y}^2\right) \tag{2.76}$$

It is therefore evident that the inclusion of a linear decay term in the transport equation affects the concentration profiles shape by shifting the eigenvalues. As shown in Figures 2.5 to 2.8, the influence of the decay parameter Da is significant. For dominant modes, the increase of Da tends to flatten the β_n curves, resulting in a vanishing influence of Sh in determining the shape of the concentration field. On the contrary, higher-order modes are less affected, with the eigenvalue shift due to linear decay decreasing as n increases.

In the following, results from the comparison between the OpenFOAM model described in Section 2.4 and the corresponding analytical solutions are discussed. To highlight the role of decay and deposition phenomena, the selected parameters are Da and Sh, with values ranging in [0.1,1,10] for both. Case study parameter values are listed in Table 2.1, while other relevant parameters of the problem are listed in Table 2.2.

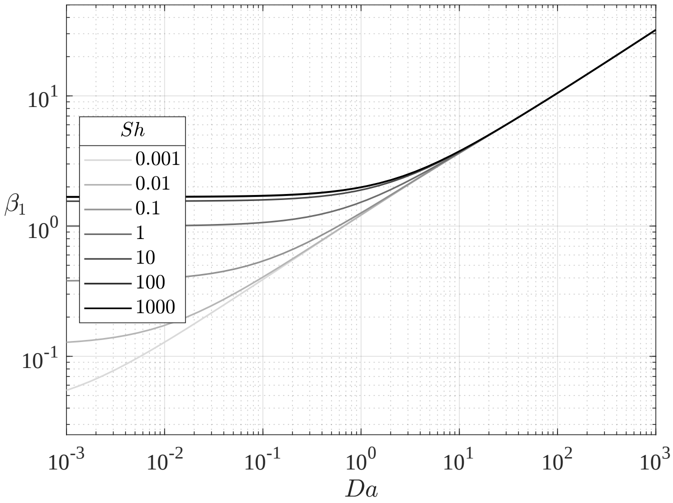

Figure 2.5: Dependence of the 1st eigenvalue β_1 on model parameters Sh and Da.

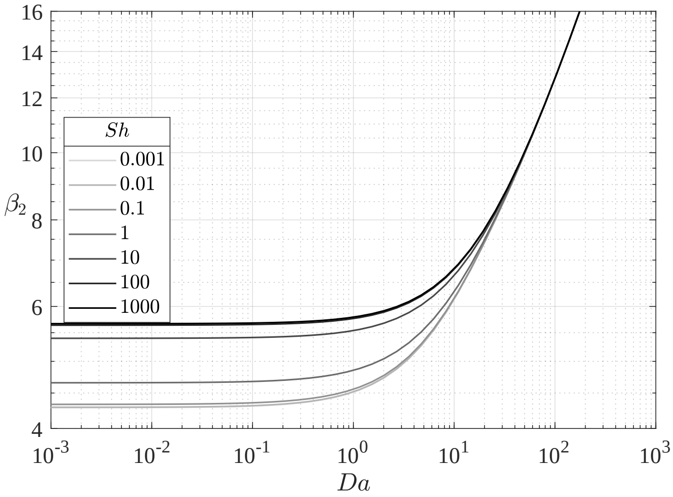

Figure 2.6: Dependence of the 2nd eigenvalue β_5 on model parameters Sh and Da.

Table 2.2: Model parameters used in all verification cases.

Re	Sc	Pe	Δ	f
500	1	500	0	0.025

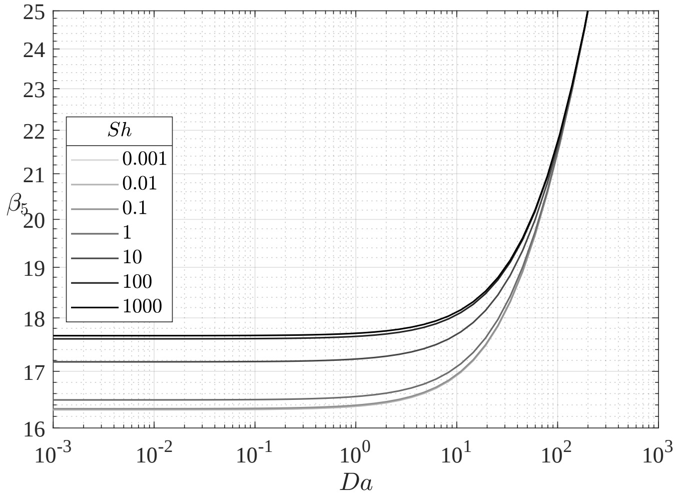

Figure 2.7: Dependence of the 5th eigenvalue β_5 on model parameters Sh and Da.

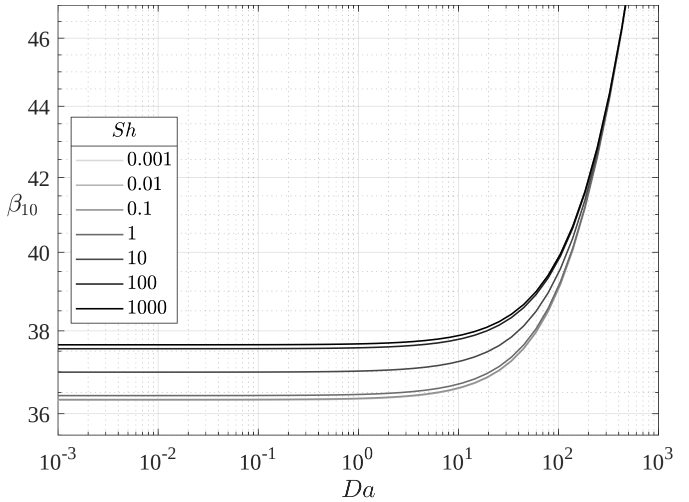

Figure 2.8: Dependence of the 10th eigenvalue β_{10} on model parameters Sh and Da.

Table 2.3: Computational times for the verification cases. 5×10^4 iterations are performed on 5×10^4 volumes with 8 CPUs.

Case n°	1	2	3	4	5	6	7	8	9
time (s)	2037	2684	2102	2312	2003	2636	2000	2036	2119

To simplify the analysis, the inlet concentration is set to zero ($c_{in} = 0$). Furthermore, to allow for a direct comparison between different test cases, the reference concentration value has been selected as

$$C_0 = \frac{H^2\bar{S}}{D} \tag{2.77}$$

It follows that

$$\hat{S}(\hat{x},\hat{y}) = \frac{S(L\hat{x},H\hat{y})}{\bar{S}} = \tilde{S}(L\hat{x},H\hat{y}) \tag{2.78}$$

Therefore in dimensionless form the solution does not depend on the source term average value, but only on its shape. For the present analysis, a cosine-shaped source term has been selected to resemble the typical shape of fission rate profiles in simplified reactor geometries such as the one here considered:

$$\tilde{S}(L\hat{x},H\hat{y}) = \frac{\pi}{2}\cos(\frac{\pi}{2}\hat{y}) \tag{2.79}$$

Concentration profiles obtained for the 9 test cases (Table 2.1) are shown in Figures 2.9 to 2.11.

Results show excellent agreement between the proposed transport model and the analytical solutions, proving a successful verification of the the implemented transport models in OpenFOAM. The influence of decay is evidenced from the decrease in concentration profiles from $Da = 0.1$ to $Da = 10$. Besides the average value, the effect of decay is also evident on the shape itself as also pointed out by the analysis of the eigenvalues. With increasing Da, particles can diffuse less before decaying, and therefore the concentration profiles tend to resemble more the shape of the source term. The same effect can be seen on the combined effect of deposition: as previously said, the effect of Sh on the profiles is more evident for smaller values of Da, while profiles tend to become more similar as Da increases.

Finally, in the following some information regarding computational costs is reported. All simulations were performed on a structured orthogonal mesh, constituted by 5×10^4 hexahedral volumes, with respectively 500 and 100 divisions on the longitudinal and transversal directions. All 9 cases shown similar convergence behaviour, with approximately 5×10^4 pseudo-transient iterations needed to ensure tight convergence for the particle concentration field. Computational times are comparable among all cases, showing no significant dependence on the physical parameters within the selected range (Table 2.3).

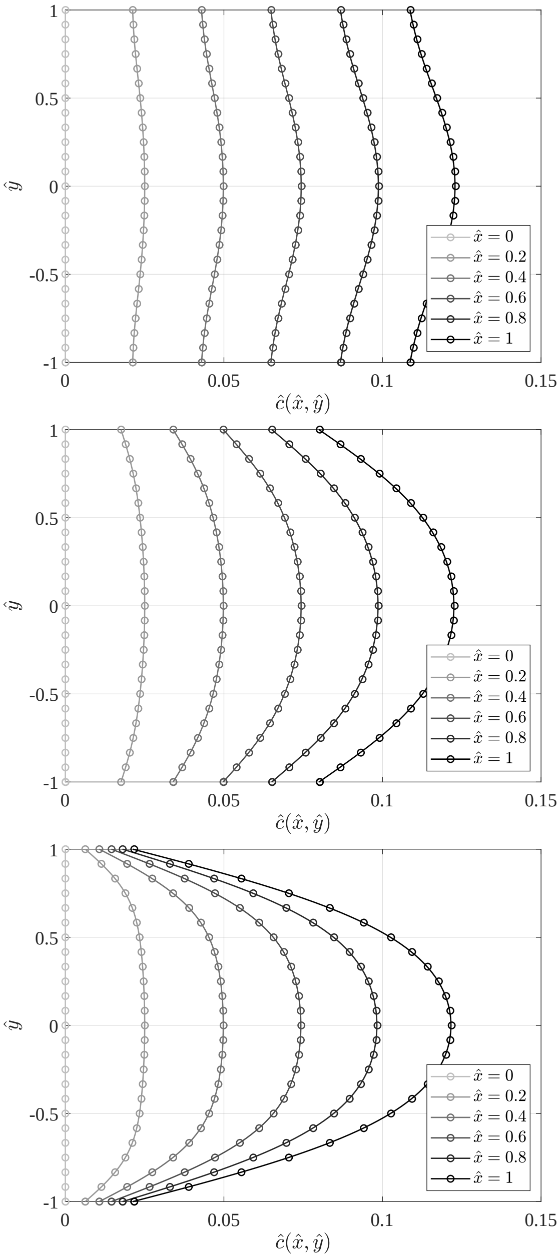

Figure 2.9: Comparison of concentration profiles obtained with the proposed transport model implemented in OpenFOAM ($\circ$) and the corresponding analytical solutions ($-$) for cases 1, 2 and 3 (from top to bottom).

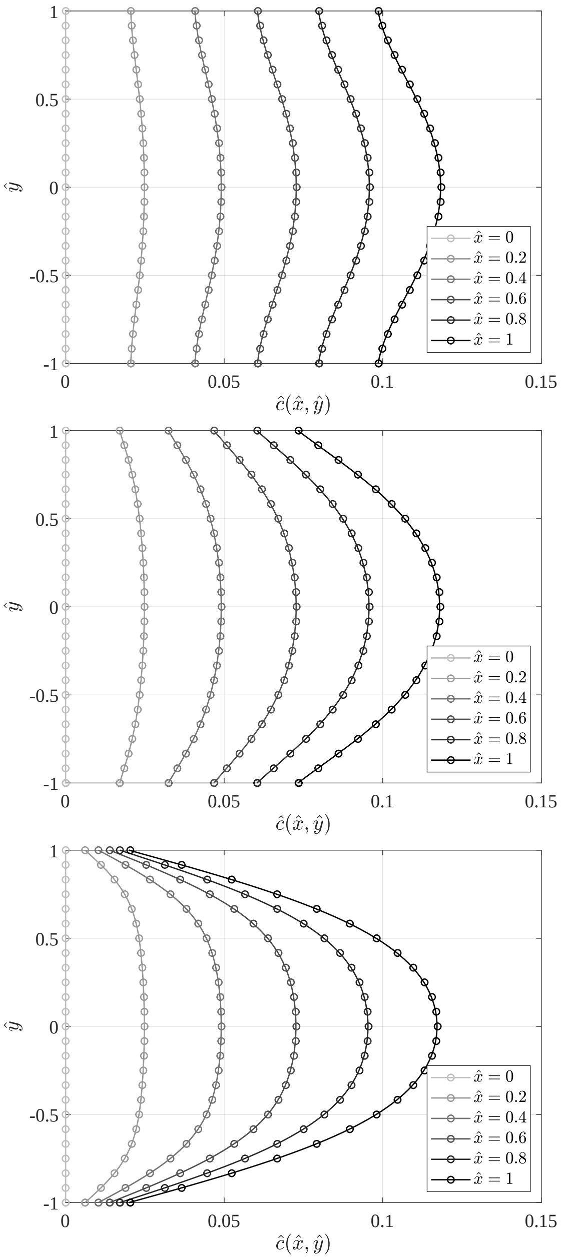

Figure 2.10: Comparison of concentration profiles obtained with the proposed transport model implemented in OpenFOAM (○) and the corresponding analytical solutions (−) for cases 4, 5 and 6 (from top to bottom).

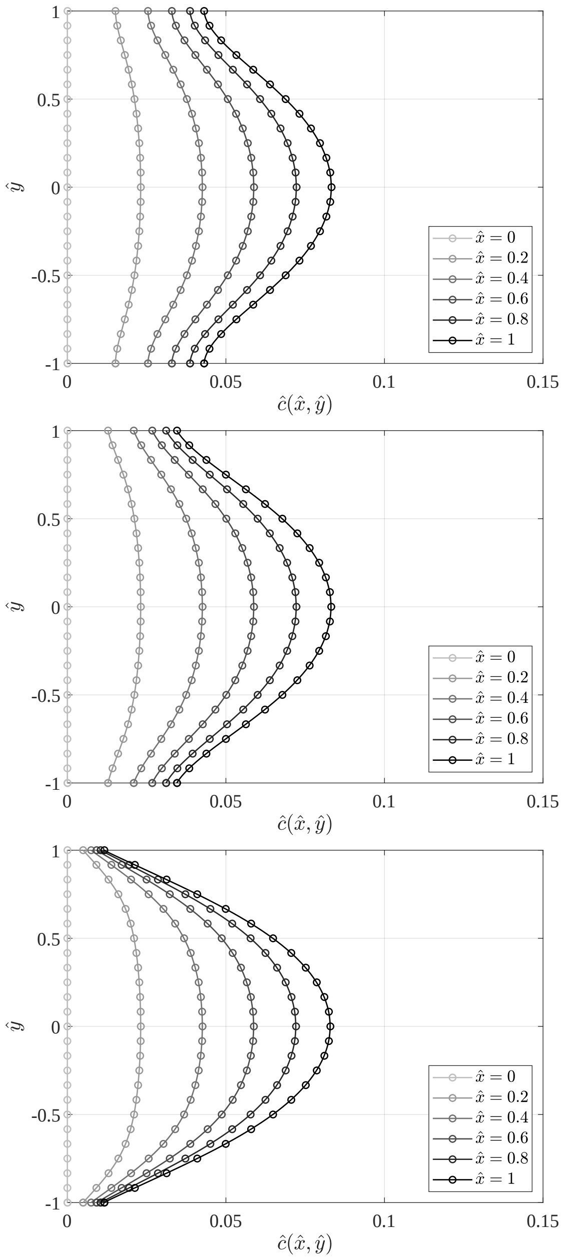

Figure 2.11: Comparison of concentration profiles obtained with the proposed transport model implemented in OpenFOAM (∘) and the corresponding analytical solutions (−) for cases 7, 8 and 9 (from top to bottom).

Chapter 3

Fission Products Transport in the MSFR

The results presented in this Chapter have been published in:

Di Ronco, A., et al. "Multiphysics Analysis of RANS-Based Turbulent Transport of Solid Fission Products in the Molten Salt Fast Reactor". *Nuclear Engineering and Design*, vol. 391, 2022, https://doi.org/10.1016/j.nucengdes.2022.111739.

In this Chapter, the developed multiphysics solver described in Chapter 2 is tested on different multiphysics cases. In the first one, described in Section 3.1, a geometry is selected based on the well-known lid-driven square laminar cavity. Even though still fairly simplified, the case features full coupling between thermal hydraulics and neutronics. Geometry and parameters were chosen for an international benchmark for MSR codes [49], and this work may represent an extension of the MSFR benchmark towards solid FP simulation. In the second one, described in Section 3.2, the 2D MSFR geometry developed in the EVOL project is used. It features the loop structure typical of the MSFR with fuel recirculation, allowing for the simulation of more realistic turbulent cases. Both cases are selected for their simplified geometric features, which enable the production of high-quality numerical grids even when wall refinement is crucial for the resolution of particle transport in the wall regions, as seen in Section 2.4.2. Furthermore, the adoption of 2D cases allows for a significant reduction of computational requirements with respect to full 3D simulations. In the third and last one, described in Section 3.3, the cavity case is used again for a preliminary test of the influence of precipitation modelling on the distribution of FPs.

The physical properties needed for the simulation of FP particles are kept the same for each case to provide comparable results. The decay constant λ_C has been set to $10^{-5}\,\mathrm{s}^{-1}$, which corresponds to a nuclide half-life of approximately one day. The equivalent fission yield y_C has been set to 10^{-2}. Such values are not specific to a particular nuclide, but have been chosen to mimic the behaviour of the entire class of noble metal particles.

3.1 The CNRS benchmark cavity

This lid-driven cavity was recently employed to develop a reference case for a numerical benchmark of different multiphysics MSFR codes. A detailed description of the case and of the benchmark procedure can be found in [49]. The domain is characterised by a 2 m by 2 m cavity filled with molten salt (Figure 3.1). The domain is treated as a homogeneous, bare reactor. Therefore, standard vacuum conditions are applied for the neutron flux to each boundary, together with a (reflective) homogeneous Neumann condition for the delayed neutron precursors. Decay heat precursors are not simulated in this case, for better consistence with [49]. The driving force for the liquid fuel flow is given by the upper lid, which moves at constant velocity of $0.5\,\mathrm{m\,s^{-1}}$. All walls are treated as adiabatic, while energy is removed from the system through a simple volumetric heat sink:

$$q_r''' = -\frac{\gamma_r}{V_r}(T - T_{sink}) \tag{3.1}$$

where γ_r is a total heat removal coefficient and V_r is the volume of heat removal region, which in this case coincides with the entire cavity domain. The main physical case parameters are summarised in Table 3.1, while the neutronics data are reported in Appendix B. Being the analysis conducted in steady-state conditions, simulations are performed in criticality eigenvalue mode with the integrated power normalised to 1000 MW.

With respect to the classic lid-driven case, the coupling with the distributed energy source through buoyancy significantly affects the flow pattern, producing more complex recirculation structures and making this test case suitable for study with multiphysics solvers, despite its overall simplicity.

The computational mesh is produced by specifying a small set of parameters: the number of divisions (equal in both directions), the thickness of the cells in the first boundary layer and the number of cells to be progressively refined. To correctly resolve the concentration boundary layers, a thickness of $10^{-4}\,\mathrm{m}$ has been chosen according to results of the analytical analysis conducted in Section 2.4.2. The resolution of the boundary layer is particularly relevant for the correct prediction of the deposition rates. The prescribed refinement is found to adequately cover the boundary layer with several cell layers. The number of refined cells has been set to 40. For what concerns the number of divisions, three different values have been considered: 100, 200 and 400. Considering the two directions separately, the meshing routine computes a constant cell growth-rate which produces a smooth transition between the refined region and the rest of the domain (where the growth-rate is set to 1). Figure 3.1 shows the mesh for the coarsest case (100 divisions).

3.1.1 Results and discussion

Steady-state simulations have been performed with the three different mesh refinements described earlier. These preliminary laminar simulations have been conducted to study the effects of grid refinement, since an adequate refinement is crucial for the prediction

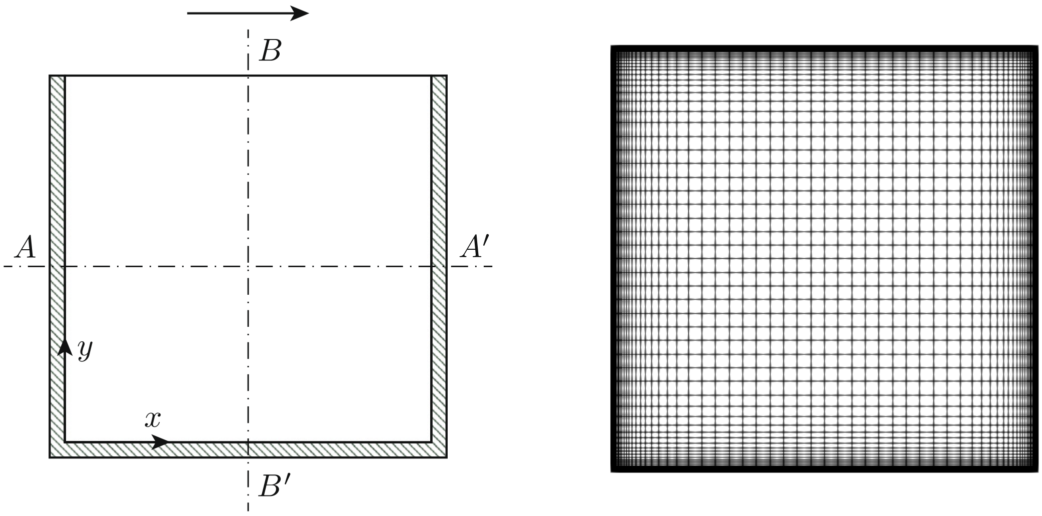

Figure 3.1: Lid-driven cavity: geometry (from [49], left) and computational mesh (coarsest case, right). The grid is refined by means of a constant growth-rate in the first 40 layers of cells, starting from a prescribed smallest layer size

Table 3.1: Main physical parameter values adopted for the lid-driven cavity case [49].

Parameter	Symbol	Units	Value
Density	ρ	$\mathrm{kg\,m^{-3}}$	2000
Kinematic viscosity	ν	$\mathrm{m^2\,s^{-1}}$	2.50×10^{-2}
Specific heat capacity	c_p	$\mathrm{J\,kg^{-1}\,K^{-1}}$	3.075×10^{3}
Thermal expansion coeff.	β_T	$\mathrm{K^{-1}}$	2.00×10^{-4}
Ref. temperature	T_0	K	900
Prandtl number	Pr	–	3.075×10^{5}
Schmidt number	Sc	–	2.0×10^{8}
Heat removal coeff.	γ_r	$\mathrm{W\,K^{-1}}$	4.0×10^{6}
Heat sink temperature	T_{sink}	K	900

of deposition rates. For reference, velocity and temperature distributions are shown in Figure 3.2. As anticipated, the interplay between the upper lid motion and the buoyancy effects produces complex recirculation patterns with two separate large laminar eddies, in contrast with the classical isothermal lid-driven cavity problem.

Concentration results for the different mesh refinements are reproduced in Figure 3.3 and in Figure 3.4 for what concerns distributions in the domain and profiles in the wall layers close to left and right walls, respectively. While the wall refinement guarantees a proper resolution of the wall layers in all cases, showing a suitable number of grid points even in the coarsest case thanks to the specific meshing procedure adopted which specifies the thickness of the first layer, only the most refined grid is able to capture all transport patterns in the domain. One possible cause is due to the use of gradient-limited upwind-biased 2nd-order divergence schemes. While 2nd-order schemes are often needed to ensure proper accuracy, their use with low-quality meshes and/or complex flows might produce unbounded or unstable results [52]. On the other hand, the nature of the problem forces the use of upwind-biased schemes to provide a good balance between stability and accuracy; gradient limiting is also needed to ensure boundedness in the presence of steep gradients such as the ones which occur in the wall layers. Other transported quantities, such as neutron precursors, do not need this kind of numerical treatment due to the different reflective boundary conditions adopted.

Wall concentration profiles are characterised by different "asymptotic values" depending on the grid refinement and the overall accuracy dictated by the quality of the mesh. Nevertheless, within the wall layer, concentration profiles exhibit similar behaviour, somewhat confirming some of the results given by the analytical treatment of Section 2.4.2. Using the values specified for λ_C, ν and Sc, Equation (2.34) predicts a value for Δy^* of about 0.0035 m. Even though the mesh refinement has been selected to ensure fairly thinner boundary elements, such value is not found to be sufficiently representative of the results from Figure 3.4. Computed profiles show significantly thinner wall layers, suggesting a strong influence of local velocity patterns and transport mechanism with respect to the simplified approach adopted in the analytical model. This is particularly evident from the comparison between the left and right walls, where the right wall layer is approximately 3-4 times larger than the left one. Nevertheless, the analytical treatment proves a useful tool to predict estimates and to understand the role of the main physical parameters.

3.2 The two-dimensional EVOL MSFR

A simplified 2D axisymmetric geometry is adopted following the work of the past EVOL project [9]. Solid parts in the system are neglected as well. The full geometry is shown in Figure 3.5, together with some information regarding the position of the heat exchanger and pump sections. The heat exchanger is modelled similarly as in the cavity case, through the use of a linear sink term analogous to Equation (3.1). The heat removal coefficient γ_r is here assumed to be zero outside the heat exchanger region. For what concerns the pump, a momentum source is imposed, along the vertical direction, which

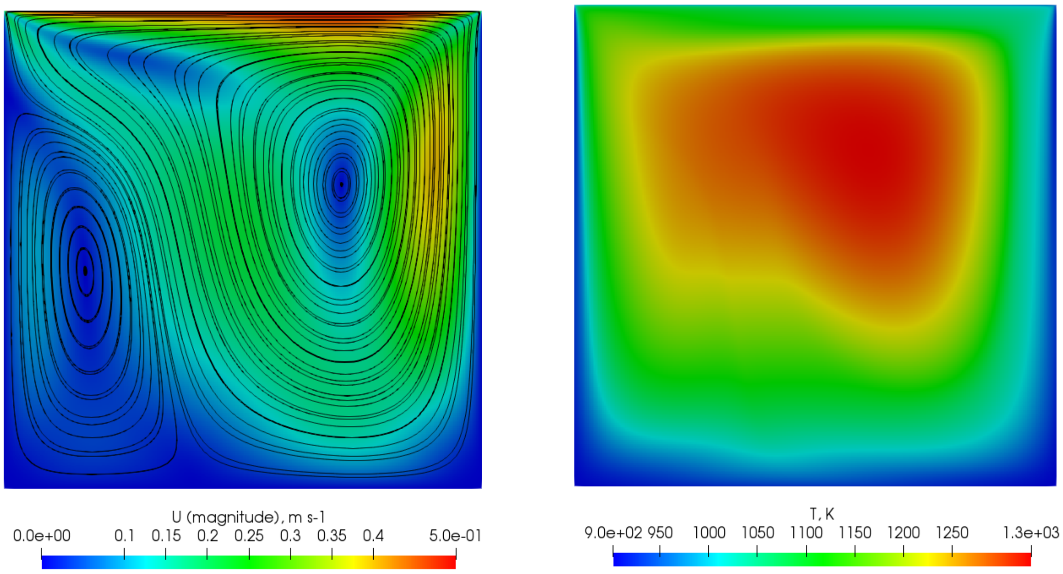

Figure 3.2: Velocity U (left) and temperature T (right) distributions in the lid-driven cavity (most refined mesh, 400 divisions). Velocity streamlines are also added for more clarity. The combined action of lid motion and buoyancy affects the flow pattern, producing two separate recirculation zones.

matches the flow rate at the pump outlet section to the total one ($1.9 \times 10^4\,\mathrm{kg\,s^{-1}}$, for the entire reactor). The main physical case parameters are summarised in Table 3.2, while the neutronics data are reported in Appendix B.

The simplified geometry allows for the production of good-quality structured meshes with little effort. In this case, a cell size of 0.01 m is employed across all the domain for the generation of the underlying mesh (Figure 3.5). Then, subsequent cell divisions are applied to the first boundary layer of cells to provide a suitable mesh refinement in the wall region. Boundary layer cells are roughly halved 6 times, to produce a first layer with a thickness of approximately 10^{-4} m. The total number of mesh elements is around 4.2×10^4.

Three different steady-state cases are simulated to assess the effect of turbulence modelling on the transport of FP particles. As described in Chapter 2, the solver makes use of the standard linear eddy viscosity approach for the modelling of turbulent quantities. The eddy viscosity ν_t affects the transport problem in a direct way, through the definition of the total mass transfer coefficient D_{eff}, and through the computation of the velocity field. For this reason, three different turbulence models are used: standard k-ε [31], the standard k-ω [54] and the k-ω-SST [36]. Gradient-based turbulent diffusion constitutes a standard approach in CFD and multiphysics analysis, but relies heavily on the turbulent Schmidt number Sc_t, with optimal values depending on fluid properties and on flow configuration [50]. Given the lack of experimental data for MSFR appli-

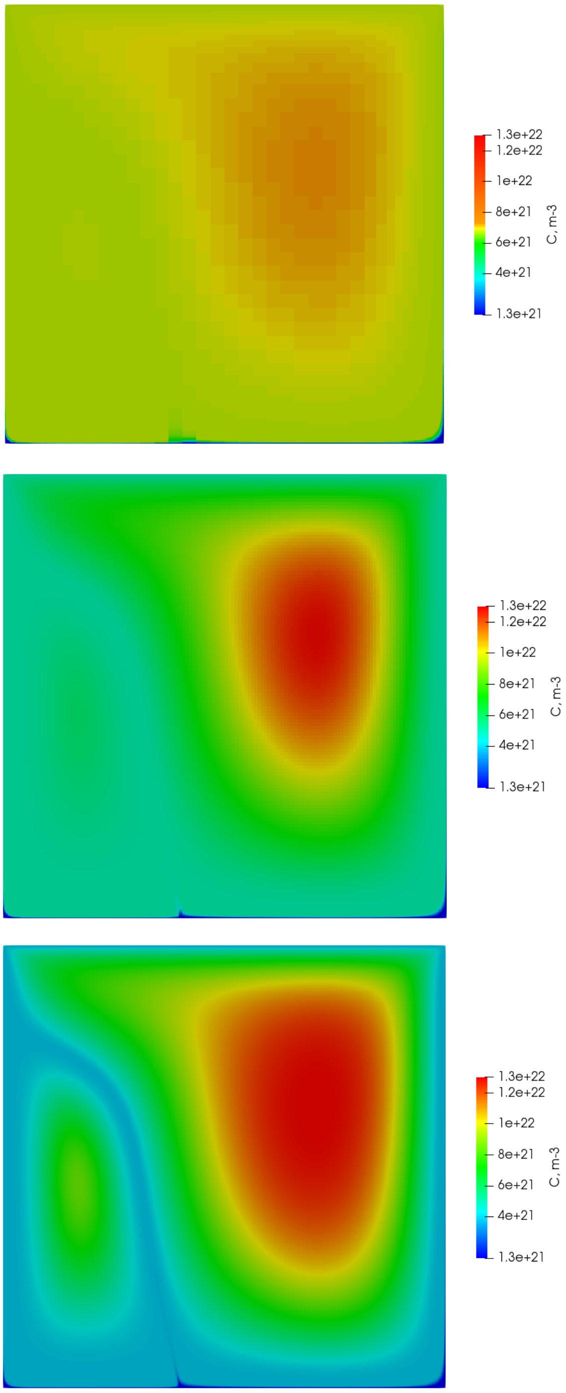

Figure 3.3: Particle concentration C distributions for three different mesh refinements: from top to bottom, 100, 200, and 400 divisions in both directions.

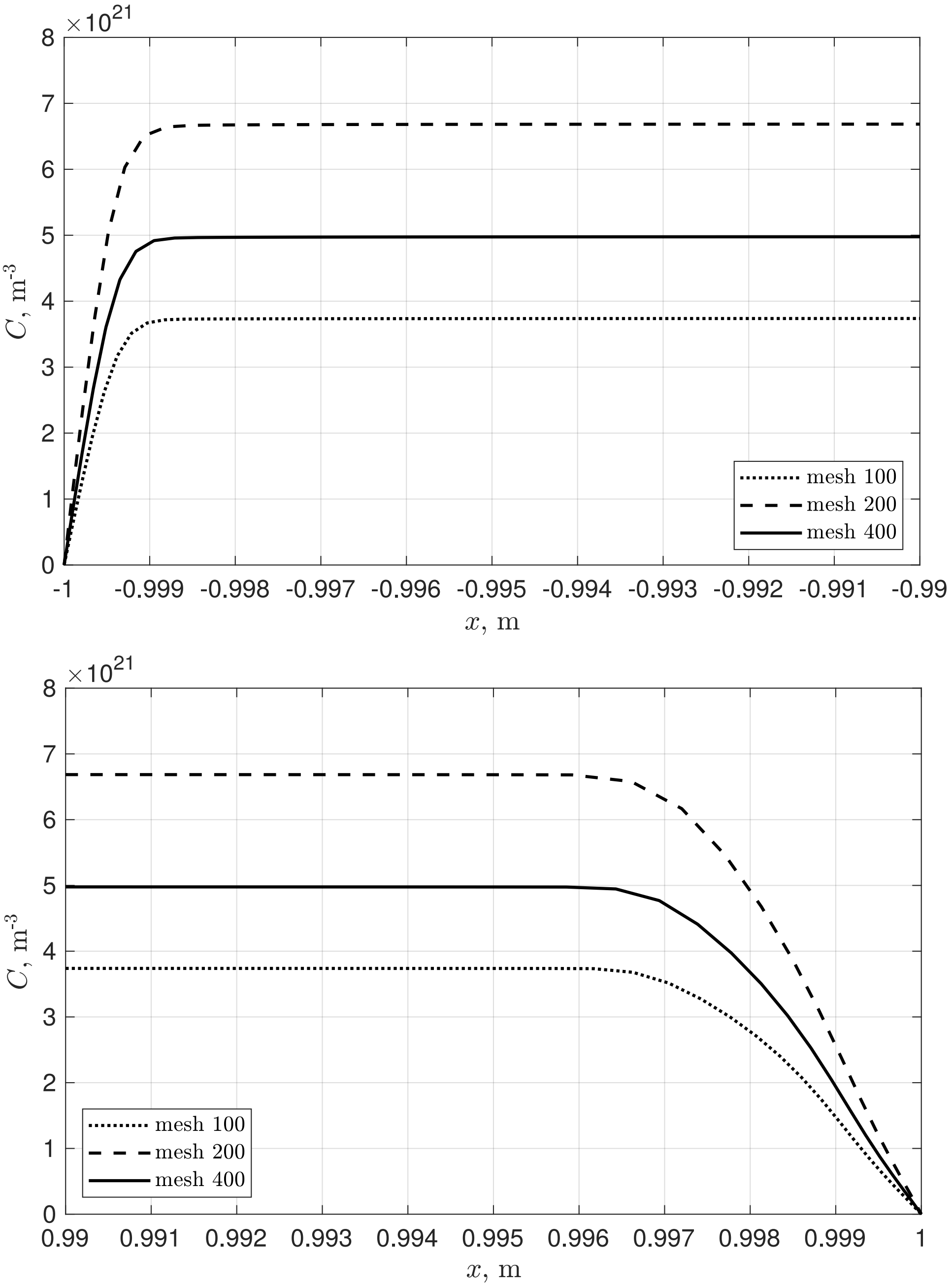

Figure 3.4: Particle concentration C wall profiles for three different mesh refinements. Line plots correspond to a horizontal line at half the cavity height on the left (top plot) and right (bottom plot) walls, corresponding to points A and A' of Figure 3.1.

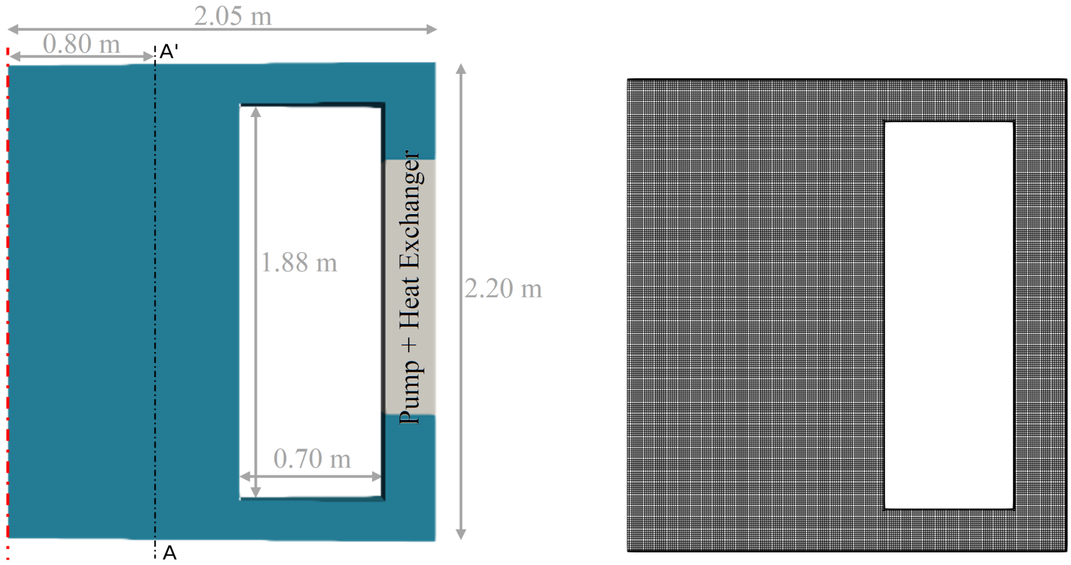

Figure 3.5: EVOL case: an axisymmetric geometry (left) is chosen to reduce the computational requirements and the resulting mesh (right) is predominantly structured thanks to the simple geometry employed. Wall mesh refinement is obtained by subsequent divisions of the wall layer.

cations, in this work three different values (0.50, 0.85 and 1.20) are selected to provide insight on the influence of such parameter on simulations over a relatively broad range of variation.

3.2.1 Results and discussion

Steady-state simulations have been conducted with the selected turbulence models and values for Sc_t for a total of nine cases, as described earlier. As in the cavity cases, 2nd-order upwind-biased gradient-limited convergence schemes have been used for the simulation of FPs. For reference, velocity and total kinetic viscosity distributions are shown in Figure 3.6. As expected, the choice of turbulence model has an evident impact on the prediction of U and ν_{eff}, in particular when comparing turbulence models from the $k-\varepsilon$ and $k-\omega$ families. Such differences have a direct influence on the combined effect of advective and diffusive transport mechanisms for FPs, as better evidenced by Figure 3.7, which shows the volume distributions of the particle concentration C for the three simulated cases. Maximum and average particle concentrations are approximately one order of magnitude lower in the $k-\varepsilon$ case than in the other cases, qualitatively in accordance with the higher $k-\varepsilon$ diffusivity.

The same behaviour is observed, naturally, in the concentration profiles close to walls. Figure 3.8 shows concentration profiles close to the bottom and top walls, in correspondence of a vertical line placed at 0.8 m from the reactor symmetry axis (Figure 3.5).

Table 3.2: Main physical parameter values adopted for the EVOL case.

Parameter	Symbol	Units	Value
Density	ρ	$\mathrm{kg\,m^{-3}}$	4.307×10^3
Kinematic viscosity	ν	$\mathrm{m^2\,s^{-1}}$	5.89×10^{-6}
Specific heat capacity	c_p	$\mathrm{J\,kg^{-1}\,K^{-1}}$	1.594×10^3
Thermal expansion coeff.	β_T	$\mathrm{K^{-1}}$	1.912×10^{-4}
Ref. temperature	T_0	K	973
Prandtl number	Pr	–	23.78
Turb. Prandtl number	Pr_t	–	0.85
Schmidt number	Sc	–	20.0
Turb. Schmidt number	Sc_t	–	0.50/0.85/1.20
Heat removal coeff.	γ_r	$\mathrm{W\,m^{-2}\,K^{-1}}$	2.5×10^6
Heat sink temperature	T_{sink}	K	900

Also in this case, gradient limiting allows for the computation of steep wall gradients without the insurgence of instability issues, while the prescribed mesh refinement proves adequate to resolve correctly the gradients. Once again, the thickness of the wall layers shows values of the order of 10^{-3} m, which clearly demonstrates the importance of local velocity profiles and of turbulence in determining the steepness of the concentration gradients and thus the required grid refinement in the wall regions. It appears evident that also the choice of turbulence model itself affects to some degree the thickness of the wall layers. Nevertheless, also in this case the thickness values predicted by the analytical model have proven useful, at least as preliminary estimates.

The integrated deposited fraction, together with other integral information are reported in Table 3.3. It appears from the results that, besides the differences in the total number of precipitate particles between the three cases, the choice of the turbulence model has a very limited influence on the number of deposited particles. This is a direct consequence of the similar gradients computed by the three models. Furthermore, in the diffusive wall layers the eddy diffusivity tends to zero and therefore the total value tends to the laminar one ($\nu/Sc = 2.945 \times 10^{-7}\,\mathrm{m^2\,s^{-1}}$), which is the same for the three cases.

The choice of the turbulent Schmidt number appears to play a similar role: larger values lead to lower diffusivities and increased precipitate concentrations, but deposition rates are scarcely affected. This confirms the prevalence of laminar diffusion in transport mechanisms close to walls, as shown by the similar wall concentration profiles shown in Figure 3.8, and allows for a certain flexibility in the choice of Sc_t as far as deposition figures are concerned. Lastly, the transport mechanisms towards the walls appear efficient when compared to the intensity of radioactive decay (in our cases, $\lambda_C = 10^{-5}\,\mathrm{s^{-1}}$), since more than 99.9% of particles end up depositing on walls. This effect is expected to be even more significant for longer-lived metallic FPs.

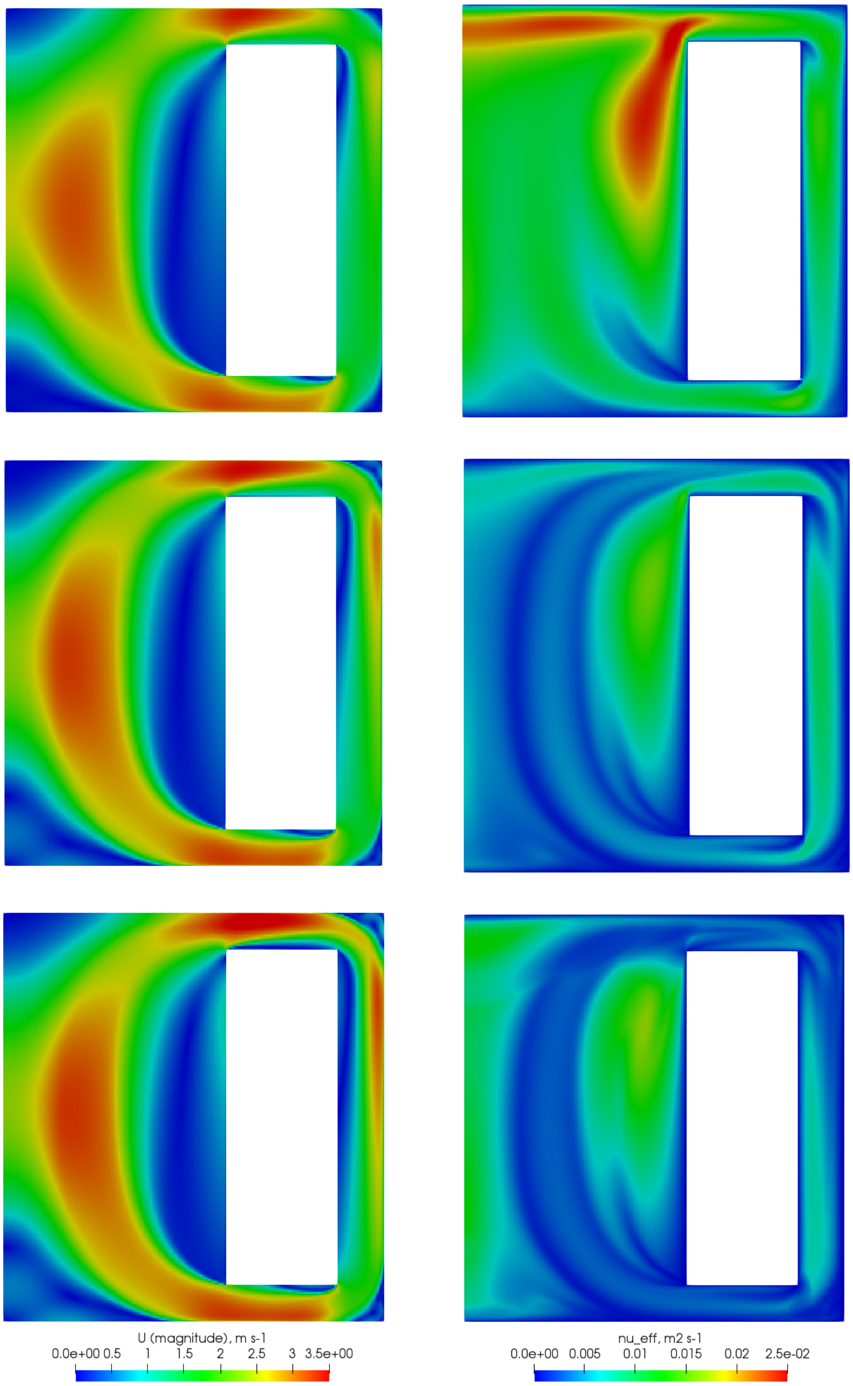

Figure 3.6: Magnitude of velocity $\mathbf{u}$ (left) and total kinetic viscosity ν_{eff} (right) distributions in the EVOL reactor for the $k-\varepsilon$, $k-\omega$ and $k-\omega-SST$ turbulence models (from top to bottom).

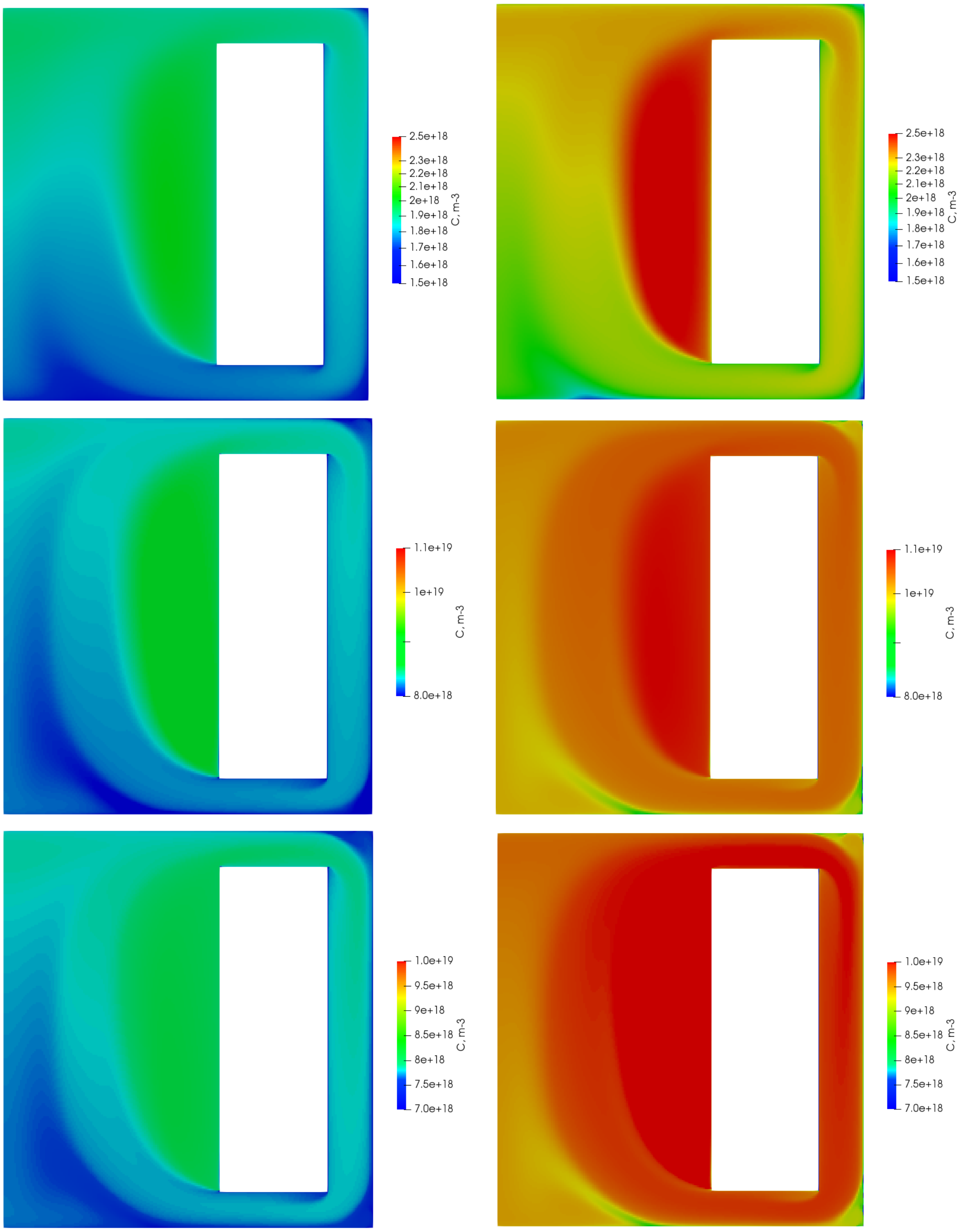

Figure 3.7: Particle concentration C distributions for the $k-\varepsilon$, $k-\omega$ and $k-\omega-SST$ turbulence models (from top to bottom). Plots on the left and right columns refer to Sc_t equal to 0.50 and 1.20, respectively.

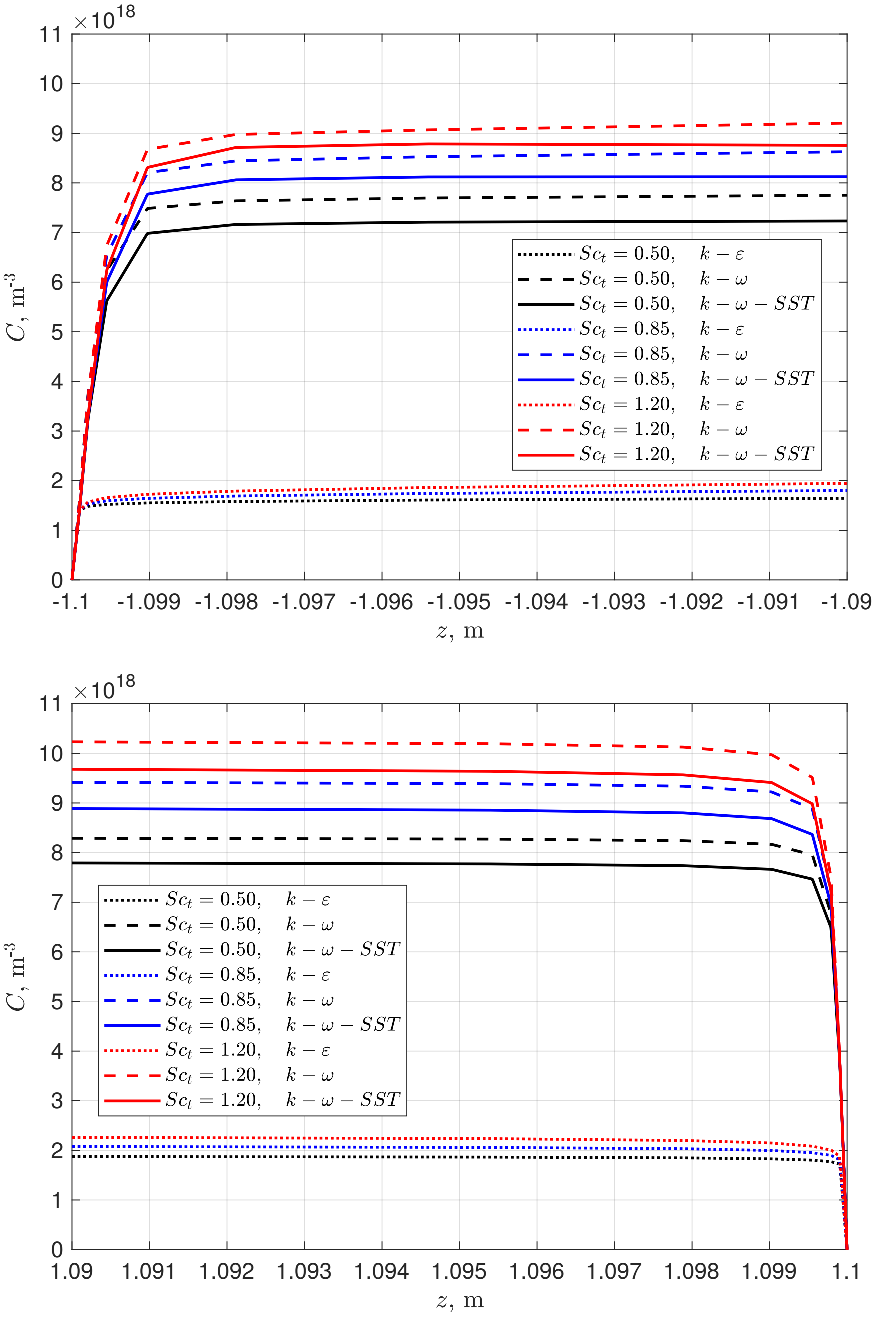

Figure 3.8: Particle concentration C wall profiles for different values of the turbulent Schmidt number Sc_t and turbulence models. Line plots refer to vertical lines of length 0.01 m placed at 0.8 m from the reactor symmetry axis on the bottom (top plot) and top (bottom plot) walls (A-A' in Figure 3.5).

Table 3.3: EVOL case: main simulation results for the selected turbulence models and values of Sc_t. The balance error is computed as the relative difference between the integral source and the sum of the integral deposition and decay rates.

(a) $Sc_t = 0.50$

Quantity	Units	$k-\varepsilon$	$k-\omega$	$k-\omega-SST$
Tot. precipitate	–	4.852×10^{17}	2.177×10^{18}	2.049×10^{18}
Tot. deposit	–	1.263×10^{21}	1.261×10^{21}	1.261×10^{21}
Tot. source	s^{-1}	1.263×10^{16}	1.263×10^{16}	1.263×10^{16}
Tot. dep. rate	s^{-1}	1.263×10^{16}	1.261×10^{16}	1.261×10^{16}
Tot. decay rate	s^{-1}	4.852×10^{12}	2.177×10^{13}	2.049×10^{13}
Rel. balance err.	–	1.524×10^{-6}	1.544×10^{-6}	1.546×10^{-6}

(b) $Sc_t = 0.85$

Quantity	Units	$k-\varepsilon$	$k-\omega$	$k-\omega-SST$
Tot. precipitate	–	5.441×10^{17}	2.495×10^{18}	2.362×10^{18}
Tot. deposit	–	1.263×10^{21}	1.261×10^{21}	1.261×10^{21}
Tot. source	s^{-1}	1.263×10^{16}	1.263×10^{16}	1.263×10^{16}
Tot. dep. rate	s^{-1}	1.263×10^{16}	1.261×10^{16}	1.261×10^{16}
Tot. decay rate	s^{-1}	5.441×10^{12}	2.495×10^{13}	2.362×10^{13}
Rel. balance err.	–	1.559×10^{-6}	1.546×10^{-6}	1.545×10^{-6}

(c) $Sc_t = 1.20$

Quantity	Units	$k-\varepsilon$	$k-\omega$	$k-\omega-SST$
Tot. precipitate	–	5.989×10^{17}	2.734×10^{18}	2.599×10^{18}
Tot. deposit	–	1.263×10^{21}	1.261×10^{21}	1.261×10^{21}
Tot. source	s^{-1}	1.263×10^{16}	1.263×10^{16}	1.263×10^{16}
Tot. dep. rate	s^{-1}	1.263×10^{16}	1.261×10^{16}	1.261×10^{16}
Tot. decay rate	s^{-1}	5.989×10^{12}	2.734×10^{13}	2.599×10^{13}
Rel. balance err.	–	1.526×10^{-6}	1.545×10^{-6}	1.556×10^{-6}

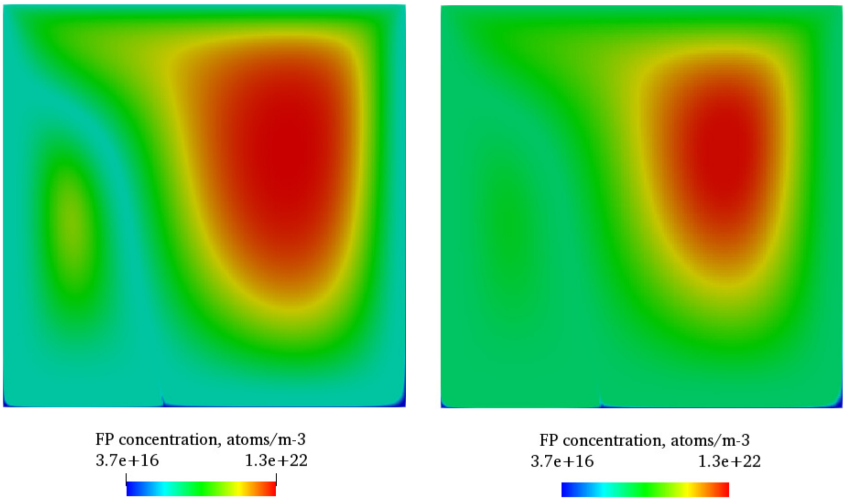

Figure 3.9: FP precipitate concentration C^p for the cavity benchmark case. On the left, base case with direct formation of the solid precipitate phase; on the right, simplified equilibrium precipitation model.

3.3 Simplified precipitation

Previous analyses have been conducted following the hypothesis of direct formation of FPs particles in the precipitated solid phase, by neglecting the potential existence of a dissolved phase and local temperature effects on precipitation. In this last case, a simple precipitation/dissolution reaction involving a single metallic species is considered, with common exponential dependence of the equilibrium constant on local temperature, as detailed in Section 2.4.3. The geometry, the case setup and the main physical parameters are the same of Section 3.1, with the addition of the following guess values for the equilibrium constants:

$$K_1 = K(T_1) = 10^{-6}$$
$$K_2 = K(T_2) = 10^{-5}$$

with T_1 and T_2 equal respectively to 1000 K and 1200 K.

Fig. 3.9 shows the comparison between the base case where no equilibrium precipitation/dissolution reaction is considered (all FP atoms are born directly as precipitate) and the case with chemical model with parameter values as described earlier. Non-negligible discrepancies are observed, suggesting that even in a simplified test case temperature-dependent effects on precipitation may sensibly affect precipitate distributions within the reactor.

Chapter 4

Large Eddy Simulation of the MSFR

This Chapter deals with a preliminary assessment of the feasibility of Large Eddy Simulation (LES) modelling for multiphysics MSFR applications. As shown in Chapter 3, standard CFD models based on the RANS approach can be a useful tool in the analysis of complex systems such as the MSFR. However, accurate modelling of turbulent phenomena is often crucial due to the wide range of flow characteristics which might be found in different operating conditions or physical regions of the system. This is especially true when turbulent diffusion plays a dominant role in the transport of simulated quantities, as in the case of FPs in the MSFR. More sophisticated approaches such as LES offer the potential for more detailed predictions of three-dimensional flows, at the cost of increased computational requirements.

LES is a numerical technique that, in contrast to more traditional approaches like RANS, resolves the largest turbulent eddies in the flow while modelling the smaller ones. This method provides a more accurate description of turbulence and enables for the investigation of complex flows over a wide variety of spatial and temporal scales. LES originated in the early 1970s [47, 16] from the study of turbulent flows in atmospheric and oceanic settings. The technique was first applied to engineering problems in the late 1980s, and it has since been employed in a wide range of applications, including aerodynamics, combustion, and multiphase flows. The filtering of the flow equations to remove small-scale turbulent fluctuations is the main feature of LES. This filtering is often achieved with a low-pass filter, which removes high-frequency flow field components. The filtered equations are then solved, with just the largest turbulent scales included, while the smallest scales are accounted for by means of appropriate sub-grid scale (SGS) models. LES provides various advantages over other approaches to turbulence modelling. One of its primary advantages is its ability to capture unstable and nonlinear effects, which can be useful in a variety of engineering applications. Furthermore, as compared to RANS models, LES delivers more accurate predictions of mean flow volumes and turbulence statistics.

In nuclear engineering, LES is becoming an increasingly important tool for simulating the behaviour of reactor systems [37]. Nuclear reactors operate in highly complex and dynamic environments, with fluid flows, heat and mass transfer, and radiation transport all playing relevant roles at different space and time scales. LES can provide a detailed description of these phenomena, allowing a better understanding of reactor behaviour and improve safety. LES can be used to predict coolant turbulent mixing and to study the effects of turbulence on heat transfer. LES modelling has been recently employed for the analysis of natural circulation in molten salt loops with distributed heating [5], but multiphysics studies of the MSFR based on LES have not been performed yet due to the intrinsic complexity of coupled neutronics/thermal hydraulics simulation and to the increased computational cost. In multiphysics analysis, LES can also be used to simulate coupled phenomena such as fluid-structure interaction, or fluid-particle interaction. This can be important in nuclear reactor design, where the behaviour of coolant flow around fuel assemblies, or the transport of fission products in the coolant, can have significant effects on reactor performance. Besides the increased accuracy, LES allows for the prediction of turbulent fluctuations of reactor quantities in steady-state operation, which might be significant in strongly coupled non-linear systems such as the MSFR.

In the following, three different meshes characterised by same meshing approach but different cell counts are first tested. Then, the intermediate mesh is selected to benchmark four different SGS models. Results are compared in terms of transient profiles of integral properties of the reactor.

4.1 Case setup

4.1.1 Geometry and mesh

A three-dimensional model of the MSFR has been developed, describing 1/16 of the complete cyclic geometry (Figure 4.1a). The symmetry of the problem has been exploited to reduce the total cell count. The model features a toroidal core region whose shape has been selected to prevent disturbances in the fuel flow and excessive recirculation, as opposed to the cases from Section 3.2. The lateral surfaces of the core are symmetry ones - since are internal to the fluid domain - while all the other surfaces are treated as walls. The shape of the out-of-core region is not optimised and serves the purpose to conserve the total volume of salt (18 m^3 for the whole reactor) and apply a simplified momentum source and energy sink, to mimic the effect of the pump and the primary heat exchanger in analogy to Section 3.2.

The meshes have been produced by first subdividing the domain in blocks and then employing a dominant hexahedral algorithm. Following this approach, the resulting meshes for the most part are divided into structured blocks with limited aspect ratio and non-orthogonality. Good quality cells are therefore produced consistently and with similar size across the entire domain. The target cell size for each of the 3 meshes has been chosen to roughly double the total cell count between each mesh iteration, such that the most refined mesh is roughly 4 times larger than the least refined one (Table 4.1). No mesh refinement has been considered due to issues in the production of good quality

Table 4.1: Main 3D MSFR mesh information.

Name	Cell count	Cell size (cm)
300k	3.21×10^5	1.25
700k	7.33×10^5	1.00
1200k	1.21×10^6	0.75

meshes for this complex 3D geometry. The obtained mesh is therefore not suited for the resolution of the boundary layers and, unfortunately for the moment being, for FP transport calculations.

4.1.2 Initialisation

To provide meaningful initial condition for transient LES simulations, the system has been initialised in critical steady-state conditions, at 3000 MW of reactor power, using a standard k-ε model. The pump section has been calibrated to match a total reactor flow rate of $1.9 \times 10^4\,\mathrm{kg\,s^{-1}}$, through a custom momentum source developed ad-hoc which adjusts the linear source coefficients along solver iterations based on an action proportional to the mismatch between the current and desired volumetric flow rate measured at the hot leg inlet. The main physical case parameters are summarised in Table 4.2.

The selection of the turbulence model naturally affects the beginning of transients, but no particular care is devoted to this aspects since initialisation only serves the purpose to define reasonable and consistent initial conditions. Other methods might have been used as well, e.g. by targeting directly both total LES reactor power and mass flow rate; in the cases here described, initial reactor power and mass flow rate are consistent with the RANS model adopted for initialisation, so that both of them are free to adjust after transient LES simulation starts.

4.1.3 LES turbulence modelling

There are several SGS models available for LES, each with its own set of assumptions and features. The choice of SGS model can affect the accuracy and computational cost of the LES simulation. Four different SGS models are here employed, among the ones offered by the OpenFOAM library:

1. Smagorinsky [47]
2. k Equation [56]
3. Dynamic k Equation [29]
4. Wall Adapting Local Eddy-viscosity (WALE) [38]

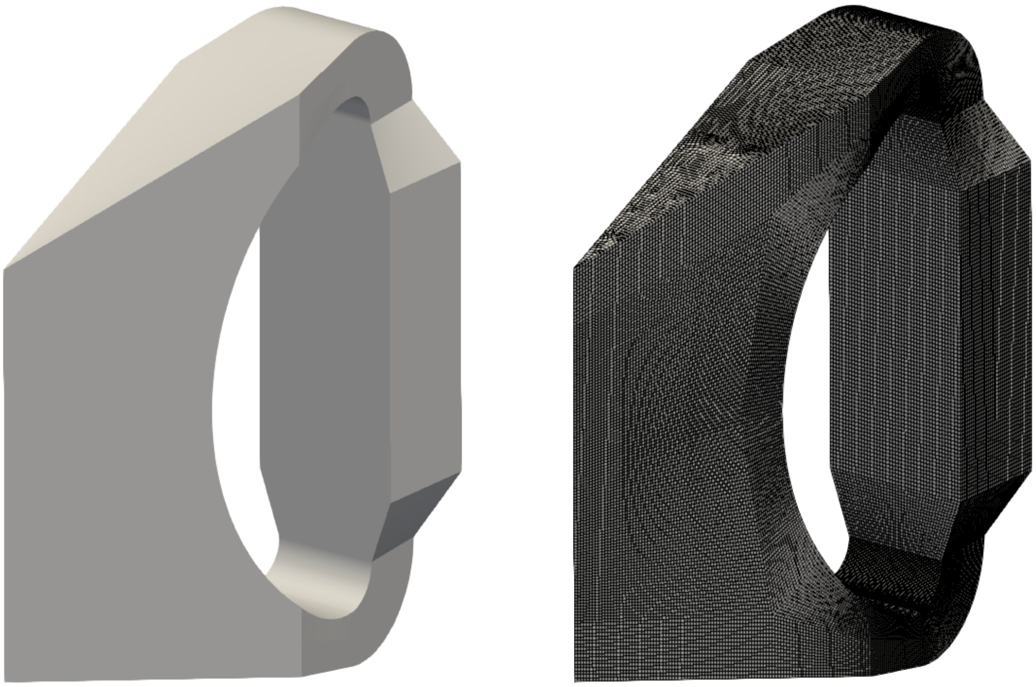

(a) Geometry.

(b) Mesh.

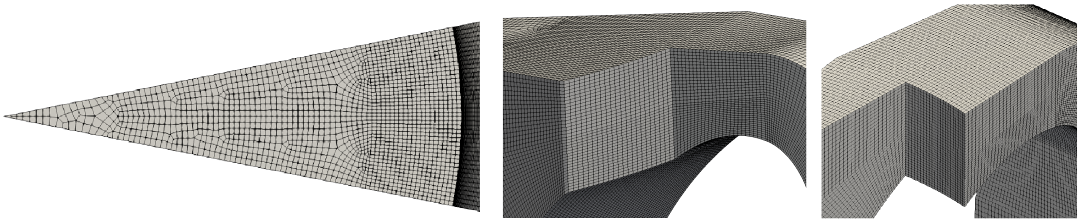

(c) Mesh details.

Figure 4.1: MSFR 3D case: a 1/16 cyclic domain is chosen to reduce the computational requirements and the resulting hexahedral mesh is predominantly structured.

Table 4.2: Main physical parameter values adopted for the 3D MSFR case.

Parameter	Symbol	Units	Value
Density	ρ	$\mathrm{kg\,m^{-3}}$	4.307×10^3
Kinematic viscosity	ν	$\mathrm{m^2\,s^{-1}}$	5.89×10^{-6}
Specific heat capacity	c_p	$\mathrm{J\,kg^{-1}\,K^{-1}}$	1.594×10^3
Thermal expansion coeff.	β_T	$\mathrm{K^{-1}}$	1.912×10^{-4}
Ref. temperature	T_0	K	973
Prandtl number	Pr	–	23.78
Turb. Prandtl number	Pr_t	–	0.85
Schmidt number	Sc	–	20.0
Turb. Schmidt number	Sc_t	–	0.85
Heat removal coeff.	γ_r	$\mathrm{W\,m^{-2}\,K^{-1}}$	2.5×10^6
Heat sink temperature	T_{sink}	K	900

The Smagorinsky model is one of the most commonly used SGS models for LES. It is a linear model that assumes that the SGS turbulence is isotropic and homogeneous. It models the sub-grid scale viscosity using a constant value that is proportional to the square of the grid spacing. The Smagorinsky model is computationally efficient but can lead to over-dissipation of energy in high Reynolds number flows. It is based on the eddy viscosity assumption, which postulates a linear relationship between the SGS shear stress and the resolved rate of strain tensor. This model serves as a base for other SGS models.

As in the case of the Smagorinsky SGS model, the one equation eddy viscosity SGS model (k Equation) uses the eddy viscosity approximation. The two models differentiate with respect to how they compute the sub-grid scale kinetic energy: the Smagorinsky model assumes the local equilibrium while the one equation eddy viscosity model solves a transport equation.

The WALE model is a wall-adapting sub-grid scale model that takes into account the effects of near-wall turbulence. It is an algebraic eddy viscosity model (0-equation model) as with the Smagorinsky SGS model, but it uses a length scale that adapts to the local flow conditions and is based on the distance to the nearest wall. The WALE model is computationally efficient and accurate for near-wall flows.

The purpose of this study is to compare different SGS-LES models with no accurate prior analysis on flow characteristics. The scarce level of geometrical detail on most parts of reactor internals (especially in the out-of-core region) and the lack of experimental data do not allow, both a priori and a posteriori, to prefer one model over the others. It is nevertheless useful to provide a rough comparison of different models for future reference, and to draw some preliminary observation of dynamical behaviour related to reactor turbulence.

4.2 Results and discussion

Free-dynamics transients of 25 s have been first simulated for the three different adopted meshes, with a fixed time step of 10^{-3} s. Figures 4.2a, 4.3a, 4.4a, 4.5a, 4.6a and 4.7a show the results respectively for the normalised total power, average temperature, normalised total mass flow rate, normalised total fission rate, normalised integrated concentration of 1st family delayed neutron precursors and normalised integrated concentration of 8th family delayed neutron precursors.

In general it is observed that after an initial transient, all reactor quantities which follow faster dynamics than the simulation time window settle around a new operating state. This is not surprising due to the mismatch between the turbulence modelling approach followed for the initialisation (RANS standard k-ε) and for the transient (LES Smagorinsky SGS). It is the case e.g. of reactor power, average temperature, mass flow rate, fission rate and the population of shortest-lived (8th) delayed neutron precursors. Longest-lived delayed neutron precursors, on the opposite, follow a much slower and smoother dynamics, which is dominated by their slow decay. Significant fluctuations are observed, suggesting that turbulence plays a substantial role in reactor dynamics which is entirely neglected by time-averaged RANS approaches. It is the case, for instance, of reactor power which is affected by quite fast oscillations with average amplitudes around few percents. The three meshes present overall similar results, showing that the dominant underlying physics is correctly resolved without the need for excessive refinement. This applies to the shape of the initial part of the transient, and to the fluctuations in the remainder in terms of average values, amplitudes and frequencies. For this reason, the intermediate "700k" mesh is selected for the successive analysis.

Instantaneous solution fields for this mesh, on a vertical midplane section, are shown for completeness in Figure 4.8 (initial) and Figure 4.9 (after 20 s). From comparison with the initial RANS fields, no particular differences in the localisation and size of turbulent structures are observed. For instance, stagnation zones close to top/bottom walls in the core region, close to toroidal walls and in the heat exchange regions are roughly of the same size and shape. Neutron flux fields, on the other side, are practically not affected.

Again, free-dynamics transients of 25 s have been simulated for the four selected SGS models, with a fixed time step of 10^{-3} s. Also in this case, Figures 4.2b, 4.3b, 4.4b, 4.5b, 4.6b and 4.7b show the results respectively for the normalised total power, average temperature, normalised total mass flow rate, normalised total fission rate, normalised integrated concentration of 1st family delayed neutron precursors and normalised integrated concentration of 8th family delayed neutron precursors. The same general considerations apply also for these cases, with the addition of the discrepancies between different SGS models. The overall dynamics show no significant differences, with oscillations qualitatively of similar frequency and amplitude. This shows that all the considered SGS models introduce approximately the same dynamics in the reactor simulation and their choice is somewhat equivalent as far as integral dynamics are considered. Average steady-state values differ, with each model predicting a different increase in reactor power except for the Dynamic k Equation, which remarkably predicts an almost unvaried or even slightly

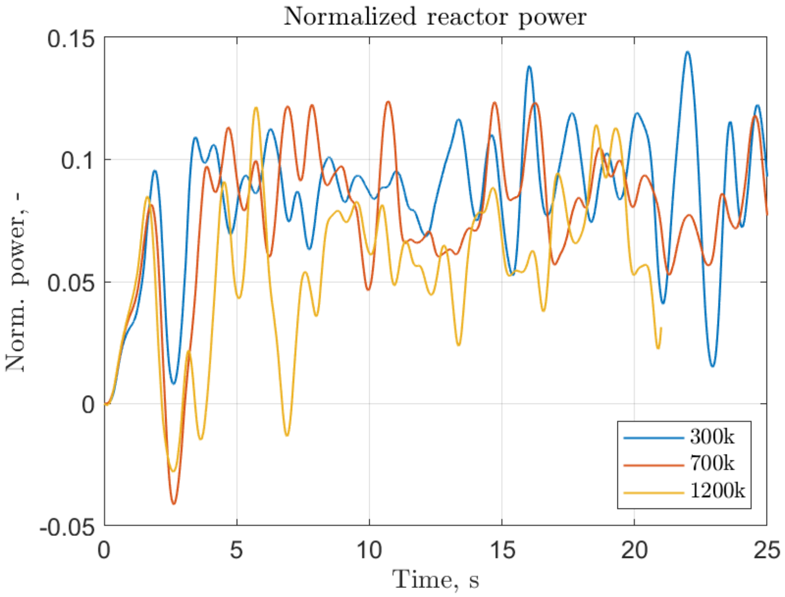

(a) Comparison among different mesh refinements.

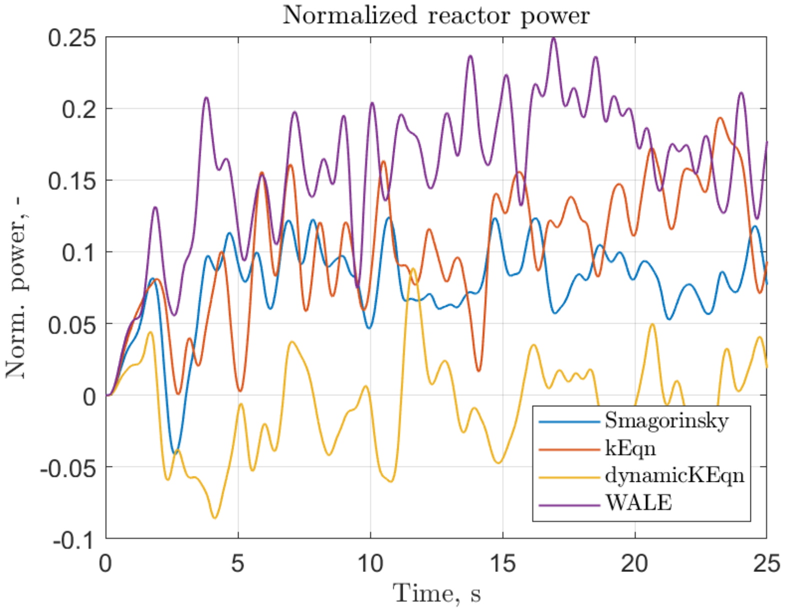

(b) Comparison among different SGS models.

Figure 4.2: Normalised total reactor power during LES transients for different mesh refinements and SGS models.

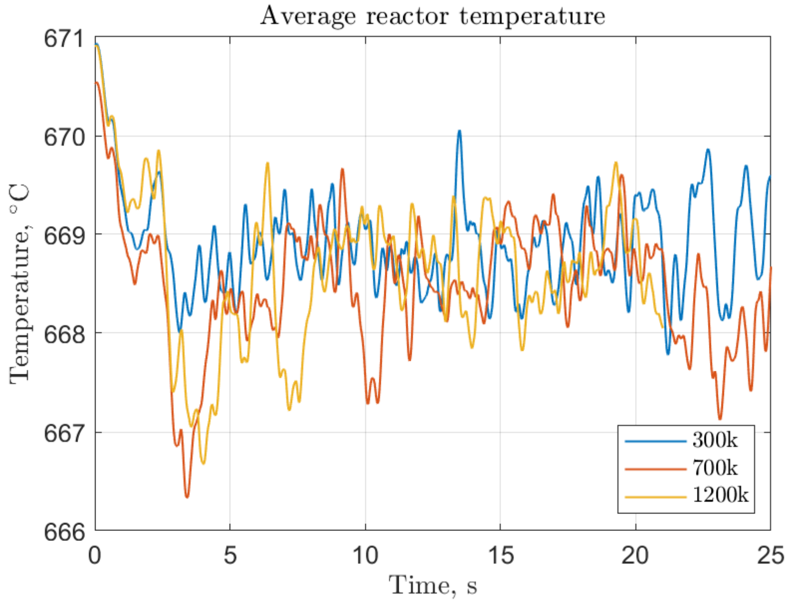

(a) Comparison among different mesh refinements.

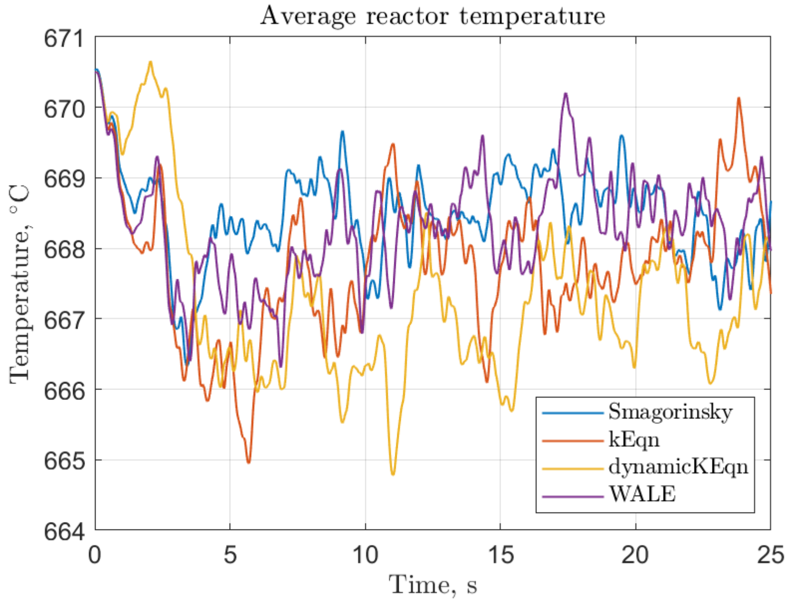

(b) Comparison among different SGS models.

Figure 4.3: Average reactor temperature during LES transients for different mesh refinements and SGS models.

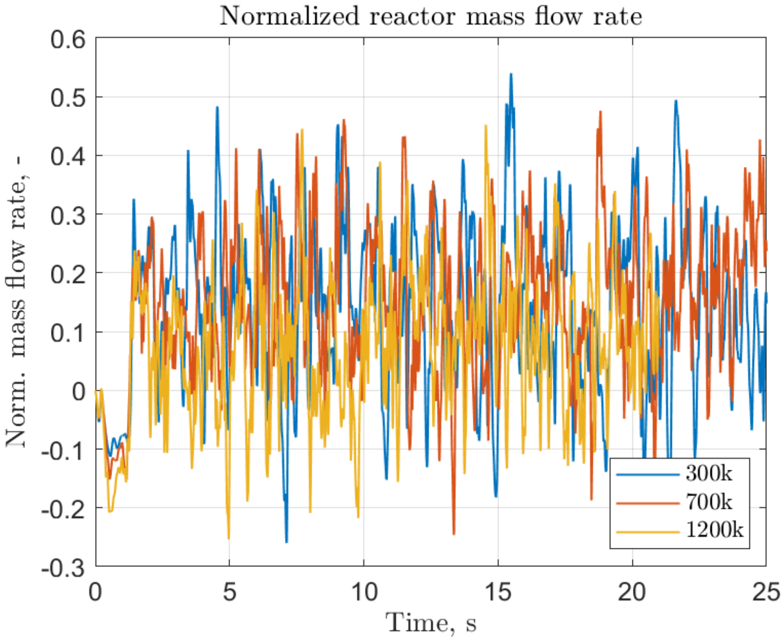

(a) Comparison among different mesh refinements.

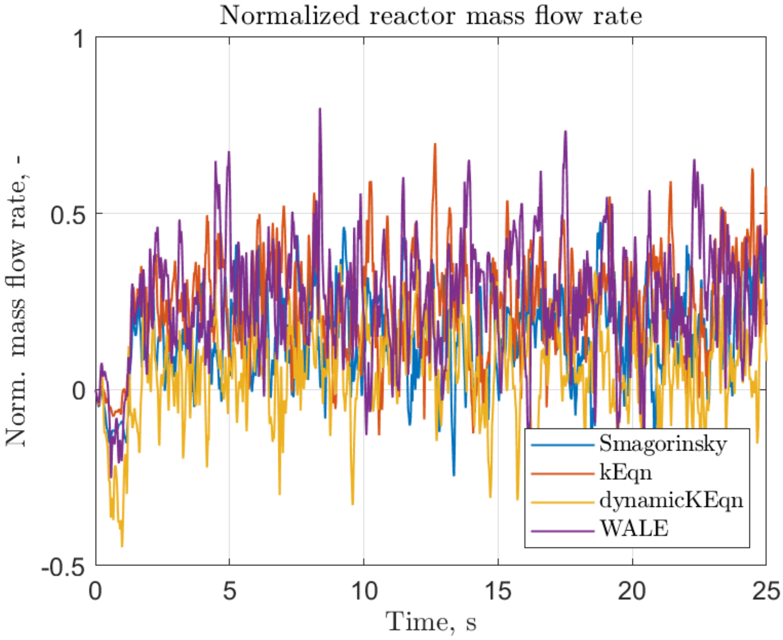

(b) Comparison among different SGS models.

Figure 4.4: Normalised total reactor mass flow rate during LES transients for different mesh refinements and SGS models.

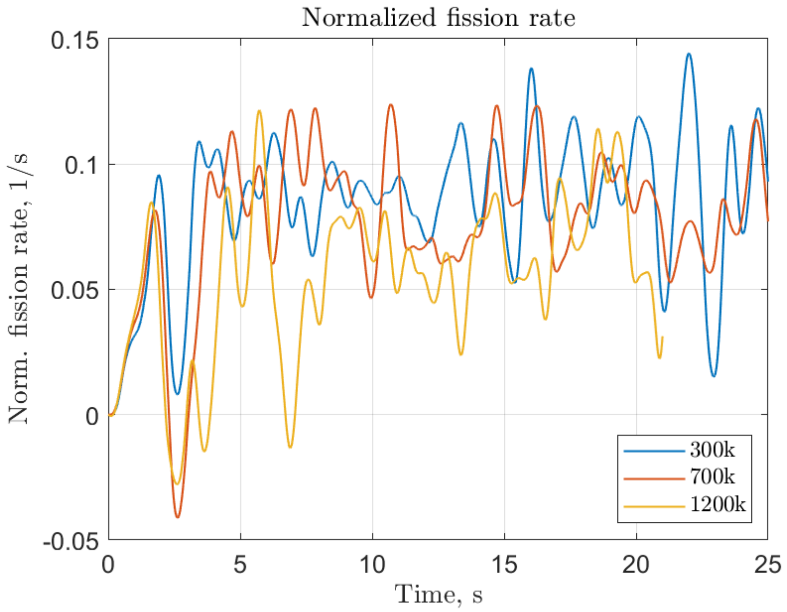

(a) Comparison among different mesh refinements.

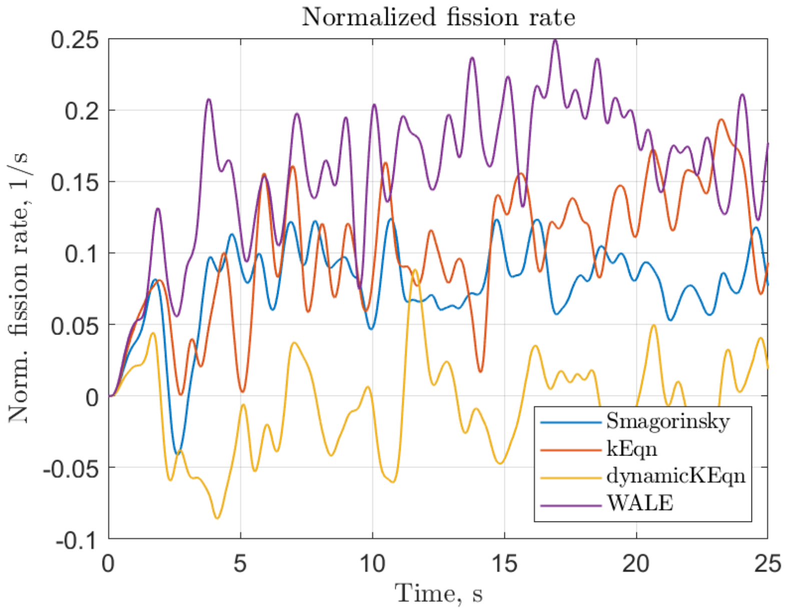

(b) Comparison among different SGS models.

Figure 4.5: Normalised total reactor fission rate during LES transients for different mesh refinements and SGS models.

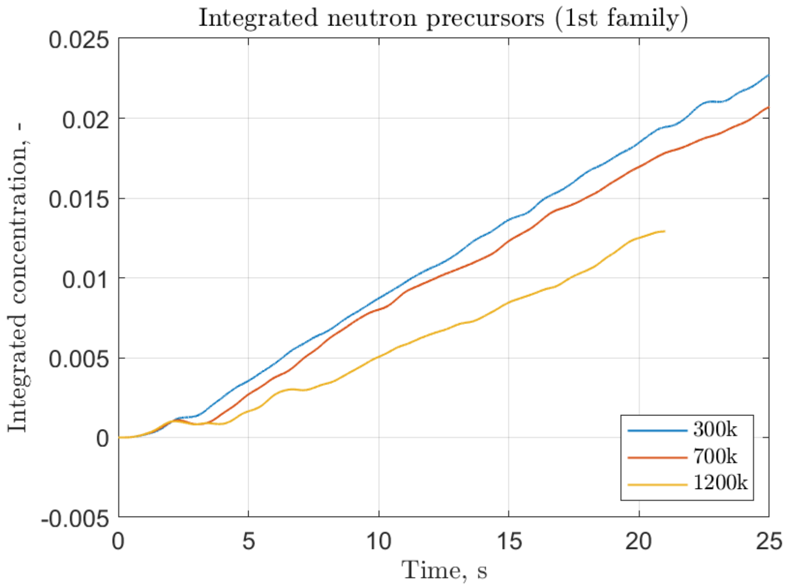

(a) Comparison among different mesh refinements.

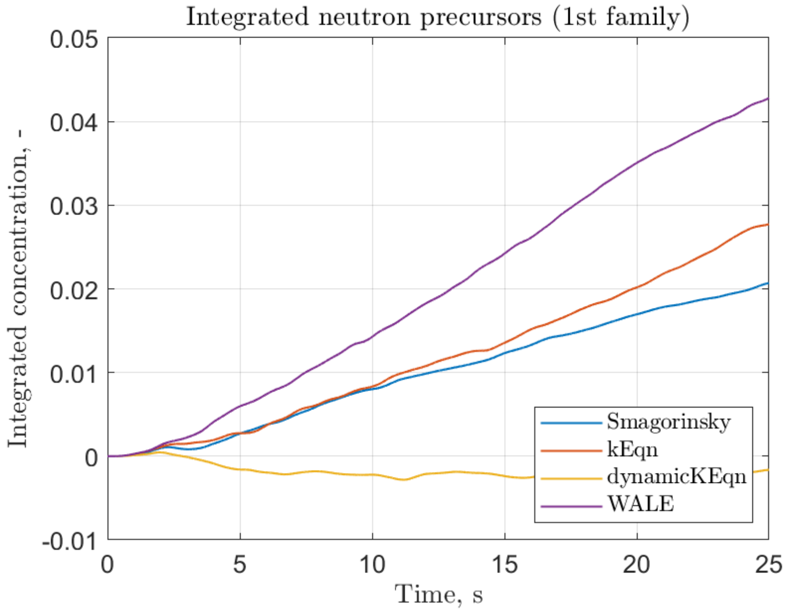

(b) Comparison among different SGS models.

Figure 4.6: Normalised integrated concentration of 1st family of delayed neutron precursors during LES transients for different mesh refinements and SGS models.

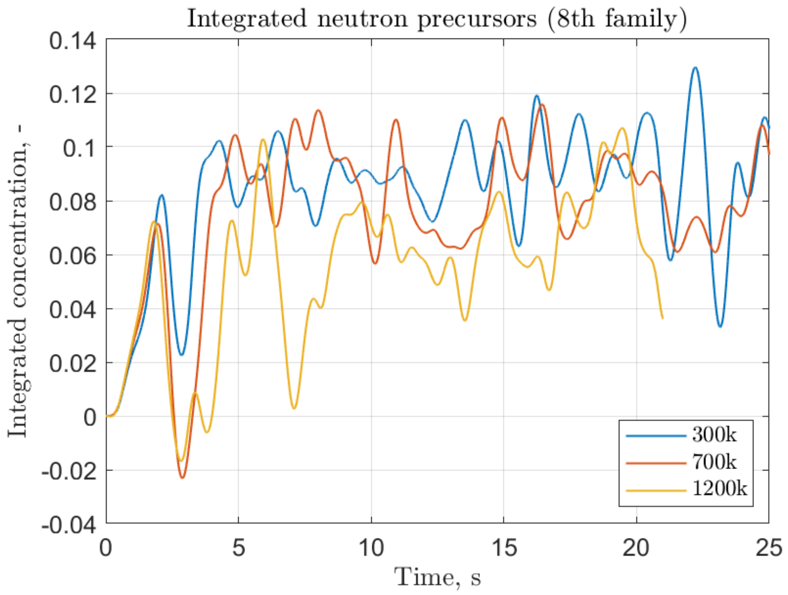

(a) Comparison among different mesh refinements.

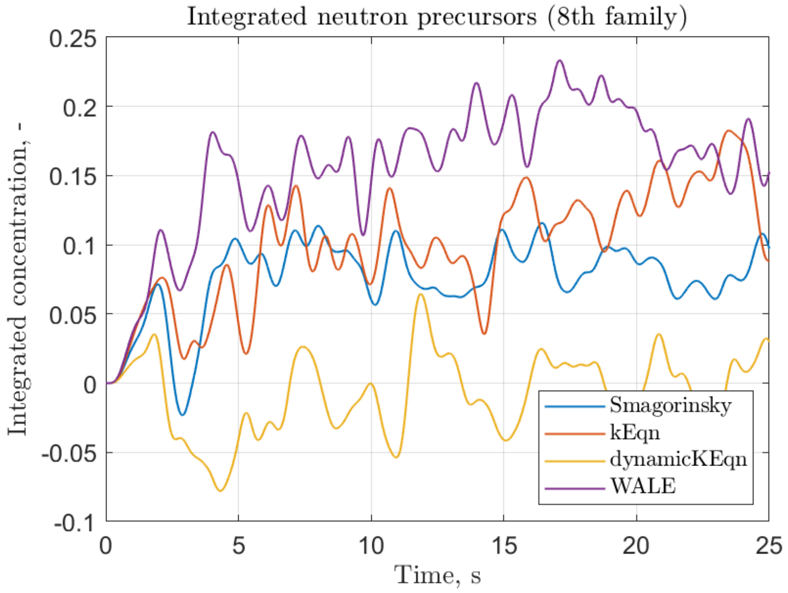

(b) Comparison among different SGS models.

Figure 4.7: Normalised integrated concentration of 8th family of delayed neutron precursors during LES transients for different mesh refinements and SGS models.

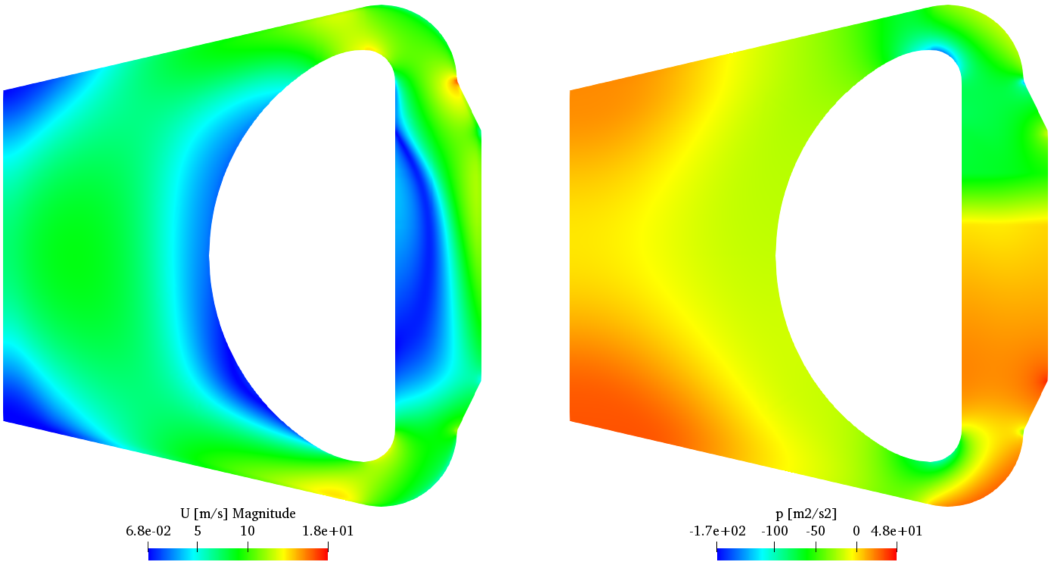

(a) Velocity (magnitude).

(b) Pressure.

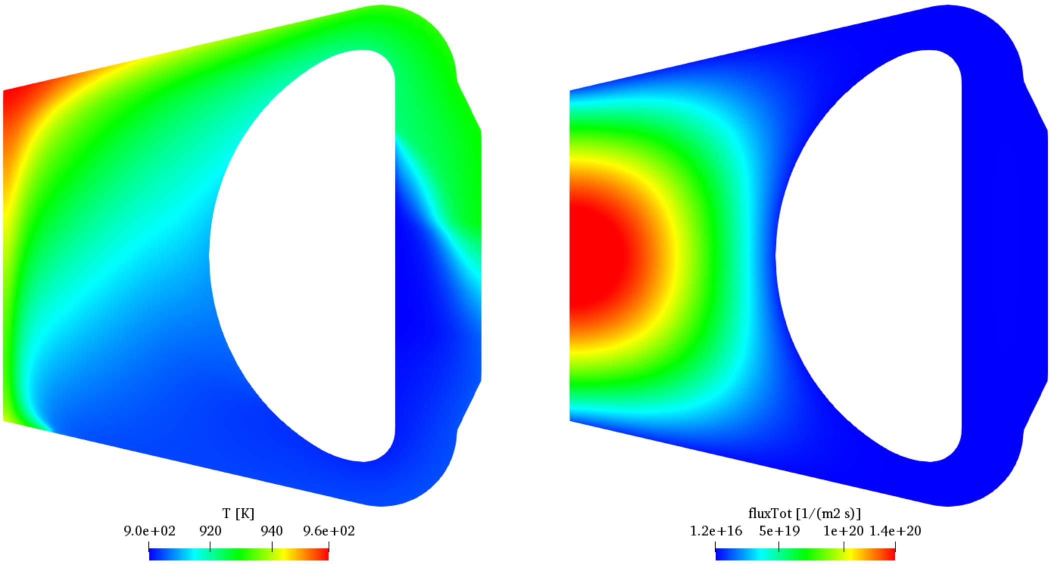

(c) Temperature.

(d) Total neutron flux.

Figure 4.8: Initial fields from standard k-ε RANS for LES simulation of “700k” mesh on a vertical midplane section.

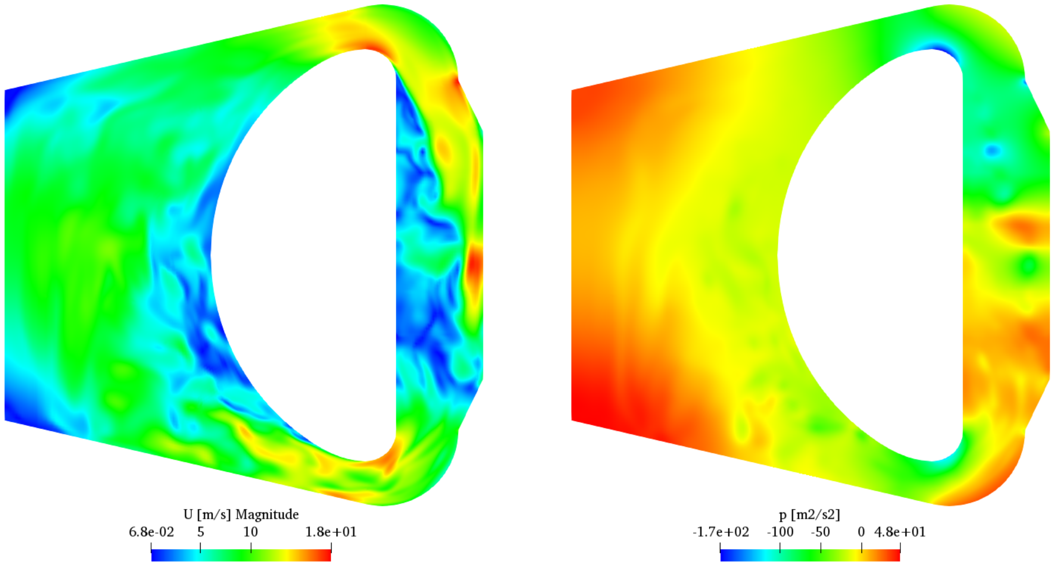

(a) Velocity (magnitude).

(b) Pressure.

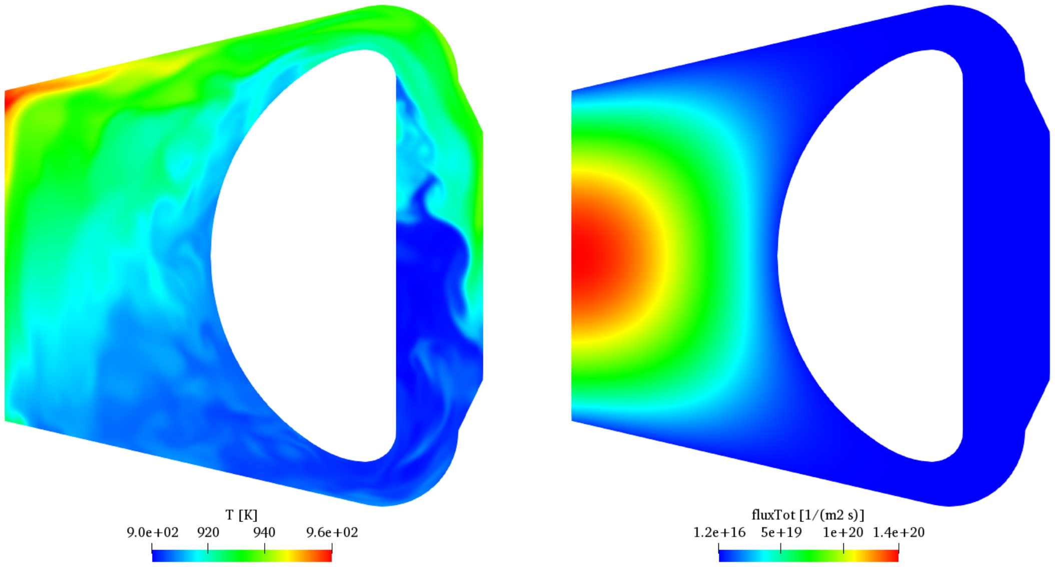

(c) Temperature.

(d) Total neutron flux.

Figure 4.9: Solution fields after 20 s of Smagorinsky LES simulation of “700k” mesh on a vertical midplane section.

decreased steady-state condition. Longer transients, however, should be simulated to allow for the acquisition of proper statistics and to draw more quantitative conclusions.

Despite preliminary, the outcomes of the study demonstrate the potential of LES modelling for the dynamic analysis of the MSFR and for a more detailed prediction of turbulent transport of quantities of interest. Power oscillations are estimated to be significant, if not addressed properly both at the reactor design and operation stages, and consistently across different SGS models. Upon further confirmation of the results from this preliminary analysis, it appears evident that correct estimation of turbulent fluctuation is crucial to the development of appropriate reactor designs and control strategies. Moreover, turbulent fluctuations in liquid fuel reactors are expected to interact with other reactor analysis aspects which are here neglected and will need to be addressed, e.g. the formation and movement of voids and bubbles, cyclic thermo-mechanical loads and potential resonance with the natural frequencies of structural elements.

Chapter 5

Conclusion

In this work, the development of transport models for the solid fission products in the Molten Salt Fast Reactor was addressed. Transport models based on a Eulerian single-phase framework were implemented in a consolidated MSFR multiphysics simulation framework based on the open-source finite-volume library OpenFOAM.

The resulting models have been verified against analytical solutions for simplified test cases, based on an extended version of the Graetz problem. Results show the good agreement, proving the correct implementation of the transport and deposition mechanisms considered and the capability of OpenFOAM in treating coupled deposition and decay phenomena of different relative intensities. The proposed approach constitutes a computationally efficient framework to extend the capabilities of CFD-based multiphysics MSFR calculations towards the simulation of solid fission products transport. The analytical model used for verification has been developed specifically for this study, since the simultaneous presence of distributed internal generation, radioactive decay and mixed deposition boundary condition in a Graetz-like problem represents an original contribution. The resulting analytical model could therefore constitute a useful benchmark for future developments of the FPs migration model and for other similar MSFR applications.

The developed transport models have then been tested on two separate MSFR cases, namely the CNRS benchmark lid-driven cavity problem and the axisymmetric EVOL geometry. The main subjects of the investigation were the prediction of particle deposition fluxes and the analysis of related numerical issues arising from the commonly adopted assumption of "perfectly adsorbing" walls in combination with distributed particles source. The influence of different turbulence modelling approaches and turbulent diffusion parameters on particle distributions and deposition fluxes was also tested in the EVOL case. Analytical results based on a simplified laminar parallel-plates geometry have been used to determine the expected particle concentration gradients close to solid walls. It was observed that the interplay between homogeneous Dirichlet boundary conditions and the presence of a non-negligible particle source in the wall layers produces steep gradients, and therefore poses the need for significant mesh refinement in the wall regions. Furthermore, the presence of steep gradients and the need to correctly resolve the boundary layers require, besides an adequate mesh refinement, the adoption of second order discretization schemes combined with gradient limiting to avoid numerical instability. Wall layer thicknesses in both the cavity and EVOL cases have not been found in complete agreement with the analytical estimate, suggesting a relevant role of geometry, local velocity profiles and of turbulence. However, prescribed mesh refinement based on the analytical model proved sufficient to adequately resolve wall concentration gradients in all simulated cases. The comparison of three different common turbulence models, namely the standard $k-\varepsilon$, the standard $k-\omega$ and the $k-\omega-SST$ models, with different turbulent Schmidt number values has shown a significant influence on the particle concentration distributions, given the discrepancies in the predicted velocity and eddy diffusivity fields. However, the deposition rates, which are one of the main subjects of the analysis, were much less affected, suggesting a certain flexibility in the choice of turbulence models and parameters as far as deposition is concerned. This effect is probably due to the fact that, in the concentration boundary layer, transport is dominated by diffusion and turbulent diffusivity vanishes at walls. In connection with this aspect, it was found that, in steady-state conditions, a large fraction (more than 99.9%) of particles borne in the fuel are found on walls, demonstrating the efficiency of transport mechanisms within the reactor. This aspect might prove even more relevant when long-lived metallic species are considered, given the competition between the deposition and decay mechanisms in determining the fate of produced particles. Furthermore, results from a preliminary simplified test case have shown a non-negligible role of precipitation modelling on the distribution of solid precipitate particles, suggesting the need for further developments.

Finally, a preliminary Large Eddy Simulation multiphysics model of the MSFR was developed, relying on the multiphysics incompressible single-phase solver developed and described in this work. The use of LES as a dynamic analysis tool for the MSFR is essentially a new and exciting research topic, with a wide range of potential applications. In this work, a 3D MSFR geometry was developed and used to test different LES SGS models available as part of the OpenFOAM library. Transient simulation evolving in free dynamics from steady-state conditions has shown, qualitatively, no significant discrepancies among different models in terms of frequency and amplitude of the turbulent oscillations introduced by LES modelling, suggesting their substantial equivalence for the dynamic analysis of the MSFR. On the other hand, predicted transients have shown non-negligible effects due to turbulence on main reactor integral parameters, with amplitudes e.g. of few percents for the total reactor power. These preliminary results will need to be confirmed with further studies, but might suggest the insurgence of interesting dynamic phenomena and new challenges for dynamics and control of the MSFR.

5.1 Further work

Despite relevant for the analysis of MSFR behaviour, test cases were selected to simplify the numerical analysis and to reduce the computational requirements. Future work will include the analysis of FPs transport in more realistic 3D reactor simulations. The study of the 2D EVOL case has shown that the effect of turbulent transport in relatively complex geometries should not affect dramatically concentration gradients close to walls, giving reasonable estimates of the required mesh refinement. Arbitrary and flexible mesh refinement in more complex 3D geometries, however, may prove a challenging task. In this perspective, it is worth noting that 3D models, especially following a LES approach, require a significant increase in the cell count (above 10^6), with a computational cost in the range of several thousands CPU-hours for transients of a few tens of seconds. This is worsened by the need to fully resolve boundary layers in generic geometries, increasing further the cell count and the numerical complexity.

Regarding other limitations of the multiphysics transport model, the integration with a full-featured chemistry model to distinguish between the solid and the dissolved species might further improve the descriptive capabilities of the multiphysics framework. To this aim, direct coupling of OpenFOAM MSFR solvers with an external equilibrium thermochemistry code, such as Thermochimica [42], might be an interesting option.

Other possible limitations of the adopted approach include the adoption of pure concentration-driven diffusive transport, which is strictly valid only in the approximation of particles of very small size. Further study will be needed to assess the range of validity of such assumption for MSFR applications and to possibly extend the methodology to more advanced particle transport models. This might however add excessive numerical/computational complexity, making the application of the multiphysics approach to real-scale MSFR simulations troublesome.

Appendix A

Supplement to the Analytical Model

A.1 Computation of M(a,b;z)

The computation of the obtained analytical results is conditioned, above all, on the reliable evaluation of $M(a,b;z)$. This task is far from trivial and is still widely addressed in the literature [41, 27]. Different techniques have been proposed for different ranges of the parameters a, b and of the argument z, but reliable and numerically efficient methods for the application in a wide range of cases are not available.

The most straightforward methods make use of the definition (2.59) in a more efficient recursive fashion:

$$M(a,b;z) = \sum_{k=0}^{\infty} T_k(a,b;z) \tag{A.1}$$

where

$$T_k(a,b;z) = \frac{(a)_k}{(b)_k}\frac{z^k}{k!} = \left(\frac{a+k-1}{b+k-1}\frac{z}{k}\right) T_{k-1}(a,b;z) \tag{A.2}$$

for $k > 0$ and with $T_0(a,b;z) = 1$. Such series is convergent for all finite z and provided that b is not a non-positive integer. Therefore, the series can be truncated as

$$M(a,b;z) \approx M_N(a,b;z) = \sum_{k=0}^{N} T_k(a,b;z) \tag{A.3}$$

for a certain N. The value $N(a,b,z)$ can be simply selected case by case as the smallest k for which holds

$$\frac{|T_{k+1}(a,b;z)|}{|M_k(a,b;z)|} < \varepsilon \tag{A.4}$$

for a suitable ε. Since it can be observed in some cases that a convergence criterion based on a single-term evaluation is not sufficient to ensure convergence, a more robust criterion can be used which is based on two successive terms. Hence the additional condition

$$\frac{|T_{k+2}(a,b;z)|}{|M_{k+1}(a,b;z)|} < \varepsilon \tag{A.5}$$

This approach proves to be accurate up to machine precision in a relatively broad range of cases, provided that $|z|$ and $|a|$ are not "too large". In the present work, expressions like

$$z = \beta_n \, \hat{y}^2 \tag{A.6}$$

$$a = \frac{1-\beta_n}{4} + \frac{Da}{4\beta_n} \tag{A.7}$$

need to be evaluated, with both $|z|$ and $|a|$ monotonically increasing functions of β_n, and the approach based on a simple power series truncation may lead to inaccuracies for large n. Experience has shown that the computation of β_n by means of (2.63) in MATLAB fails for $n \gtrsim 50$ ($\beta_n \gtrsim 200$). Further values can be easily obtained by observing that $\beta_{n+1} - \beta_n$ becomes approximately constant for sufficiently large n. However, since the computation of Y_n becomes unreliable regardless of the correctness of β_n, care must be paid if more than ≈25 eigenfunctions are needed.

Most difficulties with large parameters and argument arise from numerical cancellation occurring in subsequent large terms. This can be avoided in an arbitrary-precision arithmetic framework, as is done in the Arb library [26]. The Arb library implements arbitrary-precision interval arithmetic and allows for the rigorous evaluation of several special functions including $M(a,b;z)$. In the present work, Arb functionalities have been employed to ensure accurate evaluation of $M(a,b;z)$ up to the number of significant digits corresponding to machine precision.

A.2 Evaluation of normalization integrals

Given the numerical issues discussed earlier, the evaluation of the constants C_n and D_n needs to be addressed carefully. By direct manipulation of the eigenvalue problem (2.54) it is easily shown that

$$\begin{aligned} D_n = 2\int_0^1 (1-\hat{y}^2)\, Y_n \,\mathrm{d}\hat{y} &= \frac{2}{\beta_n^2}\left(Da \int_0^1 Y_n \,\mathrm{d}\hat{y} - \left[\frac{\mathrm{d}Y_n}{\mathrm{d}\hat{y}}\right]_0^1 \right) \\ &= \frac{2}{\beta_n^2}\left(\frac{Da}{2} E_n + \frac{Da\,Sh}{Da+\Delta} Y_n(1) \right) \end{aligned} \tag{A.8}$$

where

$$E_n = \int_{-1}^1 Y_n \,\mathrm{d}\hat{y} = 2\int_0^1 Y_n \,\mathrm{d}\hat{y} \tag{A.9}$$

In a similar fashion it is possible to express also C_n in simpler terms. Since the β_n are simply the β values for which the eigenfunctions Y_n satisfy both the differential equation and the boundary conditions, Y can denote a generic solution which doesn't necessarily satisfy the boundary conditions. Then, by multiplying the equation for Y_n by Y and the equation for Y by Y_n, and by subtracting the two resulting equations:

$$\frac{\mathrm{d}^2 Y}{\mathrm{d}\hat{y}^2} Y_n - \frac{\mathrm{d}^2 Y_n}{\mathrm{d}\hat{y}^2} Y + (\beta^2 - \beta_n^2)(1 - \hat{y}^2)\, Y\, Y_n = 0 \tag{A.10}$$

Then, through manipulation and integration:

$$\begin{aligned} \int_0^1 (1 - \hat{y}^2)\, Y\, Y_n \,\mathrm{d}\hat{y} &= \frac{1}{\beta^2 - \beta_n^2} \int_0^1 \left(\frac{\mathrm{d}^2 Y_n}{\mathrm{d}\hat{y}^2} Y - \frac{\mathrm{d}^2 Y}{\mathrm{d}\hat{y}^2} Y_n \right) \mathrm{d}\hat{y} \\ &= \frac{1}{\beta^2 - \beta_n^2} \left[\frac{\mathrm{d}Y_n}{\mathrm{d}\hat{y}} Y - \frac{\mathrm{d}Y}{\mathrm{d}\hat{y}} Y_n \right]_0^1 \\ &= \frac{1}{\beta^2 - \beta_n^2} \left[\frac{\mathrm{d}Y_n}{\mathrm{d}\hat{y}} (Y - Y_n) - Y_n \left(\frac{\mathrm{d}Y}{\mathrm{d}\hat{y}} - \frac{\mathrm{d}Y_n}{\mathrm{d}\hat{y}} \right) \right]_0^1 \end{aligned} \tag{A.11}$$

From this, it directly follows

$$\begin{aligned} C_n &= 2 \int_0^1 (1 - \hat{y}^2)\, Y_n^2 \,\mathrm{d}\hat{y} \\ &= \lim_{\beta \to \beta_n} \frac{2}{\beta^2 - \beta_n^2} \left[\frac{\mathrm{d}Y_n}{\mathrm{d}\hat{y}} (Y - Y_n) - Y_n \left(\frac{\mathrm{d}Y}{\mathrm{d}\hat{y}} - \frac{\mathrm{d}Y_n}{\mathrm{d}\hat{y}} \right) \right]_0^1 \\ &= \frac{1}{\beta_n} \left[\frac{\mathrm{d}Y_n}{\mathrm{d}\hat{y}} \frac{\mathrm{d}Y_n}{\mathrm{d}\beta_n} - Y_n \frac{\mathrm{d}}{\mathrm{d}\beta_n} \left(\frac{\mathrm{d}Y_n}{\mathrm{d}\hat{y}} \right) \right]_0^1 \\ &= -\frac{1}{\beta_n} \left[Y_n \frac{\mathrm{d}}{\mathrm{d}\beta_n} \left(\frac{Da\, Sh}{Da + \Delta} Y_n + \frac{\mathrm{d}Y_n}{\mathrm{d}\hat{y}} \right) \right]_{\hat{y}=1} \end{aligned} \tag{A.12}$$

The above expressions can be used to evaluate C_n and D_n without computing cumbersome numeric integrals, in the cases with $Da = 0$. In the general case, (A.9) must still be computed numerically, for which the methods described in this Section for the accurate and robust evaluation of $M(a, b; z)$ are essential. Derivatives with respect to β_n can also be approximated numerically with finite differences.

Appendix B

Neutronics and precursors data

This Appendix contains the numerical input parameters needed by the neutronics model calculations for the CNRS cavity benchmark (Section 3.1), the two-dimensional EVOL MSFR (Section 3.2) and the three-dimensional 1/16 cyclic MSFR (Section 4.1) cases. Neutronics data are condensed in 6 groups for neutron constants and 8 families for delayed neutron precursors constants. Data for decay heat precursor families are not reported since their presence has been neglected in the simulated cases.

For more details on the definitions and symbols used, the reader can refer to Section 2.3 and to the Nomenclature.

B.1 CNRS benchmark cavity

Neutronics data are summarised in Tables B.1 to B.4. The reference temperature selected for group constants adjustment is $T_0^\Sigma = 900$ K.

Table B.1: CNRS benchmark cavity neutron group constants: diffusion coefficient, absorption cross-section, fission cross-section.

g	$D^0_{n,g}$ (m)	$D^T_{n,g}$ (m)	$\Sigma^0_{a,g}$ (m^{-1})	$\Sigma^T_{a,g}$ (m^{-1})	$\Sigma^0_{f,g}$ (m^{-1})	$\Sigma^T_{f,g}$ (m^{-1})
1	+2.8006e−2	0	+5.4737e−2	0	+1.1131e−1	0
2	+1.8402e−2	0	+1.6473e−1	0	+1.0868e−1	0
3	+1.1311e−2	0	+3.3507e−1	0	+1.5222e−1	0
4	+1.4479e−2	0	+5.5967e−1	0	+2.5819e−1	0
5	+1.3975e−2	0	+1.2590e0	0	+5.3633e−1	0
6	+1.2825e−2	0	+3.4333e0	0	+1.4492e0	0

Table B.2: CNRS benchmark cavity neutron group constants: scattering cross-section.

(a) $\Sigma^{0}_{s,g\rightarrow h}$ (m^{-1})

$h \backslash g$	1	2	3	4	5	6
1	+1.0848e+1	+5.2332e0	+4.0181e−1	+1.0987e−2	+2.5329e−3	+3.7833e−4
2	0	+1.8367e+1	+3.1914e0	+2.3422e−3	+2.2526e−4	+2.0041e−5
3	0	0	+2.9829e+1	+1.6347e0	+1.7058e−3	+1.2463e−4
4	0	0	0	+2.1747e+1	+1.9024e0	+1.3686e−6
5	0	0	0	0	+2.2717e+1	+1.0589e0
6	0	0	0	0	0	+2.3783e+1

(b) $\Sigma^{T}_{s,g\rightarrow h}$ (m^{-1})

$h \backslash g$	1	2	3	4	5	6
1	0	0	0	0	0	0
2	0	0	0	0	0	0
3	0	0	0	0	0	0
4	0	0	0	0	0	0
5	0	0	0	0	0	0
6	0	0	0	0	0	0

Table B.3: CNRS benchmark cavity neutron group constants: average neutron yield per fission, average energy yield per fission, inverse neutron velocity, prompt fission yield spectrum, decay energy yield spectrum.

g	$\bar{\nu}_g$ (-)	$\bar{E}_{f,g}$ (J)	$1/v_g$ (m^{-1}s)	$\chi_{p,g}$ (-)	$\chi_{d,g}$ (-)
1	+2.8552e0	+3.2407e−11	+4.0037e−8	+3.5381e−1	+4.3033e−3
2	+2.5453e0	+3.2407e−11	+7.3985e−8	+5.2364e−1	+3.8773e−1
3	+2.4333e0	+3.2407e−11	+2.6175e−7	+1.2103e−1	+5.8185e−1
4	+2.4313e0	+3.2407e−11	+6.6927e−7	+1.3546e−3	+2.2795e−2
5	+2.4333e0	+3.2407e−11	+1.5585e−6	+1.5123e−4	+2.8913e−3
6	+2.4333e0	+3.2407e−11	+4.2446e−6	+7.3724e−6	+4.2894e−4

Table B.4: CNRS benchmark cavity precursor family constants: delayed neutron precursors fraction, delayed neutron precursors decay constant.

k	$\beta_{d,k}$ (-)	$\lambda_{d,k}$ (s^{-1})
1	+2.3310e−4	+1.2467e−2
2	+1.6602e−4	+2.8292e−2
3	+6.0581e−4	+4.2524e−2
4	+6.4092e−4	+1.3304e−1
5	+2.1449e−3	+2.9247e−1
6	+1.3773e−3	+6.6649e−1
7	+6.8188e−4	+1.6348e0
8	+1.0326e−3	+3.5546e0

B.2 Two-dimensional EVOL MSFR

Neutronics data are summarised in Tables B.5 to B.8. The reference temperature selected for group constants adjustment is $T_0^{\Sigma} = 900$ K.

Table B.5: Two-dimensional EVOL MSFR neutron group constants: diffusion coefficient, absorption cross-section, fission cross-section.

g	$D_{n,g}^0$ (m)	$D_{n,g}^T$ (m)	$\Sigma_{a,g}^0$ (m^{-1})	$\Sigma_{a,g}^T$ (m^{-1})	$\Sigma_{f,g}^0$ (m^{-1})	$\Sigma_{f,g}^T$ (m^{-1})
1	+2.3146e−2	−1.1819e−5	+6.2107e−1	−7.7864e−4	+4.4465e−1	−8.3425e−5
2	+1.5399e−2	+3.8237e−6	+3.2585e−1	−2.0856e−5	+2.5169e−1	−2.7809e−5
3	+9.7600e−3	−3.4761e−6	+3.9518e−1	+2.7809e−4	+1.8046e−1	+6.9521e−6
4	+1.1800e−2	−3.9280e−5	+7.7236e−1	+4.6649e−3	+2.6185e−1	+8.3425e−5
5	+1.1026e−2	−1.3904e−4	+1.5474e0	+4.3833e−2	+5.2003e−1	−7.4388e−4
6	+1.0263e−2	−2.3463e−4	+3.8791e0	+2.3648e−1	+1.3947e0	−1.0463e−2

B.3 Three-dimensional 1/16 cyclic MSFR

Neutronics data are summarised in Tables B.9 to B.12. The reference temperature selected for group constants adjustment is $T_0^{\Sigma} = 900$ K.

Table B.6: Two-dimensional EVOL MSFR neutron group constants: scattering cross-section.

(a) $\Sigma^{0}_{s,g\rightarrow h}$ (m^{-1})

$h \backslash g$	1	2	3	4	5	6
1	+1.3555e+1	+5.8054e0	+6.1574e−1	+4.1729e−3	+4.2940e−4	+3.6180e−5
2	0	+2.2042e+1	+3.7656e0	+6.4301e−3	+5.3583e−4	+2.3849e−5
3	0	0	+3.5039e+1	+1.4118e0	+2.3659e−3	+1.4904e−4
4	0	0	0	+2.7189e+1	+1.2754e0	+2.4034e−4
5	0	0	0	0	+2.9019e+1	+5.6930e−1
6	0	0	0	0	0	+2.9551e+1

(b) $\Sigma^{T}_{s,g\rightarrow h}$ (m^{-1})

$h \backslash g$	1	2	3	4	5	6
1	−1.0081e−2	+1.0463e−2	+2.7357e−3	−9.6113e−5	+3.7006e−5	−1.4165e−5
2	0	−2.0856e−3	+1.5295e−3	−1.3171e−4	+2.3411e−5	−3.1726e−6
3	0	0	+9.7330e−3	+2.7809e−4	−3.1632e−6	+1.3539e−5
4	0	0	0	+8.8640e−2	−1.8423e−3	−3.2300e−5
5	0	0	0	0	+3.5595e−1	−1.5854e−2
6	0	0	0	0	0	+5.2419e−1

Table B.7: Two-dimensional EVOL MSFR neutron group constants: average neutron yield per fission, average energy yield per fission, inverse neutron velocity, prompt fission yield spectrum, decay energy yield spectrum.

g	$\bar{\nu}_g$ (-)	$\bar{E}_{f,g}$ (J)	$1/v_g$ (m^{-1}s)	$\chi_{p,g}$ (-)	$\chi_{d,g}$ (-)
1	+3.0761e0	+3.3044e−11	+3.9811e−8	+3.6067e−1	+4.6450e−3
2	+2.8632e0	+3.3145e−11	+7.5204e−8	+5.1716e−1	+3.9391e−1
3	+2.7075e0	+3.2993e−11	+2.6880e−7	+1.2064e−1	+5.7539e−1
4	+2.6718e0	+3.2940e−11	+6.6204e−7	+1.3687e−3	+2.3069e−2
5	+2.6672e0	+3.2932e−11	+1.4947e−6	+1.5149e−4	+2.6741e−3
6	+2.6716e0	+3.2949e−11	+3.6576e−6	+7.4572e−6	+3.1626e−4

Table B.8: Two-dimensional EVOL MSFR precursor family constants: delayed neutron precursors fraction, delayed neutron precursors decay constant.

k	$\beta_{d,k}$ (-)	$\lambda_{d,k}$ (s^{-1})
1	+1.2243e−4	+1.2467e−2
2	+7.5701e−4	+2.8292e−2
3	+3.7605e−4	+4.2524e−2
4	+8.1366e−4	+1.3304e−1
5	+1.4791e−3	+2.9247e−1
6	+5.1985e−4	+6.6649e−1
7	+4.6285e−4	+1.6348e0
8	+1.5745e−4	+3.5546e0

Table B.9: Three-dimensional 1/16 cyclic MSFR neutron group constants: diffusion coefficient, absorption cross-section, fission cross-section.

g	$D^0_{n,g}$ (m)	$D^T_{n,g}$ (m)	$\Sigma^0_{a,g}$ (m^{-1})	$\Sigma^T_{a,g}$ (m^{-1})	$\Sigma^0_{f,g}$ (m^{-1})	$\Sigma^T_{f,g}$ (m^{-1})
1	+2.3146e−2	−1.1819e−5	+6.2107e−1	−7.7864e−4	+4.4465e−1	−8.3425e−5
2	+1.5399e−2	+3.8237e−6	+3.2585e−1	−2.0856e−5	+2.5169e−1	−2.7809e−5
3	+9.7600e−3	−3.4761e−6	+3.9518e−1	+2.7809e−4	+1.8046e−1	+6.9521e−6
4	+1.1800e−2	−3.9280e−5	+7.7236e−1	+4.6649e−3	+2.6185e−1	+8.3425e−5
5	+1.1026e−2	−1.3904e−4	+1.5474e0	+4.3833e−2	+5.2003e−1	−7.4388e−4
6	+1.0263e−2	−2.3463e−4	+3.8791e0	+2.3648e−1	+1.3947e0	−1.0463e−2

Table B.10: Three-dimensional 1/16 cyclic MSFR neutron group constants: scattering cross-section.

(a) $\Sigma^0_{s,g\to h}$ (m^{-1})

$h \backslash g$	1	2	3	4	5	6
1	+1.3555e+1	+5.8054e0	+6.1574e−1	+4.1729e−3	+4.2940e−4	+3.6180e−5
2	0	+2.2042e+1	+3.7656e0	+6.4301e−3	+5.3583e−4	+2.3849e−5
3	0	0	+3.5039e+1	+1.4118e0	+2.3659e−3	+1.4904e−4
4	0	0	0	+2.7189e+1	+1.2754e0	+2.4034e−4
5	0	0	0	0	+2.9019e+1	+5.6930e−1
6	0	0	0	0	0	+2.9551e+1

(b) $\Sigma^T_{s,g\to h}$ (m^{-1})

$h \backslash g$	1	2	3	4	5	6
1	−1.0081e−2	+1.0463e−2	+2.7357e−3	−9.6113e−5	+3.7006e−5	−1.4165e−5
2	0	−2.0856e−3	+1.5295e−3	−1.3171e−4	+2.3411e−5	−3.1726e−6
3	0	0	+9.7330e−3	+2.7809e−4	−3.1632e−6	+1.3539e−5
4	0	0	0	+8.8640e−2	−1.8423e−3	−3.2300e−5
5	0	0	0	0	+3.5595e−1	−1.5854e−2
6	0	0	0	0	0	+5.2419e−1

Table B.11: Three-dimensional 1/16 cyclic MSFR neutron group constants: average neutron yield per fission, average energy yield per fission, inverse neutron velocity, prompt fission yield spectrum, decay energy yield spectrum.

g	$\bar{\nu}_g$ (-)	$\bar{E}_{f,g}$ (J)	$1/v_g$ (m^{-1}s)	$\chi_{p,g}$ (-)	$\chi_{d,g}$ (-)
1	+3.0761e0	+3.3044e−11	+3.9811e−8	+3.6067e−1	+4.6450e−3
2	+2.8632e0	+3.3145e−11	+7.5204e−8	+5.1716e−1	+3.9391e−1
3	+2.7075e0	+3.2993e−11	+2.6880e−7	+1.2064e−1	+5.7539e−1
4	+2.6718e0	+3.2940e−11	+6.6204e−7	+1.3687e−3	+2.3069e−2
5	+2.6672e0	+3.2932e−11	+1.4947e−6	+1.5149e−4	+2.6741e−3
6	+2.6716e0	+3.2949e−11	+3.6576e−6	+7.4572e−6	+3.1626e−4

Table B.12: Three-dimensional 1/16 cyclic MSFR precursor family constants: delayed neutron precursors fraction, delayed neutron precursors decay constant.

k	$\beta_{d,k}$ (-)	$\lambda_{d,k}$ (s^{-1})
1	$+1.2243\mathrm{e}{-4}$	$+1.2467\mathrm{e}{-2}$
2	$+7.5701\mathrm{e}{-4}$	$+2.8292\mathrm{e}{-2}$
3	$+3.7605\mathrm{e}{-4}$	$+4.2524\mathrm{e}{-2}$
4	$+8.1366\mathrm{e}{-4}$	$+1.3304\mathrm{e}{-1}$
5	$+1.4791\mathrm{e}{-3}$	$+2.9247\mathrm{e}{-1}$
6	$+5.1985\mathrm{e}{-4}$	$+6.6649\mathrm{e}{-1}$
7	$+4.6285\mathrm{e}{-4}$	$+1.6348\mathrm{e}0$
8	$+1.5745\mathrm{e}{-4}$	$+3.5546\mathrm{e}0$

Bibliography

[1] Manuele Aufiero et al. “Calculating the Effective Delayed Neutron Fraction in the Molten Salt Fast Reactor: Analytical, Deterministic and Monte Carlo Approaches”. *Annals of Nuclear Energy* 65 (2014), pp. 78–90.

[2] Manuele Aufiero et al. “Development of an OpenFOAM Model for the Molten Salt Fast Reactor Transient Analysis”. *Chemical Engineering Science* 111 (2014), pp. 390–401. DOI: `10.1016/j.ces.2014.03.003`.

[3] C.F. Baes. “The Chemistry and Thermodynamics of Molten Salt Reactor Fuels”. *Journal of Nuclear Materials* 51.1 (1974), pp. 149–162. DOI: `10.1016/0022-3115(74)90124-X`.

[4] Florencio Balboa Usabiaga et al. “The Stokes-Einstein Relation at Moderate Schmidt Number”. *The Journal of Chemical Physics* 139.21 (2013), p. 214113. DOI: `10.1063/1.4834696`.

[5] A. Battistini et al. “Development of a CFD – LES Model for the Dynamic Analysis of the DYNASTY Natural Circulation Loop”. *Chemical Engineering Science* 237 (2021), p. 116520. DOI: `10.1016/j.ces.2021.116520`. (Visited on 02/27/2023).

[6] Ondřej Beneš and Rudy J.M. Konings. “Molten Salt Reactor Fuel and Coolant”. In: *Comprehensive Nuclear Materials*. Ed. by Rudy J.M. Konings. Oxford: Elsevier, 2012, pp. 359–389. ISBN: 978-0-08-056033-5. DOI: `10.1016/B978-0-08-056033-5.00062-8`.

[7] B. D. Bowen, S. Levine, and N. Epstein. “Fine Particle Deposition in Laminar Flow through Parallel-Plate and Cylindrical Channels”. *Journal of Colloid and Interface Science* 54.3 (1976), pp. 375–390. DOI: `10.1016/0021-9797(76)90317-9`.

[8] H. Brenner. “The Slow Motion of a Sphere through a Viscous Fluid towards a Plane Surface”. *Chemical Engineering Science* 16.3 (1961), pp. 242–251. DOI: `10.1016/0009-2509(61)80035-3`.

[9] M. Brovchenko et al. “Optimization of the Pre-Conceptual Design of the MSFR”. *Deliverable* 2 (2013), pp. 1–69.

[10] Jérôme Carrayrou, Robert Mosé, and Philippe Behra. “Operator-Splitting Procedures for Reactive Transport and Comparison of Mass Balance Errors”. *Journal of Contaminant Hydrology* 68.3 (2004), pp. 239–268.

[11] Federico Caruggi et al. "Multiphysics Modelling of Gaseous Fission Products in the Molten Salt Fast Reactor". *Nuclear Engineering and Design* 392 (2022), p. 111762. DOI: `10.1016/j.nucengdes.2022.111762`.

[12] E. Cervi et al. "Development of a Multiphysics Model for the Study of Fuel Compressibility Effects in the Molten Salt Fast Reactor". *Chemical Engineering Science* 193 (2019), pp. 379–393. DOI: `10.1016/j.ces.2018.09.025`.

[13] E. Cervi et al. "Development of an SP3 Neutron Transport Solver for the Analysis of the Molten Salt Fast Reactor". *Nuclear Engineering and Design* 346 (2019), pp. 209–219. DOI: `10.1016/j.nucengdes.2019.03.001`.

[14] Eric Cervi et al. "Multiphysics Analysis of the MSFR Helium Bubbling System: A Comparison between Neutron Diffusion, SP3 Neutron Transport and Monte Carlo Approaches". *Annals of Nuclear Energy* 132 (2019), pp. 227–235. DOI: `10.1016/j.anucene.2019.04.029`.

[15] E Compere et al. *Fission Product Behavior in the Molten Salt Reactor Experiment.* Tech. rep. ORNL–4865, 4077644. Oak Ridge National Laboratory, Oct. 1975, ORNL–4865, 4077644. DOI: `10.2172/4077644`. (Visited on 01/20/2021).

[16] James W. Deardorff. "A Numerical Study of Three-Dimensional Turbulent Channel Flow at Large Reynolds Numbers". *Journal of Fluid Mechanics* 41.2 (1970), pp. 453–480. DOI: `10.1017/S0022112070000691`. (Visited on 02/27/2023).

[17] Andrea Di Ronco et al. "Dynamic Mode Decomposition for the Stability Analysis of the Molten Salt Fast Reactor Core". *Nuclear Engineering and Design* 362 (2020), p. 110529. DOI: `10.1016/j.nucengdes.2020.110529`.

[18] *NIST Digital Library of Mathematical Functions.* Release 1.1.0 of 2020-12-15. 2020.

[19] Carlo Fiorina, Mathieu Hursin, and Andreas Pautz. "Extension of the GeN-Foam Neutronic Solver to SP3 Analysis and Application to the CROCUS Experimental Reactor". *Annals of Nuclear Energy* 101 (2017), pp. 419–428. DOI: `10.1016/j.anucene.2016.11.042`.

[20] Carlo Fiorina et al. "Development and Verification of the Neutron Diffusion Solver for the GeN-Foam Multi-Physics Platform". *Annals of Nuclear Energy* 96 (2016), pp. 212–222. DOI: `10.1016/j.anucene.2016.05.023`.

[21] Péter German et al. "Comparison of Reduced-Basis Techniques for the Model Order Reduction of Parametric Incompressible Fluid Flows". *Progress in Nuclear Energy* 130 (2020), p. 103551. DOI: `10.1016/j.pnucene.2020.103551`.

[22] W. R. Grimes. "Molten-Salt Reactor Chemistry". *Nuclear Applications and Technology* 8.2 (1970), pp. 137–155. DOI: `10.13182/NT70-A28621`.

[23] Abhijit Guha. "Transport and Deposition of Particles in Turbulent and Laminar Flow". *Annual Review of Fluid Mechanics* 40.1 (2008), pp. 311–341. DOI: `10.1146/annurev.fluid.40.111406.102220`.

[24] Alain Hébert. “Multigroup Neutron Transport and Diffusion Computations”. In: *Handbook of Nuclear Engineering.* Ed. by Dan Gabriel Cacuci. Boston, MA: Springer US, 2010, pp. 751–911. ISBN: 978-0-387-98149-9. DOI: `10.1007/978-0-387-98149-9\_8`. (Visited on 02/02/2021).

[25] R. I. Issa. “Solution of the Implicitly Discretised Fluid Flow Equations by Operator-Splitting”. *Journal of Computational Physics* 62.1 (1986), pp. 40–65. DOI: `10.1016/0021-9991(86)90099-9`.

[26] F. Johansson. “Arb: Efficient Arbitrary-Precision Midpoint-Radius Interval Arithmetic”. *IEEE Transactions on Computers* 66.8 (2017), pp. 1281–1292. DOI: `10.1109/TC.2017.2690633`.

[27] F. Johansson. “Computing Hypergeometric Functions Rigorously”. *ACM Trans. Math. Softw.* 45.3 (2019). DOI: `10.1145/3328732`.

[28] R. J. Kedl. *Migration of a Class of Fission Products (Noble Metals) in the Molten-Salt Reactor Experiment.* Tech. rep. ORNL-TM–3884, 4471292. Oak Ridge National Laboratory, Dec. 1972, ORNL–TM–3884, 4471292. DOI: `10.2172/4471292`. (Visited on 01/24/2021).

[29] Won-Wook Kim and Suresh Menon. “A New Dynamic One-Equation Subgrid-Scale Model for Large Eddy Simulations”. In: *33rd Aerospace Sciences Meeting and Exhibit.* Aerospace Sciences Meetings. American Institute of Aeronautics and Astronautics, 1995. (Visited on 02/28/2023).

[30] Arjan Koning et al. *The JEFF-3.1 Nuclear Data Library.* JEFF Report 21. OECD-NEA, 2006.

[31] B.E. Launder and D.B. Spalding. “The Numerical Computation of Turbulent Flows”. *Computer Methods in Applied Mechanics and Engineering* 3.2 (1974), pp. 269–289. DOI: `10.1016/0045-7825(74)90029-2`.

[32] Jaakko Leppänen et al. “The Serpent Monte Carlo Code: Status, Development and Applications in 2013”. *Annals of Nuclear Energy* 82 (2015), pp. 142–150. DOI: `10.1016/j.anucene.2014.08.024`.

[33] Benjamin Y.H Liu and Jugal K Agarwal. “Experimental Observation of Aerosol Deposition in Turbulent Flow”. *Journal of Aerosol Science* 5.2 (1974), pp. 145–155. DOI: `10.1016/0021-8502(74)90046-9`.

[34] H. G. MacPherson. “The Molten Salt Reactor Adventure”. *Nuclear Science and Engineering* 90.4 (1985), pp. 374–380. DOI: `10.13182/NSE90-374`.

[35] A. Marino et al. “A Multi-Physics Computational Tool Based on CFD and GEM Chemical Equilibrium Solver for Modeling Coolant Chemistry in Nuclear Reactors”. *Progress in Nuclear Energy* 120 (2020), p. 103190. DOI: `10.1016/j.pnucene.2019.103190`.

[36] F. R. Menter. “Two-Equation Eddy-Viscosity Turbulence Models for Engineering Applications”. *AIAA Journal* 32.8 (1994), pp. 1598–1605. DOI: `10.2514/3.12149`.

[37] Elia Merzari et al. "Large-Scale Large Eddy Simulation of Nuclear Reactor Flows: Issues and Perspectives". *Nuclear Engineering and Design*. 16th International Topical Meeting on Nuclear Reactor Thermal Hydraulics 312 (Feb. 2017), pp. 86–98. DOI: `10.1016/j.nucengdes.2016.09.028`.

[38] F. Nicoud and F. Ducros. "Subgrid-Scale Stress Modelling Based on the Square of the Velocity Gradient Tensor". *Flow, Turbulence and Combustion* 62.3 (1999), pp. 183–200. DOI: `10.1023/A:1009995426001`.

[39] OpenFOAM. *The OpenFOAM Foundation*. 2023. (Visited on 02/26/2021).

[40] S.V Patankar and D.B Spalding. "A Calculation Procedure for Heat, Mass and Momentum Transfer in Three-Dimensional Parabolic Flows". *International Journal of Heat and Mass Transfer* 15.10 (1972), 1787a–1806. DOI: `10.1016/0017-9310(72)90054-3`.

[41] J. W. Pearson, S. Olver, and M. A. Porter. "Numerical Methods for the Computation of the Confluent and Gauss Hypergeometric Functions". *Numerical Algorithms* 74.3 (2017), pp. 821–866. DOI: `10.1007/s11075-016-0173-0`.

[42] M.H.A. Piro et al. "The Thermochemistry Library Thermochimica". *Computational Materials Science* 67 (2013), pp. 266–272. DOI: `doi.org/10.1016/j.commatsci.2012.09.011`.

[43] Terry Price, Ondrej Chvala, and George Bereznai. "A Dynamic Model of Xenon Behavior in the Molten Salt Reactor Experiment". *Annals of Nuclear Energy* 144 (2020), p. 107535. DOI: `10.1016/j.anucene.2020.107535`.

[44] D. C. Prieve and E. Ruckenstein. "Rates of Deposition of Brownian Particles Calculated by Lumping Interaction Forces into a Boundary Condition". *Journal of Colloid and Interface Science* 57.3 (1976), pp. 547–550. DOI: `10.1016/0021-9797(76)90232-0`.

[45] E. Ruckenstein and D. C. Prieve. "Rate of Deposition of Brownian Particles under the Action of London and Double-Layer Forces". *J. Chem. Soc., Faraday Trans. 2* 69.0 (1973), pp. 1522–1536. DOI: `10.1039/F29736901522`.

[46] Jérôme Serp et al. "The Molten Salt Reactor (MSR) in Generation IV: Overview and Perspectives". *Progress in Nuclear Energy* 77 (2014), pp. 308–319. DOI: `10.1016/j.pnucene.2014.02.014`.

[47] J. Smagorinsky. "General Circulation Experiments with the Primitive Equations: I. The Basic Experiment". *Monthly Weather Review* 91.3 (1963), pp. 99–164. DOI: `10.1175/1520-0493(1963)091{$<$}0099:GCEWTP{$>$}2.3.CO;2`. (Visited on 02/27/2023).

[48] Marco Tiberga et al. "Preliminary Investigation on the Melting Behavior of a Freeze-Valve for the Molten Salt Fast Reactor". *Annals of Nuclear Energy* 132 (2019), pp. 544–554. DOI: `10.1016/j.anucene.2019.06.039`.

[49] Marco Tiberga et al. "Results from a Multi-Physics Numerical Benchmark for Codes Dedicated to Molten Salt Fast Reactors". *Annals of Nuclear Energy* 142 (2020), p. 107428. DOI: `10.1016/j.anucene.2020.107428`.

[50] Yoshihide Tominaga and Ted Stathopoulos. "Turbulent Schmidt Numbers for CFD Analysis with Various Types of Flowfield". *Atmospheric Environment* 41.37 (2007), pp. 8091–8099. DOI: `10.1016/j.atmosenv.2007.06.054`.

[51] Samuel A. Walker and Wei Ji. "Species Transport Analysis of Noble Metal Fission Product Transport, Deposition, and Extraction in the Molten Salt Reactor Experiment". *Annals of Nuclear Energy* 158 (2021), p. 108250. DOI: `10.1016/j.anucene.2021.108250`.

[52] R. F. Warming and Richard M. Beam. "Upwind Second-Order Difference Schemes and Applications in Aerodynamic Flows". *AIAA Journal* 14.9 (Sept. 1976), pp. 1241–1249. DOI: `10.2514/3.61457`. (Visited on 07/17/2023).

[53] H. G. Weller et al. "A Tensorial Approach to Computational Continuum Mechanics Using Object-Oriented Techniques". *Computer in Physics* 12.6 (1998), pp. 620–631. DOI: `10.1063/1.168744`.

[54] David C. Wilcox. "Formulation of the K-w Turbulence Model Revisited". *AIAA Journal* 46.11 (2008), pp. 2823–2838. DOI: `10.2514/1.36541`.

[55] Brian D. Wood, Michel Quintard, and Stephen Whitaker. "Estimation of Adsorption Rate Coefficients Based on the Smoluchowski Equation". *Chemical Engineering Science* 59.10 (2004), pp. 1905–1921. DOI: `10.1016/j.ces.2003.12.021`.

[56] Akira Yoshizawa. "Statistical Theory for Compressible Turbulent Shear Flows, with the Application to Subgrid Modeling". *The Physics of Fluids* 29.7 (1986), pp. 2152–2164. DOI: `10.1063/1.865552`.

Ringraziamenti

Quando conclusi la mia tesi di laurea, non aggiunsi nessun tipo di ringraziamento. Le ragioni di ciò si sono perse rapidamente, tanto che successivamente mi dissi che potendo tornare indietro non avrei commesso lo stesso errore. Si potrebbe quasi dire che parte della motivazione che mi ha spinto a intraprendere questa avventura di dottorato, nei suoi alti e bassi, sia qui: poter scrivere una nuova tesi a cui aggiungere queste poche righe. Ora che l'occasione per fare ammenda è finalmente arrivata, mi rendo conto che l'unica reale ragione della mia originaria mancanza fu la pigrizia.

Il primo sentito ringraziamento va ai miei supervisori, i Proff. Antonio Cammi, Francesca Giacobbo e Stefano Lorenzi. Sotto la vostra guida ho avuto la possibilità di affrontare diversi temi e problemi e di rappresentare il nostro Ateneo. Il mio auspicio è di poter continuare a mettere a frutto quanto ho imparato, da voi e con voi, e dare un contributo a questa disciplina che ci accomuna e che continua ad affascinarmi. Ma soprattutto, grazie di cuore per avermi gratificato nei miei momenti migliori e tollerato in quelli peggiori, sempre con correttezza, comprensione e amicizia.

Il secondo pensiero va a tutti coloro i quali hanno abitato con me l'ufficio dottorandi al Politecnico. Il mio ricordo va alle risate, alle stravaganze, alle briscole dopo pranzo, alle merende pomeridiane alle macchinette, agli aperitivi in ufficio del venerdì sera. A tutti i momenti di reciproco sostegno, e di confronto sia sul piano umano che accademico. Mi avete fatto sentire a casa in quella che a tutti gli effetti è stata la mia seconda casa per tanti anni. Grazie dunque a Stefano - ora in veste di collega -, Davide e Tommaso: siete stati i miei punti di riferimento ed una fonte di ispirazione e conoscenze. Grazie anche a Carolina, Alessio, Marco Tudor, Marco, Christian, Federico, Giovanni, Gabriele, Jonas: siete stati dei compagni di viaggio ben migliori di quanto avrei potuto desiderare.

Per concludere il versante milanese, un grazie va anche a tutto il resto del Gruppo Reattori Nucleari e a tutti i "ragazzi di nucleare" per aver contribuito a creare questa famiglia allargata di cui mi sentirò sempre un membro orgoglioso. Che il gruppo NuclearFantaCalcio possa non morire mai.

Ci tengo ora a ringraziare l'Ing. Gioacchino Miccichè. Ci siamo conosciuti solo alla fine di questa avventura: grazie per avermi accolto nella mia nuova casa e di avermi guidato con amicizia, competenza e autorevolezza verso una nuova fase della mia vita professionale. Un pensiero va anche a tutto il resto della famiglia di Brasimone: in particolare - di nuovo - a Gabriele, compagno di tanti pomeriggi passati tra avvitatori, videocamere e saldature, e a tutto il team di ENEA e *new*cleo, per avermi accolto a bordo.

È ora il turno della compagnia di Varese. Tante volte mi è stato detto che le amicizie giovanili vanno e vengono e non sono destinate a durare. Questo pensiero, fonte di dubbi e tristezza che mi ha accompagnato per anni, si è nel tempo trasformato nella certezza che siete i miei amici e lo sarete sempre, anche nella distanza. Grazie dunque a Mattia, Alessandro, Francesco, Giacomo, Matteo, Stefano, Elia, Marco e Marco, per avermi concesso il privilegio di crescere insieme a voi. A noi va l'augurio di continuare ad esserci sempre per una birra in Buttiga e di trovarci tra altri 30 anni ancora ad annoiare il resto dei presenti con i soliti aneddoti dei tempi del liceo.

Grazie alla mia famiglia. Ai miei genitori Adele e Giorgio, per non avermi mai condizionato nelle mie scelte, per essere stati sempre al mio fianco e per avermi dato tutto l'aiuto ed il supporto di cui ho avuto bisogno. Anche se a volte non ci si capisce del tutto, spero di riuscire a non farvi mai mancare il mio affetto come voi non mi avete fatto mai mancare il vostro. A mio fratello Matteo, amico, compagno, rivale e modello: che i nostri percorsi non ci allontanino mai. A tutti i nonni, soprattutto a quelli che non ci sono più: se sono qui il merito è anche un po' vostro.

L'ultimo ringraziamento va a Nicole. Se questa tesi esiste concretamente, gran parte del merito va a te. Hai creduto in me più di chiunque altro aiutandomi, sempre con dolcezza e generosità, a ritrovare le forze ogni volta che mi sono mancate. Che questo sia il primo di tanti traguardi insieme.

Bologna, settembre 2023